LAPPEENRANTA UNIVERSITY OF TECHNOLOGY
LUT School of Energy Systems
LUT Mechanical Engineering
Laboratory of Welding Technology

Tarig Abdo

THE EFFECTS OF HEAT INPUT AND MECHANICAL CONSTRAINTS ON THE MAG AND LASER WELDABILITY OF 316L STAINLESS STEEL

Examiners: Associate Professor Paul Kah
M.Sc. Esa Hiltunen

ABSTRACT

Lappeenranta University of Technology
LUT School of Energy Systems
Degree Program in Mechanical Engineering

Tarig Abdo

The effects of heat input and mechanical constraints on the MAG and laser weldability of 316L stainless steel.

Master's thesis

2018

90 Pages, 46 Figures, 11 Tables and 4 appendices.

Examiners: Associate Professor Paul Kah
M.Sc. Esa Hiltunen

Key words: Angular distortion, Bowing, Ferrite structure, Hot cracking, Intergranular corrosion, 316L stainless steel, Weldability.

Stainless steel is the dominant material in many industries such as petrochemicals, paper and pulp, cutlery and food processing units, in addition to offshore and corrosive environment applications. While welding represents the essential joining method for metals under demanding conditions, weldability of austenitic stainless steel must be guaranteed. High coefficient of thermal expansion remains a welding challenge for austenitic stainless steel. Whereas, it promotes the occurrence of the distortion in the welded structures. In this study, angular and longitudinal distortion on thin plates of austenitic stainless steel have been investigated. Ten samples of 316L stainless steel with 3 mm thickness were welded in butt-square joints using MAG and fiber laser welding processes. Therefore, angular and longitudinal distortions were measured by laser- 2D highly sensitive device, and then optical micrograph used to reveal the microstructure and carbides precipitation.

Fibre laser welding has produced smaller fusion zone and smaller heat affected zone (HAZ) compared to MAG welding. Therefore, relatively smaller distortion has been generated for the laser-welded samples. Laser welding speed of 2.2 m/min, the power of 2.5KW, and the focal position of 3mm represent the optimum parameters to prevent distortion in the 3mm plate of 316L stainless steel. In MAG welding, test results revealed a proportional relation between welding heat input (KJ/mm) and angular distortion. Raising the heat input from 0.3 to 0.472 KJ/mm increases the angle of distortion four times and increases the bending on the welded plate three times from 1.2 mm to 3.6mm. Constraints, which applied in form of a mechanical clamp does not prevent the occurrence of distortion.

316L showed Ferrite-Austenite solidification mode and an insignificant tendency to hot cracking due to moderate content of ferrite structure estimated as 10% of the total structure. SEM micrography beside the EDS test revealed a proportionality between heat input and

carbides formations on the grain boundaries of HAZ, which indicates that degree of sensitization (DOS) to intergranular corrosion is higher when heat input increases and welding speed decreases. FE model has built with ANSYS to simulate the experiment and verify the model based on experimental results, the simulation model showed a significant deviation in the distortion results. Disability of the FE software to introduce the completely welding parameters justifies the variation between numerical and experimental results.

ACKNOWLEDGEMENT

It is a great pleasure to express my deepest acknowledge to Prof. Paul Kah, Associate professor, the welding laboratory- Lappeenranta University of Technology for his kind supervision and his unfailing support since the early beginning of this research till the time I am writing these words.

I would like to express my sincere appreciation to M.Sc.Esa Hiltunen, Laboratory engineer, the welding laboratory- Lappeenranta University of Technology and for the technicians at the welding laboratory who were involved in the practical part of the research. Furthermore, I would like to thank Dr. Eric Belinga and my colleagues, the researchers at the welding laboratory for their appreciated technical support.

Finally, I would like to express my very profound gratitude to my parents and my spouse for their moral support, and I would like to dedicate this work for them and for all my family.

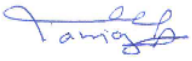

Tarig Abdo

Lappeenranta 10.10.2018

TABLE OF CONTENTS

1 INTRODUCTION 11

1.1 Definition of weldability 11

1.2 Stainless steel 13

1.3 Classification of stainless steel 13

1.3.1 Ferritic stainless steel 15

1.3.2 Austenitic-ferritic stainless steel 15

1.3.3 Martensitic stainless steel 15

1.3.4 Austenitic stainless steel 15

1.4 Applications of stainless steel 16

1.5 Previous researches in weldability of austenitic stainless steel 19

1.6 Welding challenges of austenitic stainless steel 20

1.7 Research objective 22

1.8 Research problem 22

1.9 Research questions 23

1.10 Implementation methods of the research 23

2 WELDING PROCESSES 24

2.1 Gas metal arc welding process (GMAW) 24

2.1.1 Metal transfer modes in GMAW 25

2.1.2 GMAW process for joining austenitic stainless steel 28

2.2 Laser beam welding process (LBW) 33

2.2.1 Effect of different laser processes and parameters on weld quality of austenitic SS 35

3 RESIDUAL STRESSES AND DISTORTION 38

3.1 Residual stress in welding 38

3.2 Effect of welding conditions on residual stresses 40

3.3 Influence of residual stresses on corrosion resistance 40

3.4 Distortion in welded structures **41**

3.5 Types of distortion in welding **42**

3.5.1 Angular distortion 42

3.5.2 Shrinkage 44

3.6 Distortion prediction and mitigation **46**

4 EXPERIMENT METHODOLOGY **50**

4.1 Welding procedure specifications (WPS) **51**

4.2 Material properties. **53**

4.3 Weld tests **54**

4.3.1 Angular distortion 54

4.3.2 Longitudinal distortion (Bowing) 55

4.3.3 Samples preparation and Macro examination 56

4.3.4 Optical microscope image 57

4.3.5 Scanning Electron Microscope (SEM) and Electron Dispersive Spectrometer (EDS) ... 58

5 RESULTS AND ANALYSIS **60**

5.1 Visual inspection and quality assessment. **60**

5.2 Angular distortion measurements **62**

5.3 Longitudinal distortion/bowing measurements **66**

5.4 Microstructure analysis and hot cracking **69**

5.5 SEM, EDS and carbides investigation results **75**

5.6 Intergranular corrosion (IGC) and Critical cooling rate (CCR) **78**

6 SIMULATION MODEL **80**

7 CONCLUSION **83**

8 FURTHER STUDIES **85**

REFERENCES **86**

APPENDICES

LIST OF ABBREVIATIONS

AF	Austenite-ferrite solidification mode
AWS	American Welding Society
BM	Base material
CCR	Critical cooling rate
CR	Cooling rate
CW	Continuous wave
EDS	Electron dispersive spectrometer
EN	European Standard
FA	Ferrite-austenite solidification mode
FCAW	Flux cored-electrode arc welding
FEM	Finite-elements model
FZ	Fusion zone
GMAW	Gas metal arc welding
HAZ	Heat affected zone
IGC	Intergranular corrosion
ISO	International Organization for Standardization
KJ	Kilojoule
KW	Kilowatt
LBW	Laser beam welding
LOP	Lack of penetration
LVDT	Linear variable differential transformer
m/min	Meter per minute
MAG	Metal active gas
MIG	Metal inert gas
SEM	Scanning electron microscope
SMAW	Shielded metal arc welding
WPS	Welding procedure specification

LIST OF TABLES

Table 1. Definition and chemical composition of different stainless steel groups (mod. EN10088-1 2014, pp 12-43). 14
Table 2. Minimum required current (Transition current) for spray transfer mode (Mod. Harris, et al., 2004, p. 155). 27
Table 3. Effect of oxygen percentage in the shielding gas and mode of metal transfer on the radius of curvature. 316L stainless steel butt-weld joints. (Puchi-Cabrera, et al., 2009) .. 30
Table 4. The chemical composition of 316L austenitic stainless steel welded joint obtained with a different N_2 percentage in the shielding gas for variable welding currents (Trevisan, et al., 2003) 33
Table 5. Influence of focal position (F) on the laser weld seam dimensions (Gietzelt, et al., 2015). 37
Table 6. Welding parameters of the MAG samples. 52
Table 7. Laser welding parameters. 53
Table 8. Materials composition. 53
Table 9. Mechanical properties. 53
Table 10. Distortion angle 65
Table 11. Longitudinal distortion 69

LIST OF FIGURES

Figure 1. Consumption of stainless steel by sectors in India, China and the western world (Baddoo, 2008). 19
Figure 2. Basic equipment for gas metal arc welding process (Harris, et al., 2004). 25
Figure 3. Metal transfer modes in gas metal arc welding process (Slane, 2010) 27
Figure 4. Effect of metal transfer mode and O_2 percentage in the shielding gas on fatigue life of 316L stainless steel (Puchi-Cabrera, et al., 2009). 29
Figure 5. Correlation between N_2 addition to CO_2 shielding gas, the formation of δ-ferrite (F %), solidification crack (LTG), mean pulse current (A) and deposited N into the weld pool (Trevisan, et al., 2003). 32
Figure 6. Effect of the current intensity on the total crack length (Trevisan, et al., 2003)..... 32
Figure 7. keyhole welding process (Sokolov & Salminen, 2014). 35
Figure 8. The difference in 304SS laser welds cross sections obtained by different weld technological parameters (Gietzelt, et al., 2015). 36
Figure 9. Distribution of a residual stresses on a butt joint ("Mod." Nasir, et al., 2016). 39
Figure 10. Angular distortion measurement devices. LVDT (a) and Goniometer (b). (Adamczuk, et al., 2017) 43
Figure 11. The relation between welding passes and angular distortion (Adamczuk, et al., 2017). 44
Figure 12. Different types of distortion in the butt and fillet weld (Damen, 2015) 45
Figure 13. Measuring method of deflection in the welded sheet (Deng & Murakawa, 2008). 47
Figure 14. Tack welding in square butt-weld joint (Brown, 2018) 48
Figure 15. Welding distortion preventive techniques. 49
Figure 16. Welding robot used in the experiment to create the MAG welding samples..... 50
Figure 17. Welding fit- up. Partially constrained (A) and fully constrained (B). 51
Figure 18. The laser-2D device, utilized for measuring distortion..... 55
Figure 19. Longitudinal distortion measurement. 56
Figure 20. Samples preparation for micrography. 57
Figure 21. Optical microscope used to reveal the microstructure of the welded samples. 58
Figure 22. Samples preparation for SEM and EDS test. 59
Figure 23. Optical micrograph for MAG and laser weld samples. Images reveal LOP for laser-1 and laser- 2 and excess penetration in MAG 1, MAG-2 and MAG-5. 61
Figure 24. Angular distortion on the MAG welded samples. 62
Figure 25. Angular distortion in MAG welded samples. 63
Figure 26. Angular distortion for laser welding samples. 64

Figure 27. The relation between angular distortion, welding speed, and heat input. 66
Figure 28. Longitudinal distortion for weld samples (MAG & Laser) on the left side of the plate (L-1). 67
Figure 29. Longitudinal distortion for weld samples (MAG & Laser) on the right side of the plate (L-2). 68
Figure 30. The relation between longitudinal distortion, welding speed, and heat input. 69
Figure 31. Schaeffler-diagram for 316L and filler material (Elga cromamig 316L Si). 70
Figure 32. Solidification modes of austenitic stainless steel (Shankar, et al., 2003). 71
Figure 33. Fe-Cr-Ni ternary diagram (a). Derived binary diagram at 70% iron content (b). (mod. Shankar, et al., 2003) 71
Figure 34. WRC-92 diagram for 316L austenitic stainless steel (mod. Shankar, et al., 2003). 72
Figure 35. Hot-cracking susceptibility in austenitic stainless steel (mod. Shankar, et al., 2003). .. 73
Figure 36. Optical microscope images for weld samples at the fusion line. 74
Figure 37. Optical microscope images for weld samples at the weld center. 75
Figure 38. SEM-microstructure images for weld samples MAG-2, MAG-3 & Laser-3. 76
Figure 39. Carbides formation indication. 76
Figure 40. EDS mapping scan for sample MAG-2 at HAZ-Carbides formation. 77
Figure 41. EDS mapping scan for sample MAG-3 at HAZ-Carbides formation. 78
Figure 42. Cooling rate measured from the data obtained from laser temperature – sensor 79
Figure 43. Simulation model-Thermal diffusion by the end of welding path. 80
Figure 44. Deformation of the welded plate in the simulation model. Angular distortion (a) and the lonfitudinal distortion (b). 81
Figure 45. Difference between the simulation model and experiment in angular distortion. 81
Figure 46. Difference between the simulation model and experiment in bowing measurement. ... 82

1 INTRODUCTION

It is self-evident for steel to be the most prevalent material in welding, where it represents the dominant material in construction and engineering applications in general. The leading categories of steel are carbon steel, high strength steel, and stainless steel. Different categories vary in their ability to be welded under certain conditions which known linguistically as “Weldability”.

1.1 Definition of weldability

The word "Weldability" has been defined different ways with various expression. Most of these definitions are about the same concept. The term weldability refer to the easiness of welding of a certain material by utilizing the common, available processes and tools to produce a sound weld joint has the similar properties of the parent material. There are several common definitions stated either by welding institutes or by welding scientists. Grigorenko and Kostin (2013, p. 815) have tried to collect some of the standard definitions:

- ISO, which is a well-known body that develops and publish standards, described weldability in ISO 581:1980 standard as, “The metal can be regarded as weldable if welding results in the formation of a sound welded joint using the welding process producing the joints satisfying the requirements on the local properties”.
- British standard of welding described weldability as well in 499-1: 2009 document as, “weldability is the capacity of the material to be welded by any method without any special measures in order to produce the welded joint with the properties satisfying the requirements.”
- As per the Russian standard GOST 29273-92, “The metallic material is regarded as weldable up to the required extent in the given processes and for the given application with the welding process resulting in metallic integrity in the appropriate technological process so that the welded components satisfy the technical requirements with respect to both the interface quality and the effect on the construction which they form”.

The American Welding Society (AWS) has defined weldability as, “The capacity of material to be welded under fabrication condition imposed into a specific, suitably designed structure and to perform satisfactorily in the intended service” (Lippold, 2015, p. 1).

Welding researchers and scientists have their own point of view to define the weldability term and determine different methods for assessing the weldability of materials. For instance, Budkin and Redchits (2013) have adopted a criteria approach to evaluating the weldability of materials. Budkin’s idea was about building a physical-chemical model for metallurgical and thermal processes in order to categorize the materials based on their weldability. Detailed equations have been formulated to consider all the parameters, which can affect the weldability.

Dieter Radaj (1992), a pioneer welding researcher, has clarified in his book (Heat effects of welding) the basic phenomena which constitute the term “weldability.” Radaj stated “The generation of weld imperfection and defects, the initiation of cold and hot cracks mainly in the partly molten metal (intensified by hydrogen diffusion), the microstructural changes in the heat-affected zone of the base metal connected with hardening or softening, and the generation of residual stresses and distortion in the whole structure connected with mainly negative effect of strength.” Radaj proceeded to define weldability by “a property of the structure to be welded influenced by design, material and manufacturing measures.”

Baker et al., from the United Kingdom, have defined weldability in their publication ‘Assessment of Material Weldability' as "Capacity of material to be welded by any desired process to produce welded joint whose properties allow the full potential of the parent material to be exploited." A well-known fact for the steel weldability that it decreases proportionally with the carbon content. Low carbon steel has better weldability when compared to medium and high carbon steel. Other impurities can have the same negative effects on weldability such as sulphur and phosphor.

Other scientists argued that the relation between weldability and carbon content is not permanently inversely. Steel with 0.65 % Carbon can have better weldability than 0.4 % C steel, while hot cracking occurs severely near 0.4 % C content. (Tamaki, et al., 2003, p. 26)

1.2 Stainless steel

Plain steel characterized with a poor corrosion resistance, stainless steel considered as an effective alternative to meet the corrosive environment for different engineering applications. Stainless steel is a series of iron-based alloy with additives that can resist different corrosion environments such as humid air, salt water, and acids. Chromium (Cr) is the main alloying element responsible for corrosion resistance. Steel with more than 10.5% Cr considered as stainless steel. (Outokumpu, 2013)

Addition of Nickel (Ni) enhances the formation of an austenitic structure that results in high mechanical properties. Ni-Cr steel is superior material in strength, ductility (even at low temperature), toughness and sever corrosion applications such as sulphuric acids. Molybdenum (Mo) addition resists pitting corrosion and general corrosion as well, on the other hand, it promotes the formation of ferritic structure. Manganese (Mn) is added to stainless steel to resist de-oxidation at elevated temperature, it is austenite stabilizer at low temperature and ferrite stabilizer at high temperature, Mn resists hot cracking by preventing the formation of iron sulphide inclusions. Nitrogen (N) is austenite stabilizer element that, therefore it improves the mechanical properties. Ni helps to minimize the localized corrosion, especially when added with Molybdenum. (Outokumpu, 2013)

Berthier, a French mineralogist was a pioneer in discovering the Chromium ability of corrosion resistance in 1821. In 1892, Robert Hadfield, another mineralogist from England, has disapproved Berthier's fact. Hadfield adduced the deficiency of Chromium to resist corrosion. Hadfield stated his allegation based on sulphuric acid environment test. He would have a different conclusion with seawater or nitric acid corrosion environment. In 1911, Monnartz criticized Hadfield’s allegation after publishing a comprehensive report on Cr-Fe clarifying their ability to resist corrosion, especially for acidic mediums. Later on, parallel experiments were accomplished in Germany, England, and the USA between 1912 -1916 and all the studies proved the significant advantages of Cr addition to steel for resisting oxidation and rust formation. (Outokumpu, 2013)

1.3 Classification of stainless steel

Steel with at least 10.5% Cr and maximum 1.2% C content can be categorized as stainless steel as stated by the European standard document, EN 10088-1:2014, 3.1. Different types

of stainless steel are available based on the amount of Cr and other alloying elements, heat treatment, and fabrication method. The European standard has classified stainless steel with names and designation numbers based on the chemical composition. The same standard adopted three main categories of stainless steel; corrosion resistance steel, heat resistance steel and creep resistance steel. Table 1 illustrates the manner how the classification done by the European standard. In table 1 random material grades have been selected from the main tables in EN 10088-1 to represent different groups of stainless steel with different applications. While the objective of table 1 is to show how the European standard has derived the designation of the stainless steel from the chemical composition, it does not cover all the mentioned groups in the original source.

Table 1. Definition and chemical composition of different stainless steel groups (mod. EN10088-1 2014, pp 12-43).

Name	Number	C	Si	Mn	P	S	Cr	Mo	Ni	N	Ti
Chemical composition of austenitic corrosion resisting steels											
X2CrNiN18-7	1.4318	0.03	1.0	2.0	0.045	0.015	16.5-18	-	6-8	0.1-0.2	-
X9CrNi18-9	1.4325	0.03-0.05	1.0	2.0	0.045	0.03	17-19	-	8-10	-	-
X1CrNiSi18-15-4	1.4361	0.015	3.7-4.5	2.0	0.025	0.01	16.5-18.5	0.2	14-16	0.1	-
Chemical composition of austenitic heat resisting steel											
X8CrNiTi18-10	1.4878	0.1	1.0	2.0	0.045	0.015	17-19	-	9-12	-	0.5-0.8
Chemical composition of austenitic creep resistance steel											
X6CrNi18-10	1.4948	0.04-0.08	1.0	2.0	0.035	0.015	17-19	-	8-11	0.1	-
Chemical composition of austenitic-ferritic corrosion resisting steels											
X2CrNiN22-2	1.4062	0.03	1.0	2.0	0.04	0.01	21.5-24	0.45	1-2.9	0.16-0.28	-
X3CrNiMoN27-5-2	1.4460	0.05	1.0	2.0	0.035	0.015	25-28	1.3-2.0	4.5-6.5	0.05-0.2	-
Chemical composition of ferritic corrosion resisting steels											
X2CrNi12	1.4003	0.03	1.0	1.5	0.04	0.015	10.5-12	-	0.3-1.0	0.03	
X2CrMnNiTi12	1.4600	0.03	1.0	1-2.5	0.04	0.015	11-13	-	0.3-1.0	0.025	0.18-0.35
Chemical composition of ferritic heat resisting steel											
X10CrAlSi7	1.4713	0.12	0.5-1.0	1.0	0.04	0.015	6-8	Al (0.5-1.0)			

1.3.1 Ferritic stainless steel

Steel with chromium content within the range of (11.2 – 19%). Reasonable price compares to austenitic stainless steel due to the absence of nickel. Molybdenum is present to improve the corrosion resistance. Niobium and titanium are common in ferritic stainless steel to improve the weldability, which is poor relatively. Ferritic heat-resistant grades are favourable to replace austenitic stainless steel when sulphur reaction anticipated. It is typically achieved by increasing the carbon content above the average limit, which results in good creep resistance. Silicon and aluminium are added to resist oxidation at elevated temperatures. (Outokumpu, 2013)

Ferritic stainless steel is magnetic up to specific temperature, almost 750°C. The higher the chromium content within the limit, the better corrosion resistance. Limited formability and weldability of ferritic stainless steel restrained its application, despite the improved design of automotive assembly lines to fit the requirements of forming and welding the ferritic stainless steel. Ferritic stainless steel highly resists the stress corrosion cracking, in contrast to austenitic stainless steel. (Beddoes & Parr, 1999)

1.3.2 Austenitic-ferritic stainless steel

A balanced phase of ferrite and austenite structure. It combines respective merits of both categories. Known as duplex stainless steel. It contains high chromium percentage, up to 25%, molybdenum (0.3-4%) and less nickel compared to austenitic stainless steel. Nitrogen is added to improve strength and manganese to substitute nickel and to enhance the solubility of nitrogen. Supreme strength among the other types of stainless steel. (Outokumpu, 2013)

1.3.3 Martensitic stainless steel

Least spread group of stainless steel. Highest strength and hardness due to higher carbon content and the presence of nitrogen in some grades. No or rather tiny percentages of nickel and molybdenum. Higher carbon content is the main reason for poor weldability in martensitic stainless steel. (Outokumpu, 2013)

1.3.4 Austenitic stainless steel

It represents the greatest group of stainless steels in the application. Chromium content is between (12-27%), nickel (7-30%), molybdenum (2-3%), carbon concentration is quite low

(0.02-0.08%). A non-magnetic material, produced in solution-annealed state; heat treatments are not applicable for hardening the material. (Weman, 2012, p. 198) Austenitic stainless steel has distinctive mechanical properties, good creep resistance at elevated temperatures and excellent ductility at cryogenic temperatures.

The corrosion resistance of austenitic stainless steel is the best among the other groups. It has a good weldability and formability. Fabrication by cold working is preferable to improve the strength. Some grades contain a higher amount of alloying elements, up to 25% chromium, 25% of nickel and 7% of molybdenum. These materials suit the high demanding applications and known as super austenitic stainless steel or high performance austenitic. Another grade of austenitic stainless steel known as "high temperature austenitic". It suits the elevated temperature applications and dry gases environment. It provides long service and good creep resistance. (Outokumpu, 2013)

The structure of austenitic stainless steel is gamma iron with a minor amount of carbon, which justifies the nonmagnetic nature. Presence of sufficient amount of nickel in austenitic stainless steel is essential for retaining the austenitic structure at room temperature. Furthermore, nickel resists some of the corrosion environments. Another category of austenitic stainless steel known as, manganese – nitrogen austenitic stainless steel. Manganese and nitrogen partially replaced nickel for this grade to achieve economic benefits and when nickel is not available. (Beddoes & Parr, 1999)

1.4 Applications of stainless steel

Indisputably, steel is the most utilized material in construction, and stainless steel is one of the basic grades of steel. The production of stainless steel has increased from five million tons in 1970 to 34 million tons in 2010 (Outokumpu, 2013) and 48 million tons in 2017 (ISSF, 2018). Oil and gas industry, automotive manufacturing, household utensils, chemical plants in addition to the offshore and highly corrosive environment are the dominant consumers of stainless steel. More than half of the stainless steel produced parts are a cold rolled sheet, about one fifth are bars, and 10% are hot rolled plates. Stainless steel tubes are common in production and casting is minor. Almost 25% of stainless steel production serving the food industry sector, 20% for chemical, oil and gas industry, 8% for washing machines and the same amount for transportation. Frying pans and cutlery represent 9% of

the total production of stainless steel and 5% for each of construction sector, pulp and paper industry. Energy and kitchen equipment beside other application forms the remaining percentage. (Outokumpu, 2013)

One of the fundamental characteristics of stainless steel is the excellent fire resistance, even in case of fire, it does not emit any toxic fumes. Therefore, it is favourable material for many applications inside buildings such as stairways, floor coating besides wall and tunnels cladding. Following is the summary of the primary applications of stainless steels associated with the appropriate group of steel for each application as mentioned by Beddoes and Parr. (1999, p.239-259)

- Cutlery; Martensitic stainless steel is a good option for cutting tools where strength, hardness, and corrosion resistance are demanded. A blade with 13% Cr and 0.25% C is rustless which provides a healthy environment in kitchens and operation rooms in hospitals likewise. Experience has proved that stainless steel cutlery can remain shiny and sharp with the time.
- Food processing units; Usage of stainless steel for cutlery applications has paved the way into further implementation for food processing tools. Starting from the farm, hardenable stainless steel utilized to fabricate the blows that can resist the corrosive soil. Vessels made of 18-8 and 304 were used to store milk, wine, and fruit juices. It is so obvious to find many cooking utensils made as clad materials to avoid the poor heat conductivity of stainless steel relative to plain carbon steel, it is three times as conductive compared to austenitic stainless steel value.
- Chemical industry; Austenitic stainless steel is an ideal material to fabricate the storage vessels for many chemical substances such as organic acids, ammonia fertilizers, and alkalis. On the other hand, hydrochloride acid causes localized corrosion on austenitic stainless steel. Ferritic stainless steel has shown a better resistance to stress corrosion cracking in chloride iron environment. Austenitic stainless steel is a perfect resistant of sulphuric acids environment; however, superalloys are required for some application. While caustic soda is common material in many chemical industries, austenitic stainless steel has revealed an excellent result with caustic soda environment up to 50% concentration and temperature below 95 °C, while Ferritic stainless steel exposes to the risk of caustic stress-corrosion cracking.

- Heat exchanger; demanding application, caution is required when selecting the material to fulfill many aspects such as; withstand loads at elevated temperature, resist different corrosion environment beside the economic operation of heat exchangers. Austenitic stainless steel, ferritic stainless steel and duplex stainless steel are typical in the manufacturing of heat exchangers.
- Pulp and paper industry; Wood chips are transported to the factories in order to be treated in individual vessels known as digesters. Different chemicals like sodium sulphide and sodium hydroxide are added to digesters, which produce an aggressive corrosive environment. Stainless steel is being utilized in the paper and pulp industry since 1920, not only for digester repair work, also it is applicable for the evaporators, heaters, blander and smooth surfaces need.
- Automotive industry; generally automotive parts requires good strength, hardness, and corrosion resistance. Ford is the pioneer in replacing the malleable metal parts with stainless steel since 1930. They made the radiator shell, hubcaps, headlamp case and tie rods out of stainless steel. Later in 1965, 10kg of stainless steel contributed in each car manufacturing. By nineteen's century, 90% of the car manufacturers have introduced stainless steel. Recently stainless steel is the dominant material for seatbelt anchors, water pump seal, thermostat, fuel filter, air injection tubes, output shaft wear - sleeves and airbag components. Automotive exhaust system carries hot gases (up to 900°C) in addition to acidic contents and salt water that represents a corrosive environment. Exhaust system materials have evolved from mild steel and aluminum-mild steel into stainless steel in 2000 with four times lifetime and 1% failure probability. Ferritic stainless steel AISI 409 is the most prevalent grade for exhaust system parts. Hardened martensitic stainless steel is an appropriate option for the valves application.
- Turbine blades; turbines are most often placed in a high pressure and elevated temperature atmosphere. For steam and gas turbine, such conditions require martensitic stainless steel to achieve wear resistance, good strength, and corrosion resistance.

Demand for stainless steel is growing rapidly, faster than the other metals. Since 1990, there is a 5% annual increment. Western countries in addition to China and India are the dominant consumers of stainless steel. Figure 1 shows the share of different sectors in stainless steel

consumption in 2006. The industry was the prevailing field in China where in India, durable consumer represented the largest sector of stainless steel consumption. (Baddoo, 2008)

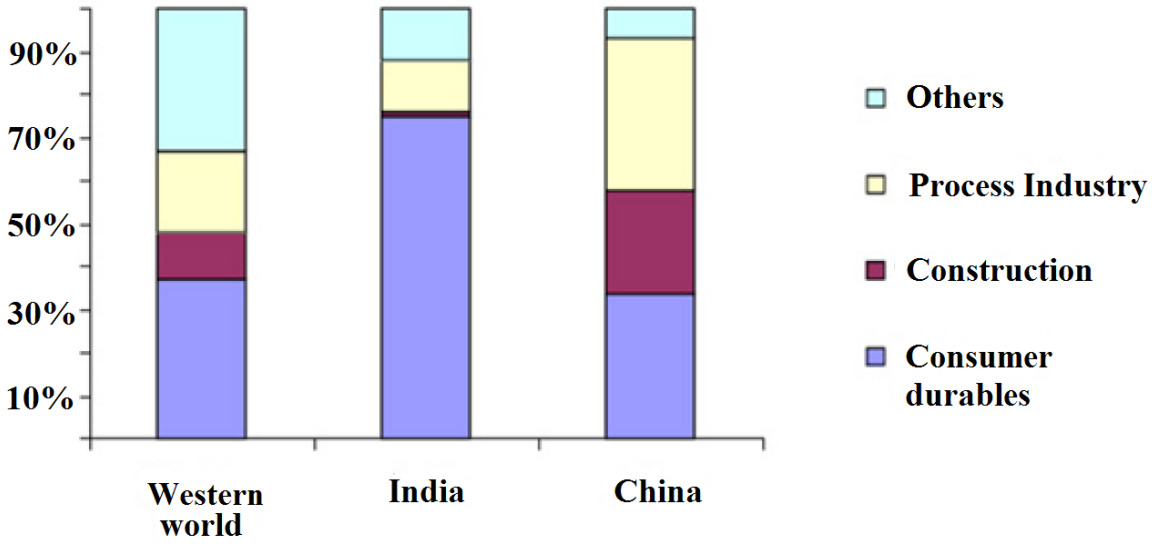

Figure 1. Consumption of stainless steel by sectors in India, China and the western world (Baddoo, 2008, p. 1200).

1.5 Previous researches in weldability of austenitic stainless steel

Investigating the weldability of materials is an interesting research topic for the welding researchers. Many researches discussed the influential factors on the weldability of austenitic stainless steel. Most of the published work focused on the effect of the welding parameters, shielding gases and filler material on the quality of the welded joints. Mostly, weldability has being evaluated based on the susceptibility of solidification cracking, final mechanical and physical properties of the weld joints. Nevertheless, minor interest has given to distortion.

Devendranath et al., (2015, pp.1602-1613) investigated the influence of filler metal on microstructure, mechanical properties and corrosion resistance of AISI 316L (X2CrNiMo17-12-2). Pulsed current tungsten inert gas has adopted as the primary welding process for the experiment. Charpy- V notch and tensile tests were carried out to examine the mechanical properties after welding. A close relation between the applied filler metal against the mechanical and physical properties of the welded joint has been proved.

Shankar et al., (2003) investigated the effect of shielding gas additives on the weldability of austenitic stainless steel 316L (X2CrNiMo17-12-2) and 3316LN (X2CrNiMoN17-11-2). V. Shankar and his colleagues from Indian Institute of Technology manipulated the amount of nitrogen in the shielding gas within the range (0.04 -0.19%). Longitudinal moving torch Varestraint test has been applied to evaluate the weldability. The study revealed the relationship between the impurity level and crack probability in presence of nitrogen.

Sowards et al., (2012) from the Mineral, Metal and Materials society with association with ASM International-USA, have published a beneficial study. The study has shown the effect of different filler material base on the metallurgical behaviours and solidification mode of austenitic stainless steel type 304L (X2CrNi18-9). Researchers found a proportional relation between the dilution of the austenitic stainless steel base and segregation of Ti, Cu, and Si. Applying of (cast pin tear) test proved an increment in the solidification cracking susceptibility with a higher dilution of 304L base metal because of the low solubility of those elements in austenite structure.

Younes et al., (2013) at University of Bristol-UK, have carried mechanical examinations to compare the strength of 304L stainless steel (X2CrNi19-11) welded by TIG and other samples joined with the electron beam (EB). Moreover, Younes et al, have exposed the tensile specimens to hydrogen gas in order to observe the effects of the different amount of H2 gas on the mechanical properties. Hydrogen addition has improved the tensile strength and the yield strength. However, it has reduced the ductility; it also changed the fracture mode and initiated cracks near the austenite-ferrite interface. Hydrogen embrittlement found to be higher with TIG process.

1.6 Welding challenges of austenitic stainless steel

Austenitic stainless steel is a conservative heat material due to the low thermal conductivity; it is about one-third the value of plain carbon steel, which is a positive property in welding and makes weldability of austenitic stainless steel excellent with minor cautions. Most of the welding processes are applicable for joining austenitic stainless steel. The current research studies part of the drawbacks associated with welding of austenitic stainless steel, and correlation with the welding parameters.

Welding parameters beside the chemical composition represent the most significant influential factors on the weldability of austenitic stainless steel. Cleanliness and proper filler material are essential parameters to ensure the soundness of the welded parts made of austenitic stainless steel. Heat input should be kept in the minimum possible level when welding austenitic stainless steel, to minimize the risk of sensitization, distortion and hot cracking. As per the European standard (EN 1011-3: 2001, pp.17-23); the following defects are expected when welding the austenitic stainless steel.

- Hot cracking: due to the presence of impurities and segregation to interdendritic regions. Ferritic solidification-mode substantially prevents the formation of hot cracks; it dissolves the elements with a high tendency of segregation such as phosphor and sulphur. Ductility of ferrite structure is superior to austenite at elevated temperature. Moreover, ferrite has a lower coefficient of thermal expansion (Shankar, et al., 2003). However, ferrite-phase may reduce the corrosion resistance of austenitic stainless steel in presence of specific environments; moreover, ferrite lowers the ductility at the temperature range (550-900°C) due to the formation of "Sigma phase". Annealing (1100°C) is an effective way to dissolve the ferrite and enhance austenite-phase beside the proper selection of the filler material. (Weman, 2012, p. 200) The shape of the weld pool effects the susceptibility for centreline cracking, teardrop shape produced by fast travel speed is not recommended.
- Sensitization: formation of chromium carbides, which accumulates on grain boundaries and reduce corrosion resistance. Higher carbon concentration enhances the formation of the carbides (Weman, 2012, p. 200)
- Stress corrosion cracks: environmental phenomena occurs when steel exposed to aggressive corrosive media such as halide at an elevated temperature in the presence of tensile stresses (residual stresses from welding or grinding). Austenitic stainless steel exposed to stress corrosion cracks.
- Distortion: it can be defined as any geometrical deviation produced from the welding stresses, expansion – contraction. This research investigates the distortion and its connection with the welding process and welding parameters. Distortion is a common defect in welding, wherein the shipbuilding industry; 20-30% of the weight of labour job is reworking due to the welding distortion (Cao, et al., 2017, p. 2). Distortion is highly anticipated when welding austenitic stainless steel due to the low thermal conductivity and high coefficient of thermal expansion.

On the parent metal adjacent to the weld bead, another type of chromium depletion can occur because of carbides dissolve at the elevated temperature. Subsequently, these carbides are not able to reform, and some carbon remains in solid state and combine with chromium at the formation range of chromium carbide when interpass temperature or post heat treatment is applied. Consumption of the chromium reduces the corrosion resistance. The phenomenon is known as the knife-line attack.

1.7 Research objective

The objective of the current research is to evaluate the weldability of austenitic stainless steel in terms of distortion and sensitization to intergranular corrosion because of the welding heat. Austenitic stainless steel suppresses the heat transfer due to the poor thermal conductivity. Austenitic stainless steel characterized by a high coefficient of thermal expansion. Therefore it becomes highly exposed to distortion as a consequence of the welding process. Distortion is a significant concern in welded structures, it changes the physical geometry and leads to fit up failure; it promotes residual stresses, which can produce defect for the entire application or construction, in most cases distortion requires corrective maintenance, which is costly and time-consuming process.

All the mentioned demerits of distortion make studying the effects of welding parameters on distortion for austenitic stainless steel interesting. This research aims to determine the most appropriate welding process (MAG- LB) for joining austenitic stainless steel in order to minimize the probability of distortion. Additionally, the study has applied Different welding parameters to examine the effect of heat inputs on deformation and intergranular corrosion as well.

1.8 Research problem

Arc welding processes apply concentrated heat to the weld pool to ensure the fusion. During welding, the applied heat leads to expansion at the heat-affected zone (HAZ) and compression in the base metal. After welding and during the cooling stage, contraction takes place in HAZ and tensile stresses at the base metal area. Therefore, non-uniform stress produces at the weld joint, which known as residual stress.

When residual stresses exceed the yield strength of the parent metal, plastic deformation or distortion takes place. This phenomenon is highly connected to austenitic stainless steel due to poor thermal conductivity and high coefficient of thermal expansion.

Distortion is unfavourable in the welded structures; it impairs the geometry, which affects the assembly and functionability. Distortion reduces the fatigue strength and minimizes the load capacity of the component (Radaj, 1992, p. 247).

1.9 Research questions

The main research question:

- Which welding process (MAG-Laser) is more suitable for joining austenitic stainless steel to achieve a sound weld and mitigate distortion?

Research sub-questions:

1- What is the effect of the introduced heat through the welding process on the produced distortion?
2- What is the effect of the introduced heat on the corrosion resistance of austenitic stainless steel?
3- What is the effect of mechanical constraints on preventing distortion?

1.10 Implementation methods of the research

The research adopts both qualitative and quantitative method to answer the research questions. Laboratory tests have been done by welding 3mm thick austenitic stainless steel sheet applying MAG, and laser welding processes. Distortion has been measured using 2D-laser device with high sensitivity. The quantitative method depends on measuring the magnitude of distortion in the different welding processes at different heat inputs.

The result has been analysed numerically. Research implements SEM to detect the formation of carbides as a qualitative analysis method for corrosion resistance investigation. In addition to Energy dispersive spectroscopy (ESD) to measure the concentration of the alloying elements for the indications as a quantitative method for evaluation of resistance the intergranular corrosion.

2 WELDING PROCESSES

The welding process is a fabrication method for joining metals or thermoplastics through the coalescence of adjacent parts. Fusion welding and solid state welding are the main categories of the welding processes. For fusion welding, the electrical power source, filler material, and the shielding technique represent the essential components of the process. For fusion welding, the base material melts and solidifies either with or without a filler material in order to form the weld joint. The electrical source is essential to create the arc and provide the required heat for melting. Shielding gas is substantial for protecting the weld pool from air gases contamination that affects the quality of the weld joint. There are dozens of different welding processes varies in their application according to the welded material, essential quality, time and cost. This part of the research discusses part of the welding processes applied for joining austenitic stainless steel.

2.1 Gas metal arc welding process (GMAW)

Recently, it became the dominant process in welding for different engineering applications. GMAW covers a wide range of materials from constructional steel, stainless steel and malleable metals, mainly Aluminium and copper. Known as MIG process when pure inert gas utilizes for shielding or MAG process when shielding gas contains an active gas such as CO_2. GMAW is feasible for welding of the thin sheets due to low heat input. Although it achieves high productivity for thick plates. (Weman, 2012, pp. 41-48)

GMAW process had applied commercially for the first time in 1948 for welding aluminium with inert shielding gas, the process known as metal inert gas (MIG). Later the process replaced the conventional stick welding known as SMAW (Shielded Metal Arc Welding) for many considerations; it ensures greater productivity due to continuous wire feed and higher welding speed. GMAW has to be equipped with power source, wire feed system, shielding gas cylinder and regulator, water-cooling system and welding gun. Welding gun combines the wire electrode, shielding gas and electrical cable in one nozzle that manipulated either by the welder or by a robot to control the welding speed and direction. (Harris, et al., 2004)

Figure (2) shows the essential equipment of the GMAW process in a semiautomatic mode, where a welder is required to hold the welding gun.

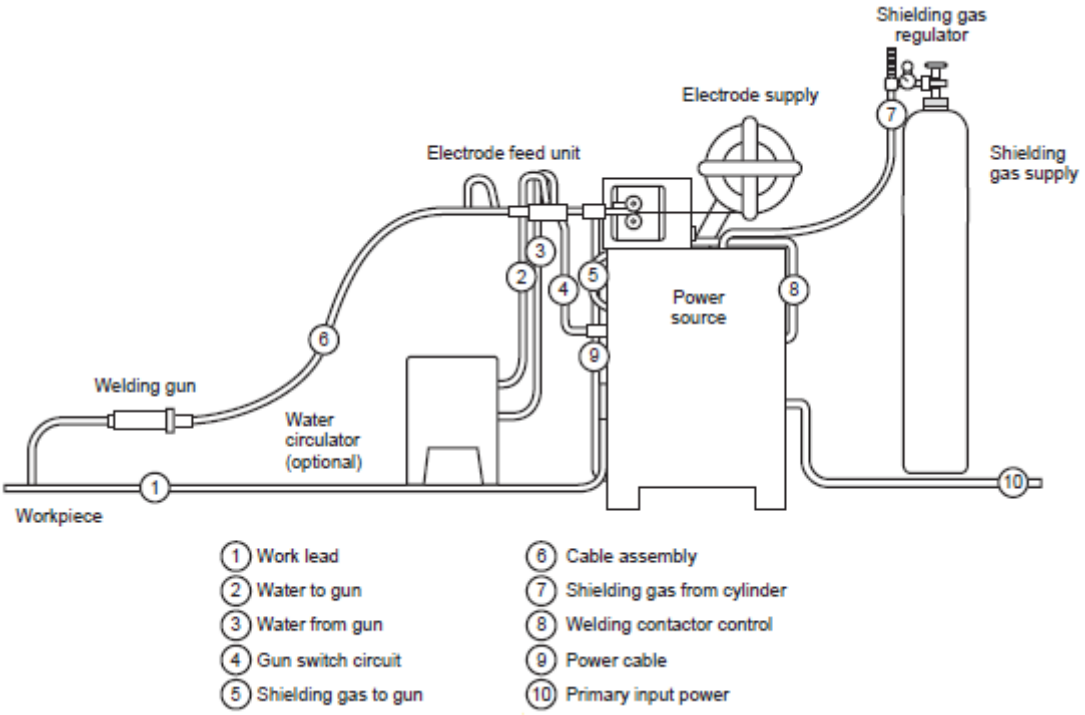

Figure 2. Basic equipment for gas metal arc welding process (Harris, et al., 2004).

2.1.1 Metal transfer modes in GMAW

Transfer mode refers to the manner in which the material from the fused electrode transfers to the workpiece. Several parameters control the metal transfer mode, basically, the magnitude of the welding current, type of the current, polarity, shielding gas, electrode diameter, and components. (Harris, et al., 2004) There are several modes of metal transfer; the following is a brief illustration of primary modes as elaborated by the welding handbook committee.

- Short circuit transfer mode: this mode of metal transfer in GMAW process apply the lowest welding current among the others. Electrode diameter is small, and the voltage is low. Consequently, the droplet does not leave the wire tip unless it touches the weld pool. Current and volt cycle divided into two periods, short circuit period while the wire tip is touching the weld pool and the arc period when a gap is present between the wire tip and workpiece, and current is relatively lower. The produced

weld is small and solidifies rapidly thus; it is appropriate for joining thin plates and for bridging when the root opening is big. Type of the shielding gas has a significant effect on the quality of the weld joint. CO_2 improves the penetration; however, it promotes the spatter. Therefore, the ideal shielding that ensures excellent penetration and less spatter is a commingle of CO_2 with an inert gas such as argon or helium.

- Globular transfer mode: droplet size with a diameter greater than electrode one, passes the arc towards the weld pool. Gravity force influences the droplet detachment out of the wire-tip. The current range is higher than short-circuit; optimal arc length is required, while concise length leads to droplet touch of the workpiece which produce spatter. On the other hand, the long arc is not recommended due to the produced weld defects such as lack of fusion, lack of penetration and excess reinforcement consequent to the high voltage. This complication limits the utilization of globular transfer mode.

  Axial drop out of the electrode is substantial for minimizing spatter. Two forces, the electromagnetic force created from the current flow on the electrode and the anode reaction force in the opposite direction control axial transfer. The resultant force is known as electromagnetic pinch force responsible for the droplet necking before detaching from the electrode.

- Spray metal transfer mode: tiny droplets fall axially on the workpiece in steady mode creating the minimal rate of spatter relatively. Direct current-positive electrode (DCEP) is appropriate to achieve spray mode. Current has to be above a certain critical level to ensure the spray transfer; beneath the critical level, the transfer mode is globular. Different factors control the critical current such as electrode diameter, electrode material, and shielding gas. Table 2 presents the minimum spray arc current for variant material with different electrode size. It is evident that the required transition current is higher when electrode diameter increases. Droplet size in spray transfer mode is less than it is in globular mode, however; the transfer rate or the number of detached drops per second is higher for the spray transfer mode. Spray transfer is appropriate for the thick plate due to the high current applied to achieve the spray mode.

Table 2. Minimum required current (Transition current) for spray transfer mode ("mod." *Harris, et al., 2004, p. 155).*

Electrode-Material	Electrode-Dia. (mm)	Shielding gas	Transition current-A
Mild steel	0.8	98%Argon - 2%O_2	150
Mild steel	0.9	98%Argon - 2%O_2	165
Mild steel	1.1	98%Argon - 2%O_2	220
Mild steel	1.6	98%Argon - 2%O_2	275
Stainless steel	0.9	98%Argon - 2%O_2	170
Stainless steel	1.1	98%Argon - 2%O_2	225
Stainless steel	1.6	98%Argon - 2%O_2	285
Aluminium	0.8	Argon	95
Aluminium	1.1	Argon	135
Aluminium	1.6	Argon	180
Deoxidized copper	0.9	Argon	180
Deoxidized copper	1.1	Argon	210
Deoxidized copper	1.6	Argon	310
Silicon bronze	0.9	Argon	165
Silicon bronze	1.1	Argon	205
Silicon bronze	1.6	Argon	270

Figure 3 shows the different modes of metal transfer in GMAW. Short circuit, globular, spray and pulse - spray transfer modes. Pulsed gas metal arc welding (P-GMAW) is the most preferable transfer mode for the heat-sensitive materials such as austenitic stainless steel due to the relatively high coefficient of thermal expansion compared to structural steel. Proper selection of pulse parameters in P-GMAW produces a high-quality weld in ASS. Efficient energy distribution in the arc ensures a minimal heat build-up in the weld pool. Consequently, less stress accumulation, which reduces the probability of distortion because of the introduced heat during welding. (Ghosh, et al., 2009, pp. 1262-1263)

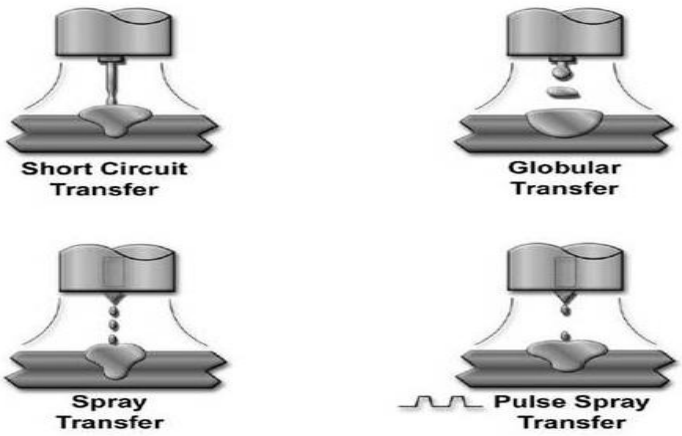

Figure 3. Metal transfer modes in gas metal arc welding process (Slane, 2010)

2.1.2 GMAW process for joining austenitic stainless steel.

As discussed in the introduction, austenitic stainless steel characterized by good weldability among the other types of stainless steels. The thermal and mechanical properties improve the weldability of austenitic stainless steel. Nevertheless, it is sensitive to the magnitude of heat input during welding process that can initiate hot cracking and leads to "Distortion" which is the primary concern of the current research. Research hypothesis; a Higher amount of induced heat during welding of austenitic stainless steel enhances the occurrence of chromium carbides on the grain boundaries (Sensitization), controlled heat input of GMAW and the wide range of parameters makes the process attractive for joining austenitic stainless steel exceptionally thin sheets where minimal heat is targeted. GMAW has proved reasonable results for welding austenitic stainless steel, this part discussing some of the practical cases.

Cabrera et al., (2009) have investigated the effect of different metal transfer mode (Pulse arc and short circuit) of GMAW on the fatigue life of 316L stainless steel. Different combination of shielding gas (Ar/O_2) has been examined. 316L stainless steel is a common material in the highly corrosive industries such as textile, pulp and paper factories where aggressive chemical agents are involved.

The material showed excellent yield strength. Therefore it is an appropriate selection for nuclear and chemical plants where high pressure exists in addition to the corrosive environment. The unique ductility of 316L stainless steel at low temperatures enhances it is utilization in cryogenic temperatures equipment. Through the study, four parameters have been investigated, after preparation of four butt-weld joints (V-groove, opening angle 60°, root opening 1.2mm), each one consist of two plates with dimensions 125x400x6mm. A couple of samples have been welded by applying pulse-arc transfer mode, one with shielding gas consist of $Ar/1\%O_2$ and the other one $Ar/5\%O_2$, the other two samples were welded with short-circuit metal transfer and same combination of shielding gas. (Puchi-Cabrera, et al., 2009)

Fatigue life chart has been obtained based on Seven test pieces with two different combinations of shielding gas (1% O_2 and 5% O_2). The same sequence has followed for both modes of metal transfer, pulse-arc and short-circuit. It is an evident that, lower O_2 content in

the shielding gas higher fatigue strength. Figure 4 presents a chart for the fatigue life in term of the required number of cycles to failure for a welded joint, two modes of metal transfer were used in the experiment, short circuit and pulse arc with different oxygen percentage in the shielding gas. Values of the number of fatigue cycles on the chart represent the average value for the seven test pieces. (Puchi-Cabrera, et al., 2009, pp. 779-782) It can be seen from the figure that the O_2 addition to the shielding gas for welding of 316L stainless steel has reduced the fatigue life regardless the metal transfer mode, either it was the short-circuiting mode or pulsed arc. A small addition in the O_2 percentage to the shielding gas drops the fatigue life significantly.

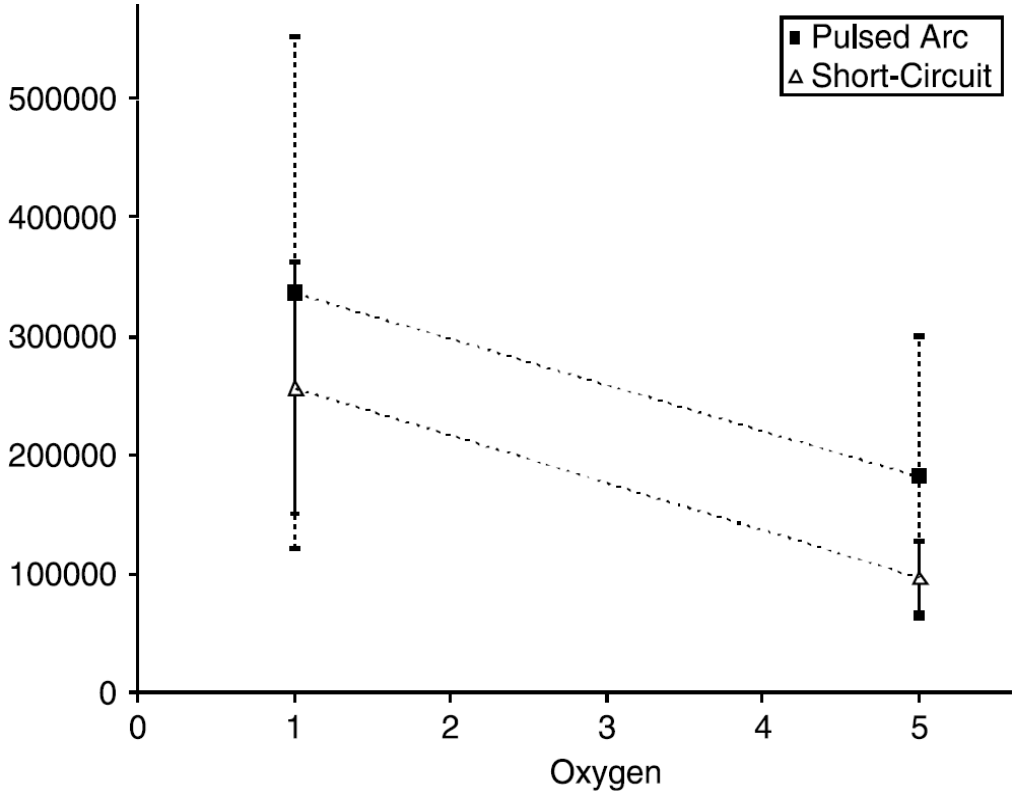

Figure 4. Effect of metal transfer mode and O_2 percentage in the shielding gas on fatigue life of 316L stainless steel (Puchi-Cabrera, et al., 2009, p. 782).

The pulse-arc metal transfer showed higher radius of curvature between the weld toe and the base material compare to the short-circuit mode. Consequently, the fatigue strength is higher for the pulse arc. For short circuit, the curvature is smaller and probability of stress concentration is higher. The O_2 percentage in the shielding gas affects the radius of curvature likewise. Weld joints created with 1% O_2 showed the bigger radius of curvature.

Table 3 shows the different radius of curvatures measured in four different zones for both modes of metal transfer with 1%O_2 and 5% O_2. (Puchi-Cabrera, et al., 2009) It can be extrapolated from the table that the higher percentage of O_2 in the shielding gas reduces the radius of curvatures which accumulate the stresses and reduces the fatigue strength.

Table 3. Effect of oxygen percentage in the shielding gas and mode of metal transfer on the radius of curvature. 316L stainless steel butt-weld joints. ("Mod." Puchi-Cabrera, et al., 2009, p.783)

Measurement zone	Radius of curvature (mm)			
	Pulsed arc		Short circuit	
	Ar/1%O_2	Ar/5%O_2	Ar/1%O_2	Ar/5%O_2
1	20.80 ± 7.1	4.02 ± 3.51	17.8 ± 8.59	4.51 ± 2.58
2	29.00 ± 24.1	5.53 ± 5.35	18.3 ± 6.66	3.26 ± 2.81
3	5.12 ± 5.83	5.18 ± 9.00	5.17 ± 2.62	1.48 ± 2.05
4	7.46 ± 6.39	3.54 ± 4.16	1.73 ± 1.48	1.00 ± 0.71

For accurate estimation of the weldability of austenitic stainless steel, it is essential to realize the complicated relationship between the microstructure of the weld zone, mechanical properties and resistance to corrosion. Alloying elements have considerable influence on the mechanical properties and corrosion resistance of austenitic stainless steel. For instance, nitrogen (N) is substantial for high mechanical behavior at cryogenic temperatures, superior austenite phase stabilizer, also, N enhances corrosion resistance at specific environments (Trevisan, et al., 2003, p. 298). Presence of δ-ferrite phase in the weld zone resists the formation of hot cracking, while it affects the superior properties of austenitic stainless steel.

N is a convenient alternative for nickel (Ni) in austenitic stainless steel due to the lower price of N in addition to the superiority in stabilizing austenite phase in the welded joint in comparison to Ni. Lately, the trend is to replace the carbon content in stainless steel with nitrogen to eliminate sensitization. Though, the higher precipitation of N in the weld zone decreases the δ-ferrite phase, 0.18% of N in the weld zone leads to the vanishing off the δ-ferrite phase. (Trevisan, et al., 2003, pp. 298-299)

To realize the effect on N addition to the shielding gas on the weldability of stainless steel, Tervisan et al., (2003) have implemented an experiment applying pulse-gas arc welding process with a flux cored electrode (FCAW) to join AISI 316L austenitic stainless steel plates (260 X 160 X 9.5mm), U bevel, butt-joint. Four percentages on N were added to the base shielding gas CO_2 (0%, 5%, 10% and 15%). Wire electrode was AWS E316LT-1, 1.6 mm diameter. Three mean pulsed currents were applied (150A, 200A, and 250A). The transvarestraint test was implemented to enhance the cracks forming to estimate the weldability with a different set of parameters and microscopic investigation were conducted to measure the cracking.

The results from the microscopic images for the total length of solidification cracks and magnitude of δ-ferrite phase in the weld zone in addition to the N percentages shows that:

- Amount of δ-ferrite phase decreases with the higher percentages of N gas in the composition of the shielding gas; the reduction percentage is higher when the mean pulse current is lower. Figure 5 presents the obtained relation between N amount in the shielding gas, the formation of δ-ferrite in the weld zone, the total length of the solidification crack (LTG) and amount of N in the weld joint for three different mean pulse currents 150A, 200A and 250A.
- The presence of the N element in the final composition of the weld zone is directly proportional to the percentage of N_2 in the shielding gas.
- The total length of solidification cracks formed in the centerline of the weld zone, decrease when a higher amount of N_2 exists in the formation of the shielding gas. This result is a contravention to the fact that, δ-ferrite phase presence in the weld zone resists the formation of solidification cracks.

An extra part of the experiment examined the effect of the pulse current value on the total length of solidification crack when pure CO_2 utilized for shielding. Results reveal that the crack is more significant when the mean pulse current is lower. Figure 6 shows the relation between the total length of the crack and the mean pulse welding current.

Another extrapolation from figure 5, that the content of the ferrite phase is greater when the mean pulse current is higher, which can be justified by the long cooling time, whereas austenite phase has more time to transfer into ferrite phase (Trevisan, et al., 2003).

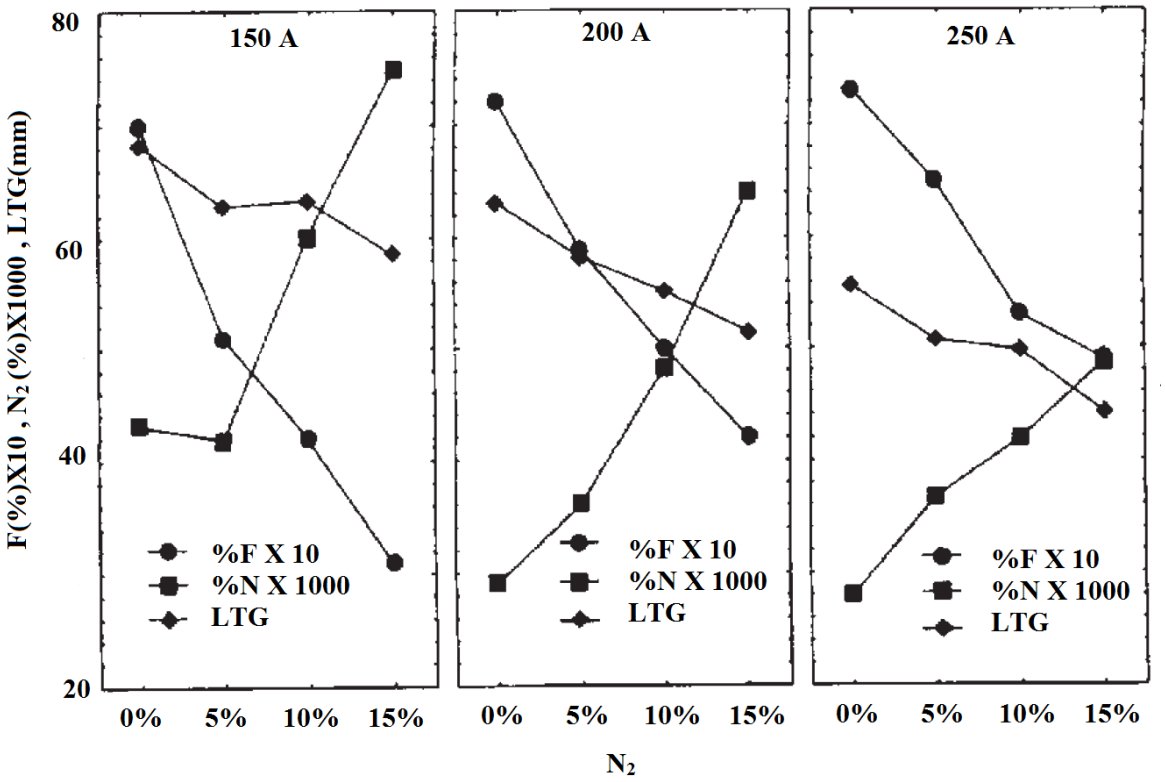

Figure 5. Correlation between N_2 addition to CO_2 shielding gas, the formation of δ-ferrite (F %), solidification crack (LTG), mean pulse current (A) and deposited N into the weld pool (Trevisan, et al., 2003, p. 300).

Figure 6 is derived from figure 5 to illustrate the correlation between the welding current and the total crack length, it can be seen that, lower the welding current, greater the produced crack.

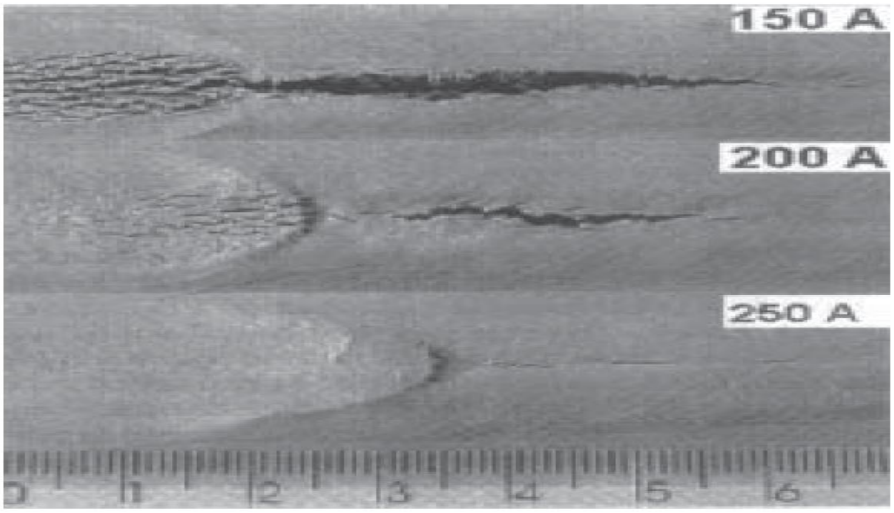

Figure 6. Effects of current intensity on the total crack length (Trevisan, et al., 2003, p. 300).

Table 4 shows the chemical composition by weight percentage of the welded joints obtained with a different N_2 percentage in the shielding gas for variable welding currents. It is evident on the table, N concentration in the weld zone decreases with higher current for all percentage of N_2 in the shielding gas. The table shows that nitrogen concentration increases with the higher amount of N_2 percentage in the shielding gas. (Trevisan, et al., 2003, pp. 300-301)

Table 4. The chemical composition of 316L austenitic stainless steel welded joint obtained with a different N_2 percentage in the shielding gas for variable welding currents (Trevisan, et al., 2003, p. 301)

N_2 in the CO_2(%)	Icm(a)	C	S	N	Cr	Mn	Mo	Ni	Si	Cu	P
15	150	0.0311	0.0046	0.0746	17.81	1.28	2.30	12.10	0.58	0.038	0.033
	200	0.0329	0.0037	0.0638	17.93	1.31	2.34	12.09	0.40	0.036	0.034
	250	0.0322	0.0030	0.0484	18.33	1.39	2.37	12.35	0.36	0.038	0.031
10	150	0.0321	0.0046	0.0602	17.90	1.29	2.40	12.26	0.38	0.036	0.035
	200	0.0385	0.0040	0.0484	18.27	1.35	2.31	12.36	0.59	0.037	0.033
	250	0.0362	0.0043	0.0410	18.10	1.36	2.40	12.24	0.46	0.035	0.033
5	150	0.0361	0.0041	0.0411	17.97	1.29	2.35	12.27	0.60	0.036	0.034
	200	0.0346	0.0037	0.0360	18.25	1.34	2.43	12.44	0.32	0.036	0.036
	250	0.0362	0.0041	0.0363	17.84	1.33	2.35	12.11	0.46	0.036	0.035
pure CO_2	150	0.0354	0.0038	0.0424	17.90	1.23	2.35	12.36	0.60	0.036	0.034
	200	0.0367	0.0038	0.0292	18.16	1.31	2.38	12.45	0.61	0.036	0.037
	250	0.0296	0.0039	0.0283	18.23	1.35	2.37	12.36	0.59	0.036	0.036
	MB	0.0260	0.0008	0.0351	17.60	1.35	1.94	10.50	0.26	0.07	0.021

2.2 Laser beam welding process (LBW)

Specific properties make laser an ideal alternative for special welding conditions. The laser produces a highly concentrated beam of oriented power; this concentrated power can easily be transferred to the welding position via particular conducting media such as mirrors and glass fibers. Laser power is focused on the surface of the weld joint, little higher or little below to melt at the incident location. Melting produces vapourised metal that creates a plasma gas useful to improves the energy absorption in addition to protect the laser equipment such as the mirrors or lenses for weld spatter and vapourised metal. (Weman, 2012, p. 136)

Laser welding is similar to plasma welding in producing the keyhole when for a butt joint, which ensures deep penetration and makes welding of thicker section affordable. In the keyhole technique, laser beam penetrates through the joint thickness then molten metal solidifies backward to fill the hole. In addition to deep penetration laser welding applies low heat input which spread the heat through small distance beside the joint and produces small HAZ. Laser welding is preferable when low heat input is required, for instance, welding of stainless steel and high strength/hardened steel and for the joining of thin sheets. (Weman, 2012, pp. 95-96)

Different parameters control the quality of the joint produced by laser welding; focal point, laser beam travel speed, power intensity and type of laser. For the laser type, there are four main categories as classified by Weman (2012) stated below.

- CO_2 Laser: laser light transferred via a tube where different gases including CO_2 flows with relatively high wavelength up to 10.6 μm. Excellent energy efficiency, whereas small electric energy, can produce high laser power capable for accomplishing welding and cutting processes. Laser light reflected on the weld joint using mirrors or lens, and shielding gas is mandatory to protect both lens and weld joint. High power of CO_2 Laser renders it capable to weld thick plates up to 26mm. CO_2 Laser application is limited to the welded material, while metals like copper, aluminum, gold, silver, and magnesium reflect a portion of the incident light which reduce the efficiency and weldability.
- Nd: YAG Laser: energy transferred through a flash tube with small wavelength (1.06 μm) while the wavelength is short, fiber optics and lens can be used to carry and focus the laser light. Appropriate for low –weldability materials such as titanium and zirconium, limited to the thickness (up to 6mm) due to low energy output compare to CO_2 laser. Severe health concern relative to the eye is connected to Nd: YAG Laser welding.
- Fibre Laser: fiberglass represents the transferring medium, it produces a laser beam with high quality. Produced power magnitude and concentration are relatively high in comparison to other types of laser welding. Short wavelength closer to Nd: YAG Laser.

  High power-Fiber laser welding provides higher welding speed, lower heat input, and deeper penetration compared to traditional arc welding processes. Thus, it is a

favourable process for application and materials susceptible to welding distortion such as shipbuilding. (Cao, et al., 2017, p. 2)

- Laser-hybrid welding: it is a dual welding process encompasses the laser welding in addition to arc welding process (MIG, Plasma…) each process has a role, arc welding process fills the gap by providing the filler material and apply high heat input while laser welding ensures the stability and penetration. The process is ideal when thick welding plates and less heat input is required. Deep penetration reduces the number of welding passes.

Figure 7 shows the key-hole welding process where higher depth to width ratio can be achieved up to 10:1, which makes the process is ideal for deep penetration application. Uniform fusion of the key-hole process and high accuracy, reduces distortion which renders the process is appropriate for welding of austenitic stainless steel. (Sokolov & Salminen, 2014, p. 560).

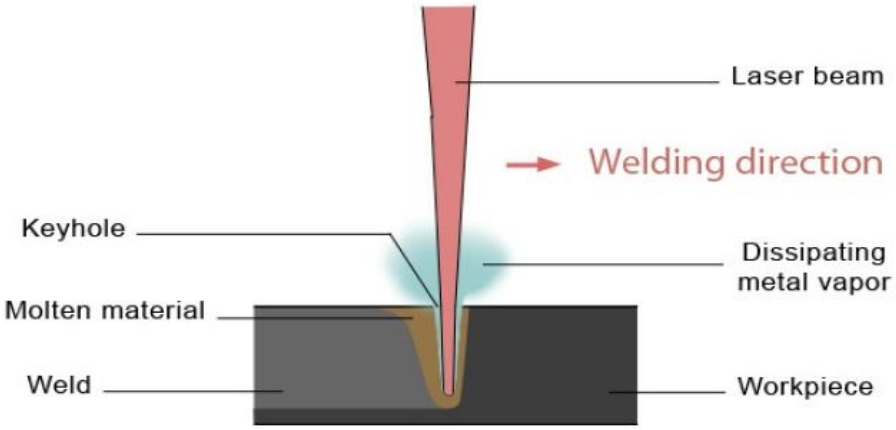

Figure 7. keyhole welding process (Sokolov & Salminen, 2014, p. 560).

2.2.1 Effect of different laser processes and parameters on weld quality of austenitic SS

Laser energy can be transferred to the weld joint either in a continuous wave (CW) mode or pulsed mode. Each mode has its advantage, CW mode is appropriate for deep penetration or thick plates where keyhole exists, however, the major drawback of CW is the energy dissipation through a vast distance which increases the heat load and tends to produce distortion. Pulse mode is utilized for welding of thin sheets and when less heat input is required. Different parameters control the quality of laser joint, essentially the heat input,

welding speed, focal point, weld geometry in addition to pulse width, pulse frequency, peak and average power for pulse mode laser welding. (Gietzelt, et al., 2015, p. 2196)

Gietzelt et al. (2015) have investigated the effect of the laser welding technological parameters on the cross-sectional shape of the produced weld. Figure 8 shows the poor penetration produced from the high defocusing (+ values) in section (a) of the figure. It reveals likewise the triangular shape of weld section obtained by pulse mode (b) and the difference in the weld dimensions (depth and width) when tunning the welding speed. In (c) the welding speed is relatively low compared to (d).

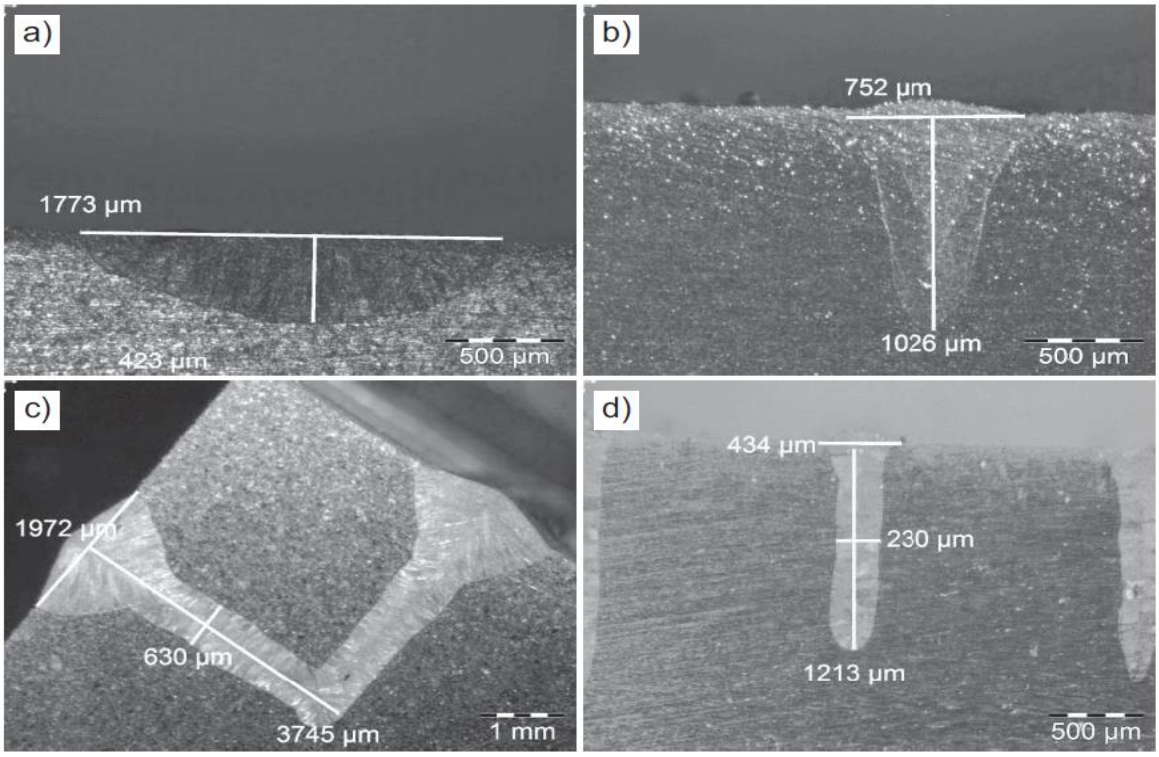

Figure 8. The difference in 304SS laser welds cross sections obtained by different weld technological parameters (Gietzelt, et al., 2015, p. 2190).

Researchers have implemented dozens of experiments on 304SS with laser pulsed welding to evaluate the most affecting factors on the weld seam dimensions. A conclusion has reached, that a combination of several factors in varying proportions are responsible for the weld seam dimensions with different, influential factors are:

- Heat input per unit length – affects depth of weld
- Pulse duration and peak power – significant effect on the weld seam depth

- Frequency – minor effect
- Average power – significant effect on both, width and depth
- Focal position – controls depth more than the width

Table 5 reveals the influence of the focal position on the weld seam dimensions. It is clearly observed that the depth of the seam has dropped significantly with the changing of the focal position from 2mm beneath the surface of the weld to 2mm above the surface, the experiment has accomplished with 150W as an average power, welding speed of 0.2 m min^{-1} and frequency 15 Hz.

Table 5. Influence of focal position (F) on the laser weld seam dimensions("Mod." Gietzelt, et al., 2015, p.2193).

Focal position (mm)	Width (µm)	Depth (µm)	Width at 50% of the depth (µm)
-2	1225	1715	500
	1225	1700	485
-1	1320	1445	535
	1405	1385	570
0	1420	1185	575
	1370	1235	580
1	1345	905	460
	1415	920	475
2	1220	560	490
	1105	515	530

Another research team from China (Zhang, et al., 2013, pp. 136-143) has studied the effect of different laser welding technique (CO_2 Laser, Nd:YAG and fiber laser) on residual stress, macro hardness and tensile properties of 304 stainless steel 5mm. The effect of focal position, laser power and welding speed on the quality of the weld joint has investigated.

3 RESIDUAL STRESSES AND DISTORTION

Residual or delayed stresses are inevitable in welding, it has a significant influence on the welded joints. Most importantly, it reduces the loading capacity, which can lead to unexpected failure and catastrophic damages. Residual stresses divided into two main types; tensile residual stress and compressive residual stress, both types are common in welded structures. Residual stresses produced from the thermal effect of welding. Therefore, it has been classified as secondary stresses on some occasions. Accordingly, residual stresses can be defined as the remaining stresses in the structure after completion of the welding process even with an absence of external loads. (Nasir, et al., 2016, pp. 6166-6167)

3.1 Residual stress in welding

For fusion welding processes, heat applies intensively in the weld pool in order to melt the adjacent base metal and the filler material. The high temperature of the weld pool creates expansion at the edges of the weld joint and consequently contraction at the adjacent area (Heat affected zone or base metal). After welding and during weld - pool solidification stage, coalescence metal starts to shrink producing contraction forces in the weld pool and expansion at HAZ. Heating rate and cooling rate or by other mean, expansion and contraction are not uniform along the weld joint. The differential heating and cooling rates along the depth of the weld piece creates a volumetric change then residual stresses take place subsequently.

The resultant of the non-uniform stresses are either tensile residual stress, or compressive residual stress depend on the magnitude of each type. Other classification of the residual stresses based on the scale; "Macro and Micro". Macro stress considered in scale greater the grain size and it produced as a result of non-uniform expansion and contraction or different cooling rate, while micro stress generated due to phase transformation, for instance, austenite to martensitic transformation. (Nasir, et al., 2016, pp. 6166-6167)

Residual stresses are not permanently detrimental. Whereas, the compression residual stress enhances the fatigue strength and corrosion resistance, however, it reduces the stability.

While tension stresses have the opposite effects, it lowers the fatigue strength and corrosion resistance and improves the stability. (Radaj, 1992, p. 247)

Many factors control the type and distribution of the involved residual stresses as mentioned by R.H Leggatt in Cambridge-UK (2008, p.144)

- Existing residual stresses before the welding process as a consequence of other manufacturing processes.
- Base and filler material properties including the chemical composition, thermal properties, and mechanical properties.
- Weld joint geometry.
- Applied restrains for positioning the components during welding.
- Produced stress after the welding process such as thermos-mechanical treatment.
- Welding parameters and welding preparation.

Figure 9 shows the distribution of the residual stresses in a butt joint. Tensile residual stress located at the weld metal (WM) and HAZ where compressive residual stress exists at the base metal (BM). However, it does not represent a permanent condition while compressive residual stress may found at HAZ. (Nasir, et al., 2016, p. 6168)

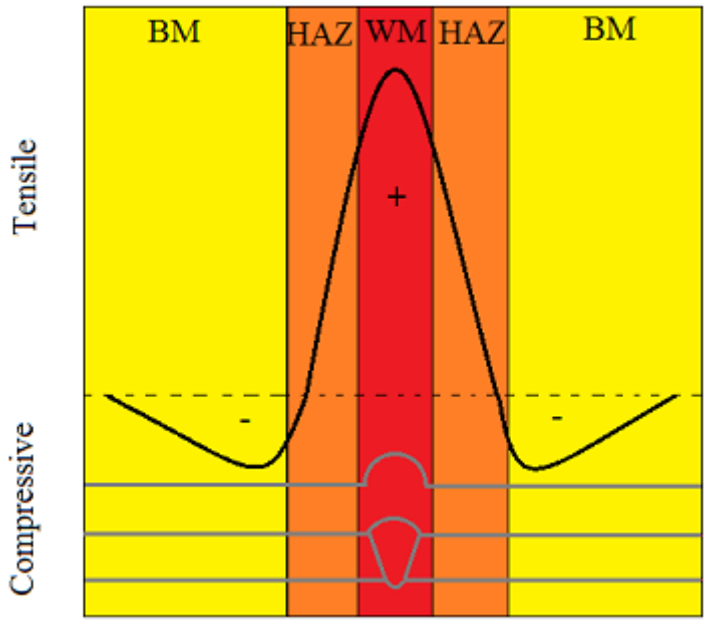

Figure 9. Distribution of residual stresses on a butt joint ("Mod." Nasir, et al., 2016, p. 6168).

Pre-welding residual stress produced by the mechanical and thermal processes applied during the material fabrication phase. It is recommended to measure those stresses away from the weld joint to consider them for evaluating the welding residual stresses. (Leggatt, 2008, p. 145)

3.2 Effect of welding conditions on residual stresses

Teng and Lin (1998 pp. 859-863) have created a finite element model for rectangular plate-butt weld joint to study the effect of different welding conditions on the magnitude and distribution of residual stresses.

Different length of the rectangular plate has been tested, 50mm, 100mm, 200mm, and 400mm. It has been proved that the transverse tensile residual stress at the center of the specimen decreases with the longer specimen. Different specimen thicknesses (5mm, 8mm, and 12mm) were tested and residual stress was greater with the thicker plate. In addition to the plate length and thickness, welds were produced with various speeds (3.33 mm/s, 7 mm/s, and 10 mm/s), while the higher welding speed reduces the width of the adjacent area affected by the welding heat, it has also reduced the residual stresses. Furthermore, it is found that the restrains increases the magnitude of residual stresses. Preheating were applied with different values (200°C, 300°C and 400°C), the result reveals that transverse residual stress decreases dramatically after the preheating process. (Teng & Lin, 1998, pp. 859-863)

Residual stresses up to certain limit remain within the elastic deformation range of the material. Any addition of the magnitude of residual stresses greater than the material yield strength, plastic deformation takes place and distortion produced at the welded structure because of the tremendous residual stress.

3.3 Influence of residual stresses on corrosion resistance

Corrosion resistance is the fundamental characteristic for materials selection to meet the corrosive environment applications. For instance, austenitic stainless steel resists different corrosive environment though, it is susceptible to stress corrosion cracking (SSC) in chloride and sulphide environment at the presence of residual stresses (Verneau & Mecozzi, 2000). A report issued by the European Commission in 1998 has studied the effect of residual stresses on the creation of SCC in 304L austenitic stainless steel.

Both externally applied loads and residual stresses tend to impair the passive film of the stainless steel where the loads are affecting, which produce pitting corrosion. Presence of metallic inclusions with the stainless steel matrix enhances the probability of pitting corrosion due to differential deformation mechanism. (Verneau & Mecozzi, 2000) Based on the report outcomes, it is self-evident that the presence of deformation in the welded component is a manifestation of the high probability of SCC and poor localized corrosion resistance.

3.4 Distortion in welded structures

The present of distortion in a welded component is an evidence of the existence of residual stresses. Residual stresses either thermal or mechanical produce distortion when overstepping the material's yield strength. Distortion can be identified as; any deviation of the component physical geometry resulted from the welding process. Distortion is undesirable; it produces detrimental consequences; it affects the welding structure functionality, complicates the assembly in multi-parts structures, and decreases the fatigue strength and static strength in addition to their effects towards the aesthetics aspect and the associated high repair cost.

Many factors are affecting the occurrence of distortion in welding as stated by the welding institute (TWI, 2018).

- Parent material properties; coefficient of thermal expansion is the dominant property of the material controls the stresses generated during the welding process and therefore the distortion.
- Restrains; it may restrict the physical deviation or movement of the welded part. However, it produces residual stress and increases the cracking probability.
- Joint design; proper plan for distortion mitigation starts from the design phase. Edge preparation and dimensions have to be selected to distribute the induced heat equally and prevent distortion. Double-sided bevelling is recommended for thick plates.
- Welding parameters; as discussed in this chapter, distortion is firmly connected to residual stresses, which is connected to a part of the welding parameters. For instance, the heat input, it has to be optimized in order to achieve the required quality and prevents distortion simultaneously.

- Fit-up; proper fit up has to be implemented during welding to achieve the alignment. Tack welding is required occasionally to restrict the part movement.

3.5 Types of distortion in welding

Only the permanent deformation in the structure geometry that remains after completion of welding considered as welding distortion, not the transient or elastic deformation during the welding process. Commonly distortion classified based on the direction relative to weld line, longitudinal and transverse Shrinkage, where length/width reduces due to the shrinkage force. Displacement or rotation around the origin after welding is another type of welding distortion. Angular distortion is the primary type in butt-welding.

3.5.1 Angular distortion

According to Adamczuk et al., (2017, p. 305), angular distortion is the "rotation of the structure around the welding line". Temperature gradient over the thickness of the plate is the causative agent of the angular distortion. The different cooling rate at the welded plate thickness creates differential transverse shrinkage where the contraction is higher on the surface of the plate comparison to the bottom. Then, angular distortion occurs. Thicker the plate, higher the probability of angular distortion due to the huge amount of deposited material and high heat input. (Adamczuk, et al., 2017, p. 311) When restrained the angular distortion by mean of clamping or fixing during welding, component tend to deform in longitudinal bending form. Shrinkage force may lead to unstable transverse deformation such as “Buckling” notably for the thin plates. (Radaj, 1992, p. 15)

Adamczul et al., (2017) at the Federal University of Rio Grande do Sul carried a distortion experiment in order to study the effect of dimensions (length, width, and depth), heat input and number of passes on the angular distortion in constructional steel ASTM A36-butt joint. GMAW were adopted to weld the joints. LVDT (Linear Variable Differential Transformer) was utilized to measure the angular distortion correspond to each pass, the sensor has been placed away from the weld area to avoid the elevated temperature at the weld pool. The goniometer was utilized to verify the LVDT readings and measure the overall angular distortion after welding, measures taken at the center of the weld piece and at both ends with a small offset. Figure 10 shows the set-up of the measurement devices on the weld plate.

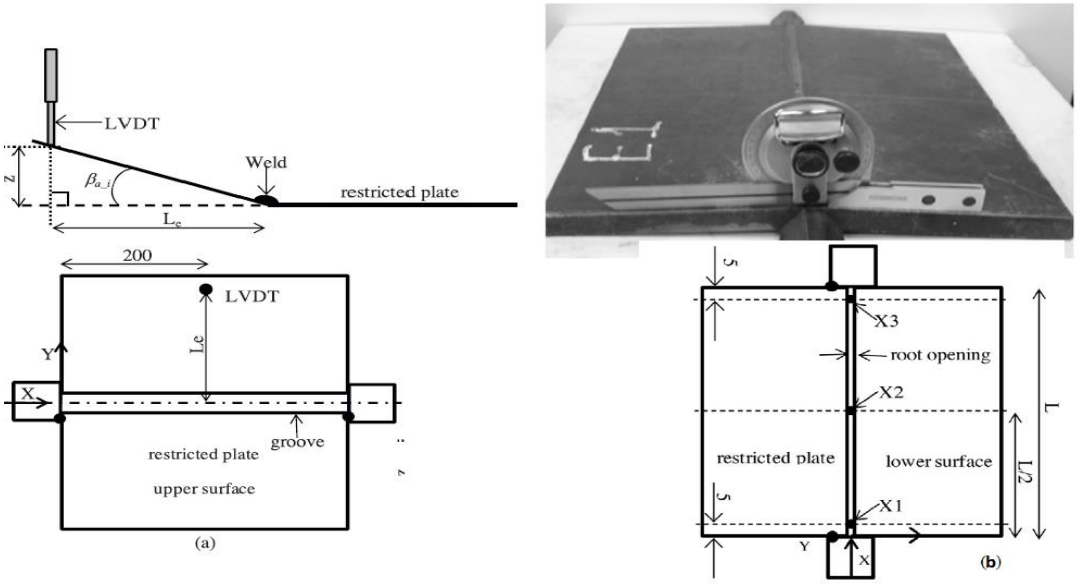

Figure 10. Angular distortion measurement devices. LVDT (a) and Goniometer (b). (Adamczuk, et al., 2017, p. 307)

The experiment results reveal that through the beginning passes, welds show slight angular distortion and the small temperature gradient through the thickness justifies this result. Then for the third, fourth and fifth pass distortion increased significantly due to high-temperature gradient and stiffness drop at the bottom of the plate. Starting from the pass number six, angular distortion decreased gradually when the thickness of the weld increase and temperature at the bottom decrease. It has been noticed that heat input and plate thickness have a minor influence on the angular distortion. (Adamczuk, et al., 2017, p. 313)

Figure 11 shows the relation between passes and the measured angular distortion (βi), while (I) represents the pass number from 1 to 13. Different heat input values were applied. It can be observed from the chart that, maximum angular distortion occurred in the fourth welding pass when heat input was 1.3 KJ/mm, and higher heat input at the same pass produced less distortion. Distortion was minimal for subsequent welding passes from sixth to 13th. The relation between heat input KJ/mm and angular distortion is not steady rather than fluctuating from one welding pass to another.

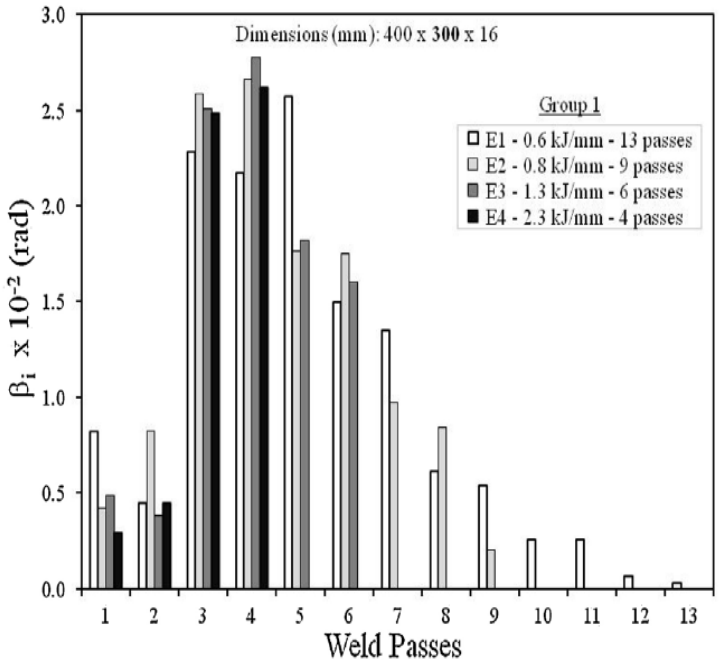

Figure 11. The relation between welding passes and angular distortion (Adamczuk, et al., 2017, p. 308).

3.5.2 Shrinkage

Shrinkage is a length reduction of the weld part geometry due to the non-uniform thermal stresses. It occurs in two directions, longitudinal or parallel to the weld axis and transverse shrinkage, which takes place perpendicular to the weld direction. Shrinkage deforms the outer dimensions of the weld part and affects functionality. For longitudinal shrinkage, 3mm is acceptable for each 3m in butt joint and 0.8mm each 3m for the fillet weld. For transverse shrinkage. (TWI, 2018)

Some equations have been derived to predict the distortion in the welded parts. The following equation predicts the longitudinal shrinkage as a function of the heat input, welding speed, and other parameters. (Verhaeghe, 1999)

$$\delta_L = \frac{0.335Q}{A\,v}\,\frac{\alpha}{\rho cp} \qquad (1)$$

Where δ_L is the longitudinal distortion, Q is the heat input, A is the cross-section area of the welded plate, ν is the welding speed, α is the coefficient of thermal expansion, ρ is density

and *cp* is the specific heat. (Verhaeghe, 1999) Figure 12 shows the different forms of distortion, which can exist on a plate because of welding stresses.

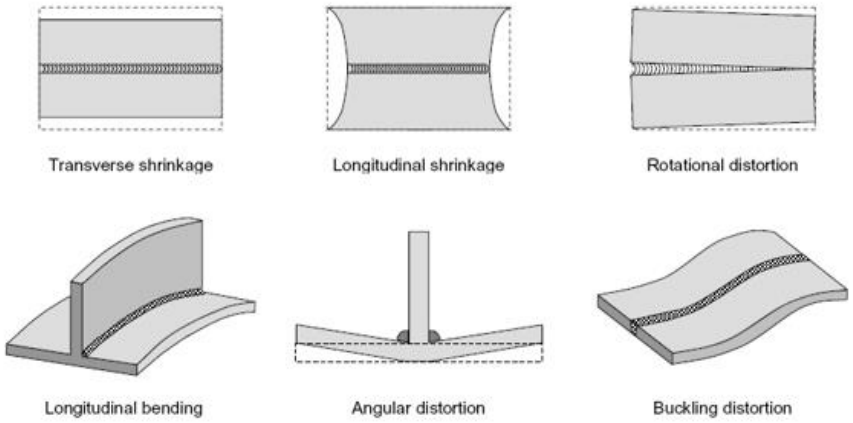

Figure 12. Different types of distortion in the butt and fillet weld (Damen, 2015)

Radaj has stated many equations for estimating different types of distortion based on the heat input, the dimension of the welded part and the thermal properties of the material. Equations 2, 3,4,5,6 and 7 below counterparts' equations (1), (3), (143), (175), (149) and (174) respectively as stated in (Radaj, 1992)

$$q = \eta_h \, UI \tag{2}$$

Where q represents the heat output from the heat source in (J/s), U is the power source volt, and I is the welding current in (A).

$$q_w = q/v \tag{3}$$

Where q_w is the heat input per unit length (J/mm), and v is the welding speed (mm/s).

$$q_w = K \, A_w \tag{4}$$

Where K is the proportionality factor varies based on the welding process; it is 41 for gas metal arc welding (GMAW). A_w is the cross-section area of the weld (mm^2)

$$\Delta L = \frac{Fs.L}{E.A} \quad (5)$$

Where ΔL is the longitudinal shrinkage result from the welding thermal stresses (mm), Fs is the shrinkage force (N), L is the weld piece length (mm), E is the elastic modulus (N/mm^2) and A is the cross-section of the plate (mm^2)

$$Fs = \mu_1 \frac{\alpha\, qw}{c\, \rho} \quad (6)$$

Where μ_1 is the stiffness factor according to the welded material, α represents the coefficient of thermal expansion (1/K), c is the specific heat capacity (J/g K), and ρ is the density of the material in g/mm^3. Equation 7 has derived from (5) and (6).

$$\Delta L = \mu_1 \frac{\alpha\, qw\, L}{c\, \rho\, A} \quad (7)$$

3.6 Distortion prediction and mitigation

Distortion in welding is a complicated thermo-mechanical problem. Many researchers have adopted numerical methods by building three dimensional (thermos-elastic-plastic) finite element model (FEM) to predict the produced residual stresses and distortion in welding. Some of these models accompanied with experiments to verify the accuracy of the numerical model.

Deng and Murakawa (2008) have used FEM to simulate the welding distortion in carbon steel sheet, butt joint with 1mm thickness. The experiment was carried out to compare the real data with the simulation one. Researchers have recognized the importance of distortion measurement in thin plates of steel due to low stiffness and wide application in the automotive industry. For the experiment, GMAW process was utilized to join two thin plates (100mm X 100mm X 1mm) with a gap of 0.4mm. Vernier gauge used to measure the distortion after welding. Figure 13 shows the schematic drawing for the measuring arrangement.

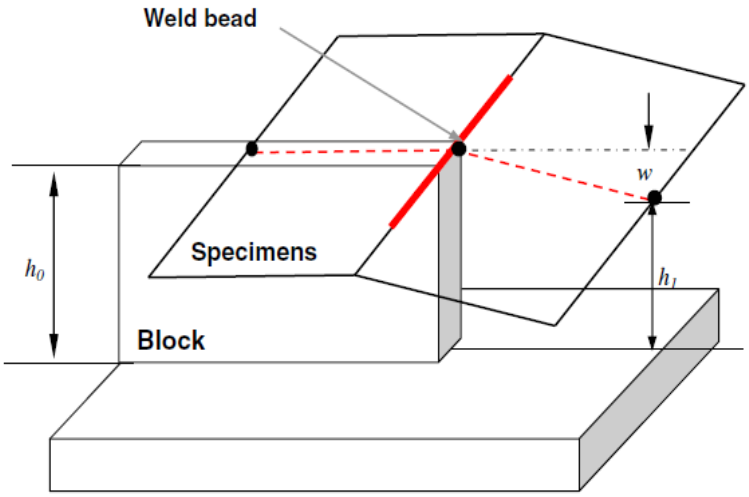

Figure 13. Measuring method of deflection in the welded sheet (Deng & Murakawa, 2008, p. 354).

Simple calculation adopted to find the deflection at the center of the welding line. The formula below shows the average value of the deflection after measures three different parts.

$$w = \frac{\Sigma(h_{\circ} - h1)}{3*2} \qquad (8)$$

Where w is the average deflection, h_0 is the original height of the plate, h1 is the height after deformation. Dimensions of the bead shape have been used as in input for the FEM, thermal data of the materials as well represented input data. FEM has proved high accuracy in predicting the distortion of the thin plate after welding. (Deng & Murakawa, 2008)

Another team of mechanical engineers in the UK and Malta tried to predict the welding distortion and develop a mitigation method by adopting three different computational simulations. Engineers have used the cryogenic CO_2 as a cooling fluid to reduce distortion. The experiment was done for butt-joint and fillet-joint, each model has been tested with and without the cryogenic fluid. Results revealed that significant reduction has achieved in distortion for the butt-joint when cooling was involved. Cooling has a minor effect on distortion in case of fillet-weld joint due to the complex configuration. (Camilleri, et al., 2010, p. 10)

Mitigation techniques of welding distortion can be categorized into two substantial forms; distortion prevention during the design phase and the other one through the fabrication phase. For design phase, distortion can be prevented by optimizing the configuration of the joint to reduce the amount of deposited material.. (Camilleri, et al., 2010) a good design for structures minimize the weld and utilize alternatives such as cold forming processes. proper placing of the welding (at the neutral structure axis) reduces distortion. Single-pass in a small cross section butt-weld minimizes angular distortion. Bevel angle and root gab have to be optimized. Selection of the appropriate welding process when deep penetration is required for minimizing deposition and distortion such as LBW and plasma welding. Reduce the number of passes and apply the welding sequence to minimize the angular distortion. Double -V joint is recommended for welding thick plates. (TWI, 2017)

Different techniques are used to prevent distortion during fabrication. Tack welding, back to back welding and stiffening are applied methods for welding distortion prevention. Tack welding is essential to keep the gap uniform along the weld, ensure proper fit-up and resist transverse distortion and it has different sequences, while back to back welding is about the introduction of an identical part of the welded one to place the weld at the neutral axis and minimize distortion. Stiffeners are effective in resisting the longitudinal shrinkage or bowing. (TWI, 2016) Figure 14 shows the tack welds applied as intermittent short weld in a butt joint. (Brown, 2018)

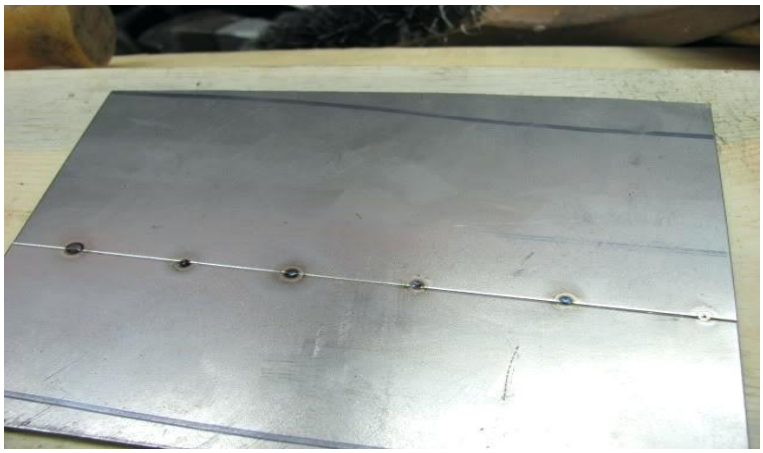

Figure 14. Tack welding in square butt-weld joint (Brown, 2018)

Figure 15 summarizes the basic techniques and procedure required to prevent distortion in welding. The chart includes the main six divisions and sub-divisions with little details for the recommended practices to mitigate distortion. Occasionally, it is not possible to follow all the mentioned procedures due to the application requirements, however, the rest of the defensive techniques are useful.

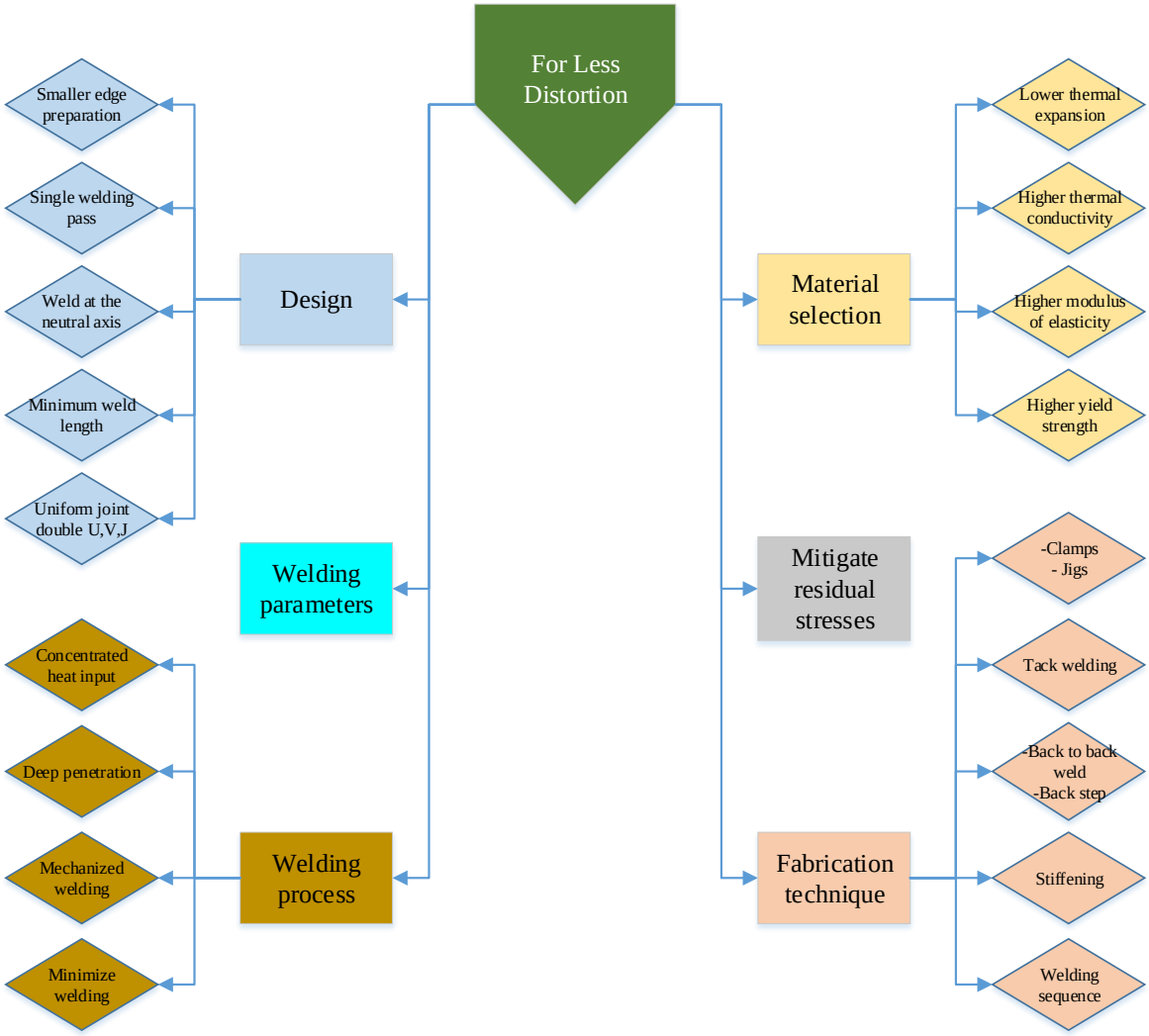

Figure 15. Welding distortion preventive techniques.

4 EXPERIMENT METHODOLOGY

For the experimental work, robotic GMAW and CW laser welding were applied to produce ten (10) square, butt-joints. Base material (BM) is low carbon- austenitic stainless steel 316L (1.4404), filler material for GMAW process is "Elga Cromamig 316L Si" with similar properties to the parent material, further details about the materials properties in section 4.2. Adopted air gap is 1.2 mm, and plates dimensions are 100*200*3mm. Shielding gas is Ar – CO_2(2%) mixture for less spatter, stable arc and to control surface oxidation (Kikani, 2016, pp. 6-9). Different heat input per unit length (KJ/mm) were applied by employing variable welding speeds.

The objective of the experimental work is to investigate the effect of the welding process and the applied heat input on the welding quality of 316L stainless steel. Distortion, hot cracking, and resistance to intergranular corrosion are the targeted quality aspects. Two welding processes were applied, robotized MAG and fiber laser welding. Laser welding is autogenous. Figure 16 shows the robot utilized for the welding experiment.

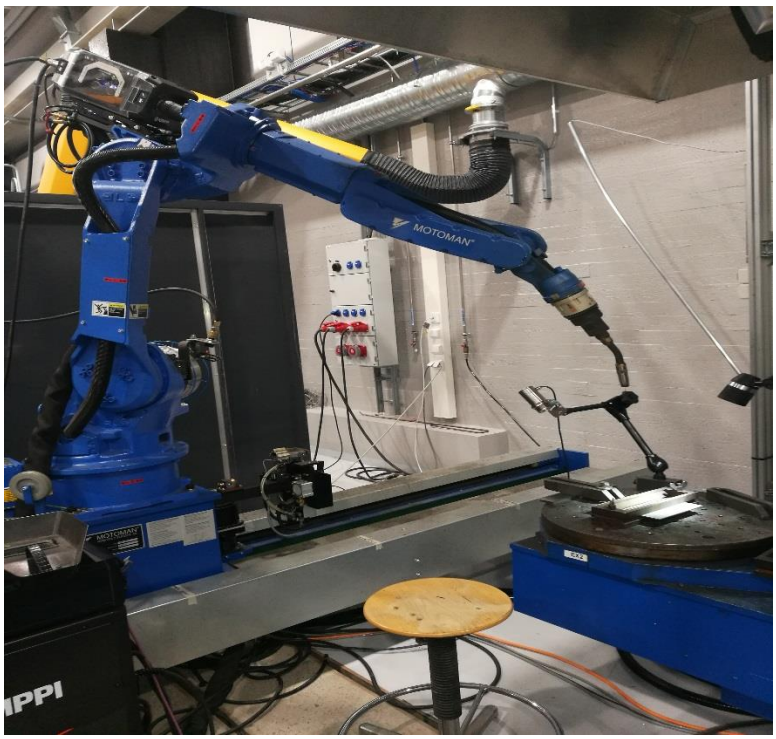

Figure 16. Welding robot used in the experiment to create the MAG welding samples.

Pyrometer temperature sensor was mounted close to the weld pieces and focused at the center of the weld seam. Sensor range is between 400°C - 1600°C, the purpose of using the sensor is to measure the cooling rate during the solidification period. Figure 16 shows the laser temperature sensor at the vicinity of the welding robot. Kemppi-A7 welding machine manufactured by Kemmpi was attached to the robot to carry out the welding.

Ten (10) samples of the base material were welded, six with robotic MAG welding, three of them with different welding speed and with partial constraints and other three with the same welding speeds, however, constraints were applied. Figure 17 shows the applied setup for the plates before welding to ensure the required fit-up mode, which was partially constrained in (A) and fully constrained in (B) The rest of the samples (4) were joined by fiber-laser welding with different heat input achieved by changing laser power and speed.

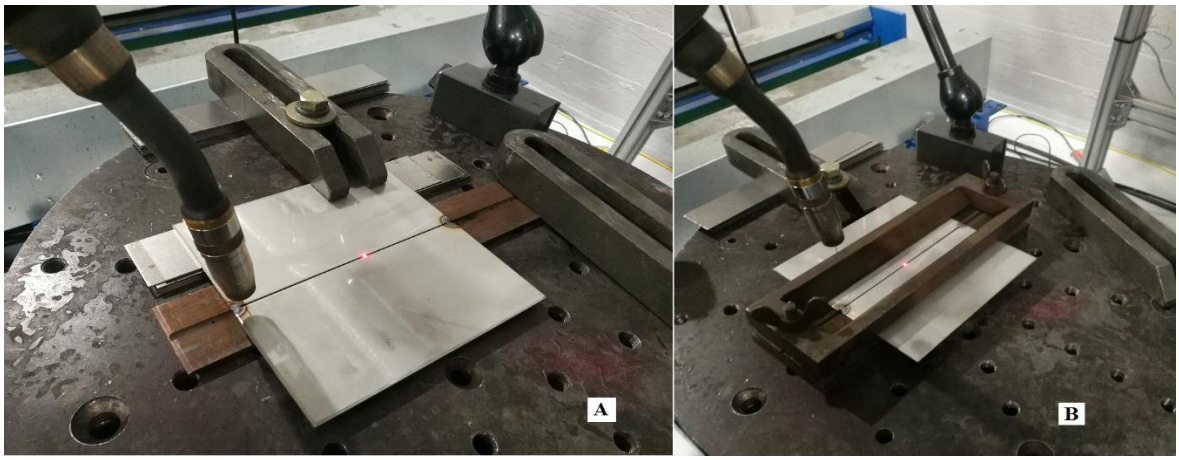

Figure 17. Welding fit- up. Partially constrained (A) and fully constrained (B).

4.1 Welding procedure specifications (WPS)

The preliminary welding procedure specification (pWPS) of the experiment was commenced based on the previous experience of the technical staff in the welding laboratory. Initial values for welding current, arc voltage, travel speed, gas flow rate and air gap were adjusted with "try and error" concept to reach the appropriate parameters.

The point of the parameters setting trials before the welding is to achieve a full penetration weld with low heat input or by other mean, optimal welding parameters. Welding current and voltage nearly remained constant for all samples, while welding speed has changed.

Tack welding was applied with TIG to ensure the uniform air-gap. The following equation has followed to calculate the heat input per unit length as per European standard (EN 1011-1)

$$Q = \frac{K.V.I}{\nu.1000} \quad (9)$$

Where Q represents the heat input per unit length (KJ/mm), K is the thermal efficiency which is 0.8 for GMAW, V is voltage (V), I represent the welding current (A) and ν is the welding speed (mm/s). Table 6 presents the welding parameters applied for the MAG samples, while the pWPS is attached in appendix IV which shows all the basic information of the robotic-MAG welding.

Table 6. Welding parameters of the MAG samples.

Sample	Filler material size Ø (mm)	Current (A)	Voltage (V)	Travel speed (mm/s)	Wire feed rate (m/min)	Heat input (KJ/mm)	Constraints
MAG-1	1.0	160	25	9.0	9.5	0.355	Partial
MAG-2	1.0	157	26.3	7.0	9.5	0.472	Partial
MAG-3	1.0	157	26.3	11.0	9.5	0.3	Partial
MAG-4	1.0	157	26.3	9.0	9.5	0.367	Full
MAG-5	1.0	155	26.4	7.0	9.5	0.467	Full
MAG-6	1.0	157	25.4	11.0	9.5	0.29	Full

The following equation was applied for heat input calculation in the laser welding process.

$$Q_L = \frac{K.P.60}{\nu.1000} \quad (10)$$

Where Q_L represents the heat input (KJ/mm), P is the laser power (kW), thermal efficiency (K) is 0.9 and ν is the laser speed (m/min). Table 7 presents the welding parameters for the laser samples, different values for the heat input were achieved by changing the laser power, speed and focal position.

Table 7. Laser welding parameters.

Sample	Power (kW)	Speed (m/min)	Focal (mm)	The heat input (KJ/mm)
Laser-1	4	3	3	0.072
Laser-2	3	2.5	3	0.065
Laser-3	2.5	2.2	3	0.061
Laser-4	2	2	0	0.054

4.2 Material properties.

This part of the research presents the chemical composition and the fundamental mechanical properties of both, the base material and filler material. Parent material is austenitic stainless steel with low carbon percentage 316L and the filler material applied in MAG welding is Elga Cromamig 316L Si matching to the parent material.

The chemical composition of the tested material is given in table 8, which shows the alloying elements as percentages of the total weight (% wt). The material inspection certificate is attached in Appendix I.

Table 8. Materials composition.

Material	C %	Si %	Mn %	P %	S %	Cr %	Ni %	Mo %	N %
Base	0,018	0,45	0,98	0,038	0,001	17,1	10,0	2,04	0,036
Filler	0,015	0,80	1,70	0,015	0,01	18,0	12,0	2,60	0,06

Table 9 shows the mechanical properties of the material. Yield strength, tensile strength, elongation, and hardness are covered. The values of the mechanical properties were taken from the material certificate provided by the supplier (Appendix I).

Table 9. Mechanical properties.

Material	Yield strength Rp 0.2%-MPa	Tensile strength Rm - MPa	Elongation A5	Hardness HBW
Base	317	603	56%	182
Filler	350	520	30%	-

4.3 Weld tests

To answer the research questions, different tests were designed. Tests reveal the magnitude of longitudinal and angular distortion produced in the welding samples as a result of the welding heat and filler material deposition. In addition to the microstructure and carbides formation investigations. This part of the research discusses the accomplished tests.

4.3.1 Angular distortion

Angular distortion is a common phenomenon in welding of the austenitic stainless steels. Therefore, it controls the weldability of the material. A sensitive laser-2D device was utilized to measure the angular distortion on the welded pieces.

Measuring device (laser 2D) were calibrated before the experiment to set the two dimensions (Height in Y direction-Length in the X direction) initial values. The measuring device is so sensitive, where it hits hundreds of height (Y) readings in one single location. Angular distortion values were measured at three (3) positions on each weld sample, both ends, in addition to the center of the plate named as T1, T2 & T3 as shown in figure 18. Readings were obtained by moving the laser beam source manually through the fixed beam to pass along T1, T2 & T3 lines.

Figure 18 shows the laser-2D device utilized in measuring the longitudinal distortion and the angular distortion, the entire system is located at the center of the figure, while the laser sensor was enlarged on the left side and the welded plates on the right side of the figure. Lineation (Ti, T2, T3, L1&L2), welding direction and measuring directions were illustrated on the plate.

The measuring system consists of laser source attached to a bi-dimensional track. When laser source moves along the track over the tested plate, height reading from reference point to the surface of the plate and displacement in X-direction are being registered. The measuring device is associated with a software to collect the data from the laser sensor; the software draws a mirror image for the plate on the direction of the measurement, the data from the software can be transferred and treated by another program such as Microsoft Excel for further analysis.

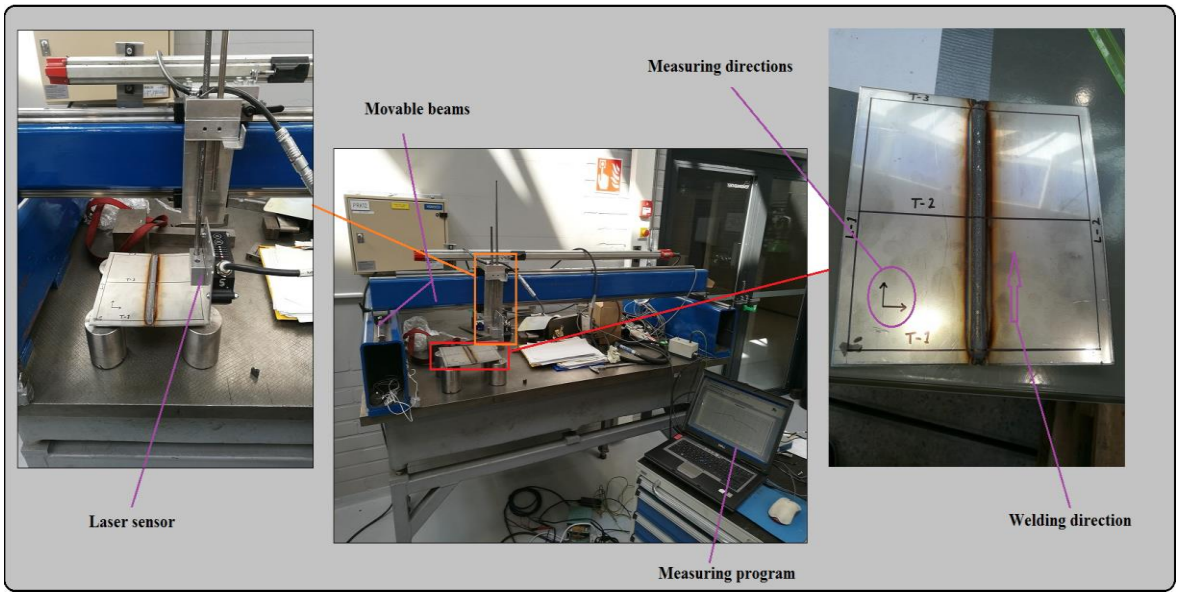

Figure 18. The laser-2D device, utilized for measuring distortion.

The data from the laser -2D device software obtained in notepad file format, then transferred to excel files and then, a mirror image of the plate profile at T1, T2 & T3 have been drawn. Therefore, the angular distortion calculations were done based on the following equation.

$$Ø = Tan^{-1}\ Y/X \qquad (11)$$

Where Ø is the angular distortion in (Degree), Y is the height or vertical displacement at the end of the measurement line, deviated from the original location (0) before welding in mm. X is the transverse displacement from the weld center to the end of the line (TI, T2 or T3) in mm. Distortion angle was measured on both ends.

4.3.2 Longitudinal distortion (Bowing)

Longitudinal distortion, bowing or longitudinal bending can be defined as the curvature produced in the longitudinal direction of the welded plate as a result of the welding process. Bowing occures either in the lower direction of the plate (smiley face) or the upper direction (sad face). Bending is a significant concern in welded structures; it affects the assembly, performance, and weldability in general.

Same device and mechanism applied for measuring angular distortion were adopted for longitudinal distortion. L1 and L2 lines appear in figure 18 were utilized to measure the

bending on both sides of the plate. Maximum height deviation from the original position of the plate (straight) represents the magnitude of the longitudinal distortion. The numerical value of X in the schematic drawing of the welded plate (figure 19) represents the longitudinal distortion measured in millimeter. As can be seen, the maximum value of distortion or bending can be found at the center of the plate or at any other position along the length of the plate.

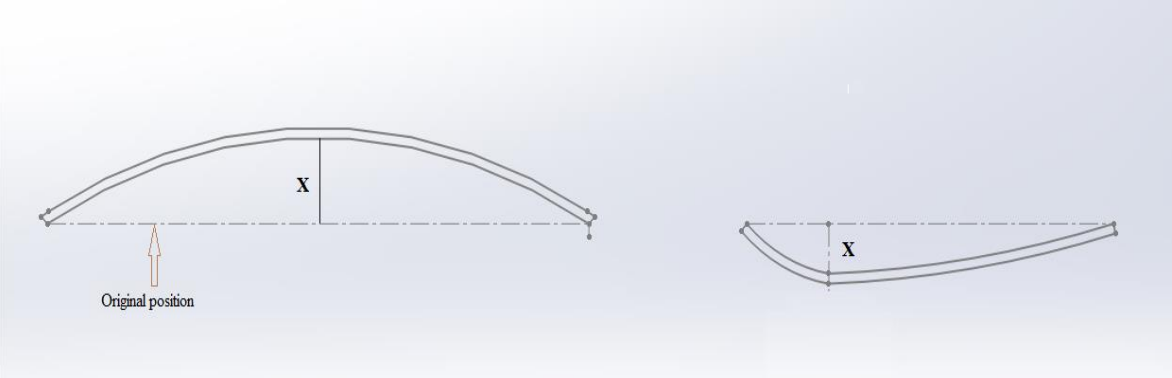

Figure 19. Longitudinal distortion measurement.

4.3.3 Samples preparation and Macro examination

After distortion analysis, samples were sent to the shearing machine. Small pieces were cut out of the original plates for macro examination and microstructure analysis. The following steps were followed to prepare metallographic samples.

1. Dry grinding.
2. Wet grinding. Through two roughness levels, 200 and 9 microns respectively.
3. Polishing. Up to 3 microns roughness.
4. Etching. 10% Oxalic acid diluted in water in presence of an electrolyte.
5. Dipping the samples in water-alcohol solution.

All samples were examined in the microscope, then macroscopic images that cover fusion area, HAZ and base metals were saved for further investigations. Figure 20 shows the consecutive processes of sample preparation starting from the prepared samples for microscopic investigation (A), dry grinding machine (B), wet grinding and polishing (C) which done through three steps at the same machine in order to reach the required surface roughness, etching process (D), the produced smooth surface after grinding and polishing is presented in (E), and finally the macroscopic examination device (F).

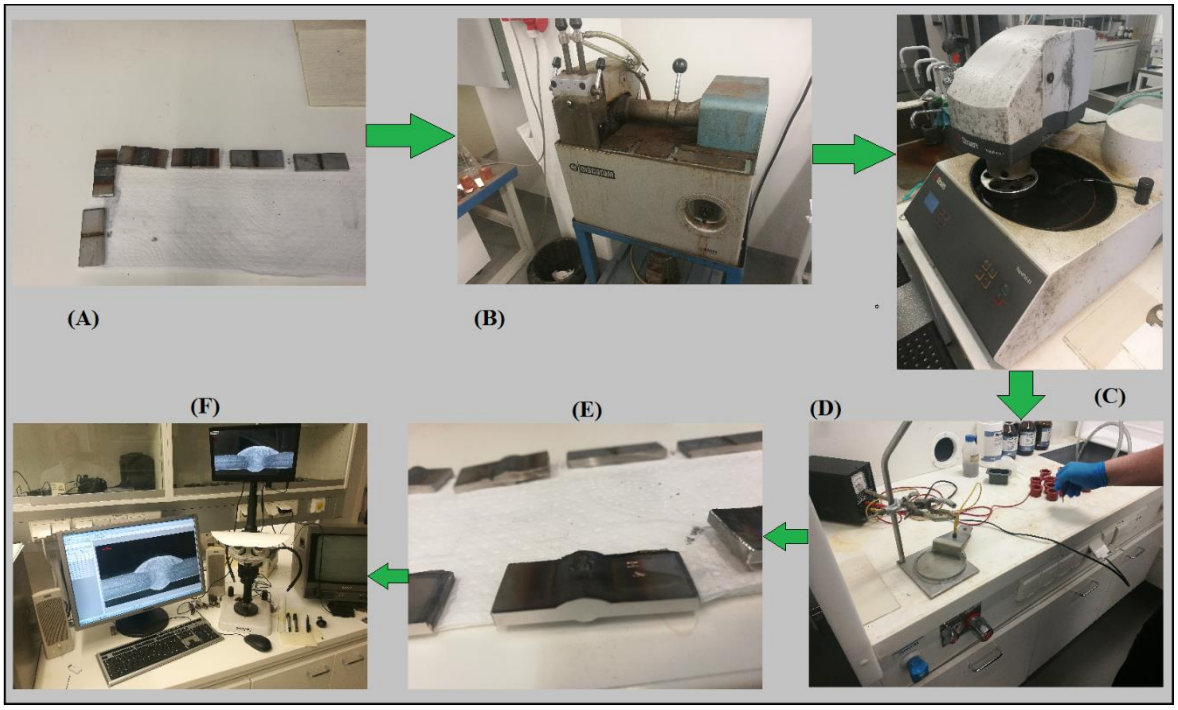

Figure 20. Samples preparation for micrography.

4.3.4 Optical microscope image

The point of applying the optical microscopic examination as part of the research is to check the phase transformation which may take place due to the applied heat. Carbides formation was targeted as well through the microstructure investigation. Carbides formation that associated to welding is common phenomena in austenitic stainless steels, where part of the alloying elements such as chromium and molybdenum tend to connect with carbon at specific temperatures, then accumulates at the grain boundaries. Carbides formation enhances intergranular corrosion known as sensitization phenomenon discussed earlier in the welding challenges of austenitic stainless steel (1.6).

Optical microscope with different magnifications was utilized to reveal the microstructure of the welded samples. Images for the fusion line and weld center were taken for each sample. Figure 21 shows the utilized microscope for the experiment. The utilized microscope can clearly reveal the different welding regions, such as the fusion zone, the fusion line, and HAZ. Moreover, it shows the manner in which the grains have grown and the orientation. Nevertheless, the identification of the microstructure-phases requires an advanced microscope with higher magnification and resolution.

Figure 21. Optical microscope used to reveal the microstructure of the welded samples.

4.3.5 Scanning Electron Microscope (SEM) and Electron Dispersive Spectrometer (EDS)

In the pursuit of the microstructure investigation and carbides formation, SEM and EDS tests were applied. The essential goal of SEM-EDS is to study the effect of welding heat on the corrosion resistance of 316L stainless steel and in particular the intergranular corrosion produced from carbides formation at grain boundaries. While the heat input for the first three samples (MAG 1,2&3) was almost similar to the rest of the MAG samples (4,5&6) however, fixation was the difference. Therefore, not all the samples have tested in SEM-EDS.

MAG-2, MAG-3 samples in addition to one laser welded sample (L-3) were tested in SEM. MAG-2 and MAG-3 samples where welding speed was 7 and 11 mm/s respectively were scanned with EDS. SEM investigation followed by EDS mapping scan revealed significant results of carbides formation on the grain boundaries discussed broader with images in the results and discussion part of the research.

Samples taken from the microscopic examinations were prepared in an additional surface-cleaning process in order to fit out for the SEM/EDS inspection. Figure 22 shows the sample preparation for SEM test. In the beginning, samples have to be dipped in acetone solution (A) to remove the accumlated carbon layer from the sample's surface and enhance the quality of the images, then the liquid removed with a CO_2- skimming gun (B) to reach a totally dry surface. Finally, samples placed inside the SEM device (C) and microstructure checked with different magnifications.

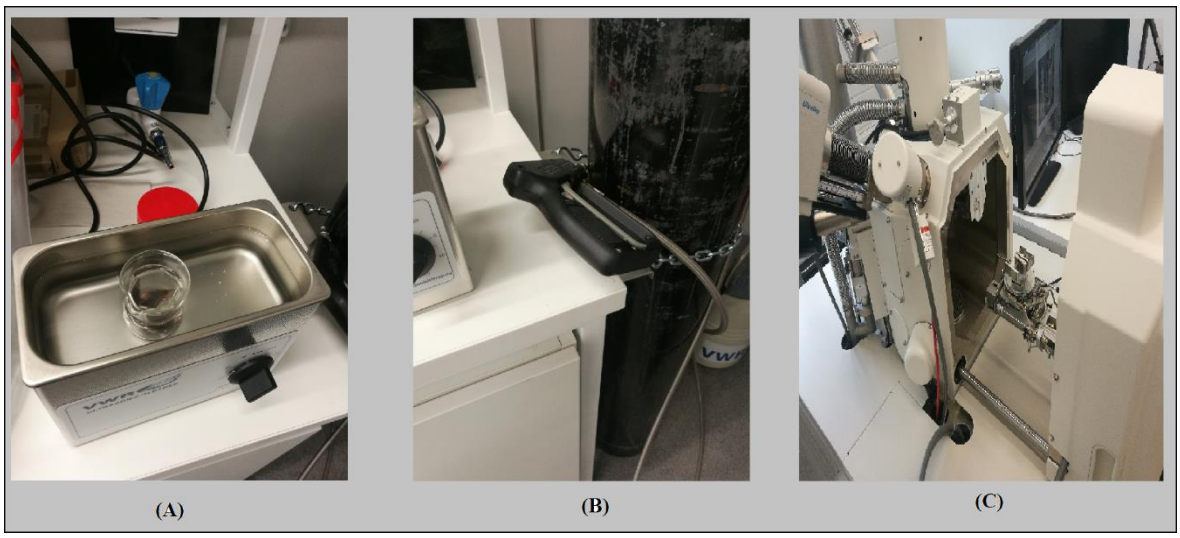

Figure 22. Samples preparation for SEM and EDS test.

5 RESULTS AND ANALYSIS

This section of the research discusses the visual inspection of the welded samples as can be seen from the macro-section images. The quality evaluation has done based on the European standard EN ISO 5817 (Welding — Fusion-welded joints in steel, nickel, titanium and their alloys (beam welding excluded) — Quality levels for imperfections). Furthermore, distortion measurements and heat input calculation for all welding samples are presented. It covers as well the microstructure analysis based on the obtained images by optical microscope and SEM in addition to EDS scan.

Based on the obtained results, graphs showing the relation between the welding speed, heat input and distortion have been created. Part of the distortion and microstructure images have been utilized for writing the result and analysis, while the rest of the deformation drawings (at the plate centers and the end of the plates) have been attached to the research as annexes. (Appendix II and III)

5.1 Visual inspection and quality assessment.

Macro-section images analyzed based on [EN ISO 5817- (2014)] was the reference for the quality evaluation of the weld samples. Analysis revealed the following.

- No cracks have been seen.
- Penetration was accepted for all MAG samples, while there was lack of penetration (LOP) 0.44 mm from the plate surface for the laser samples 1 and 2 where welding speed was 3 m/min and 2.5 m/min respectively. This value is less than 20% of the plate thickness. It is permitted only by quality level-D. Figure 23 shows the lack of penetration on the macro-section images. (Refer to table 7 for laser welding parameters)
- Fusion was accepted, and fusion lines significantly are seen.
- No porosity.
- No undercuts.
- Excess root penetration has been observed for the samples MAG-1,2 & 5 where the welding speed is 9 and 7 mm/s. It is found to be not permitted for quality level-B.

However, it is permitted as per C and D levels. Figure 23 shows the mentioned failure. (refer to table 6 for the welding parameters).

- A minimum level of spatter has been observed for both MAG and laser welding. As per the standard, the acceptance of the spatter depends on the nature of the application.
- Alignment was accepted as per the standard.
- Weld reinforcement angle was accepted for quality levels C and D (Ø > 110°) while quality level B requires (Ø > 150°)
- The geometry of the MAG weld samples was significantly deformed. Angular distortion and bending can be seen visually even before the sensitive laser -2D measurement. Figure 24 shows the deformation of the MAG welded samples.

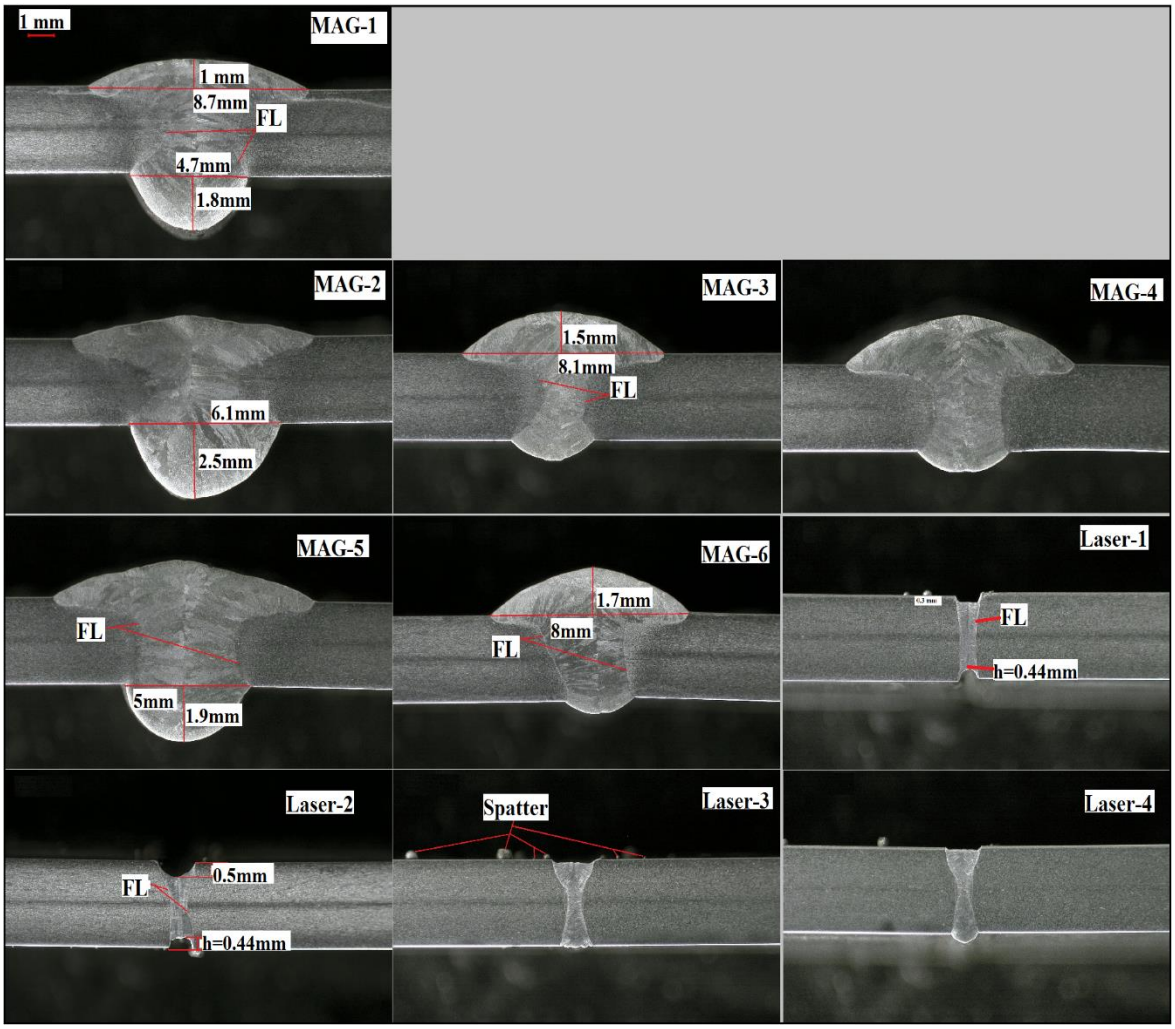

Figure 23. Optical micrograph for MAG and laser weld samples. Images reveal LOP for laser-1 and laser- 2 and excess penetration in MAG 1, MAG-2 and MAG-5.

Figure 24 shows the MAG weld samples where the angular distortion can be seen visually especially for the samples 1,2,3, and 5. The direction of the angular distortion in sample 4 and 5 where constraints were applied is opposite to sample 1 and 2.

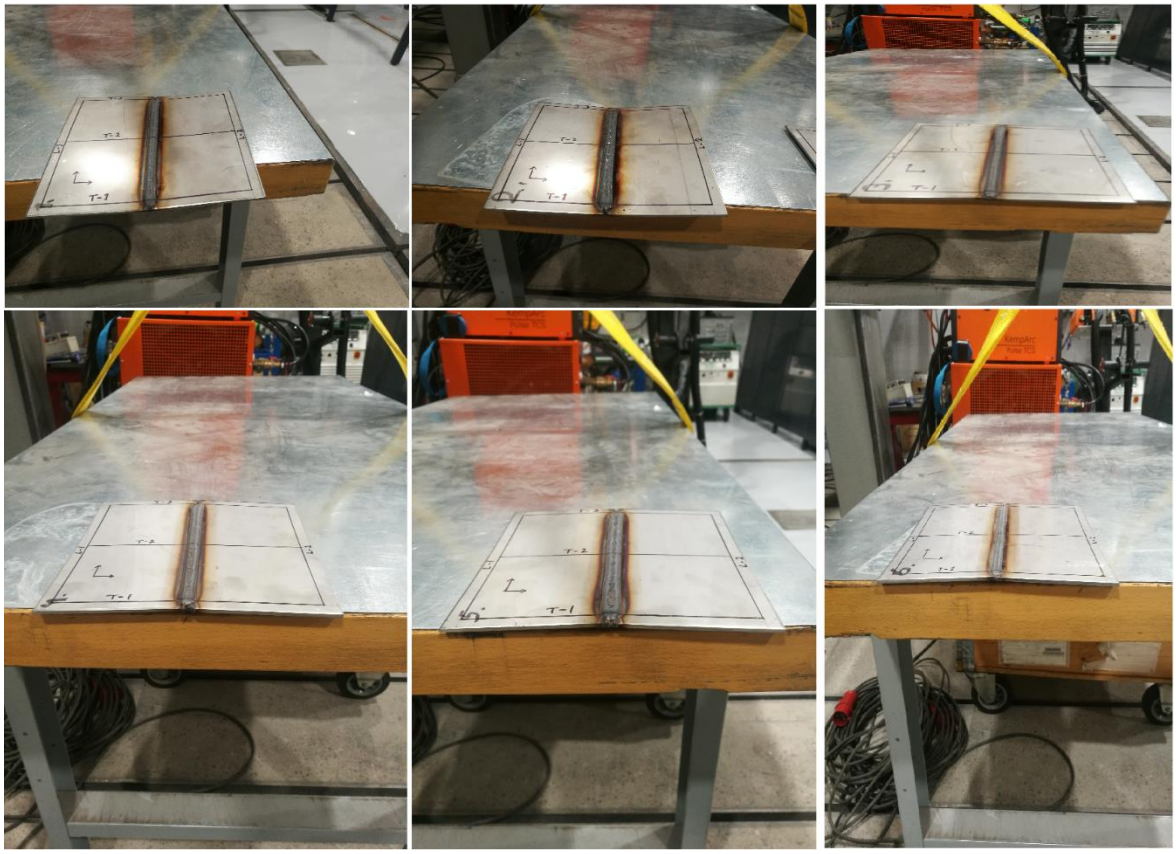

Figure 24. Angular distortion on the MAG welded samples.

5.2 Angular distortion measurements

As discussed in 4.3.1, a highly sensitive laser -2D device were utilized to measure the angular distortion (figure 18). This part of the research presents the drawn profiles of the welded plates in order to show the produced angular distortion and their measurement in the excel file. The figures covers the angular distortion measured at the front of the welded plates T1 line, while deformation at the center of the plate (T-2) and at the end of the plate where weld has finished (T-3) were attached in Appendix II and III respectively, welding speed and distortion angle equation can be seen within the figure. Figure 25 shows the measured angle of distortion and cross-section profile of the GMAW weld samples.

It can be extrapolated from the distortion sketches that, angular distortion has increased slightly when the welding speed reduced from 9 to 7 mm/s (figure 25). When the welding

speed increased to 11 mm/s, angular distortion was significantly minimized to less than 1° at both sides of the plate. A little higher speed can represent the optimum welding speed for 3mm plate - 316L steel and butt joint. Furthermore, figure 25 showing that when welding speed is 11 mm/s the plate has distorted towards the opposite direction in comparison to the lower speeds.

It can be noticed as well from figure 25 that, constraints do not mitigate the angular deformation on the 316L plate. However, the direction of the angular distortion has reversed and the magnitude of distortion angle decreased slightly

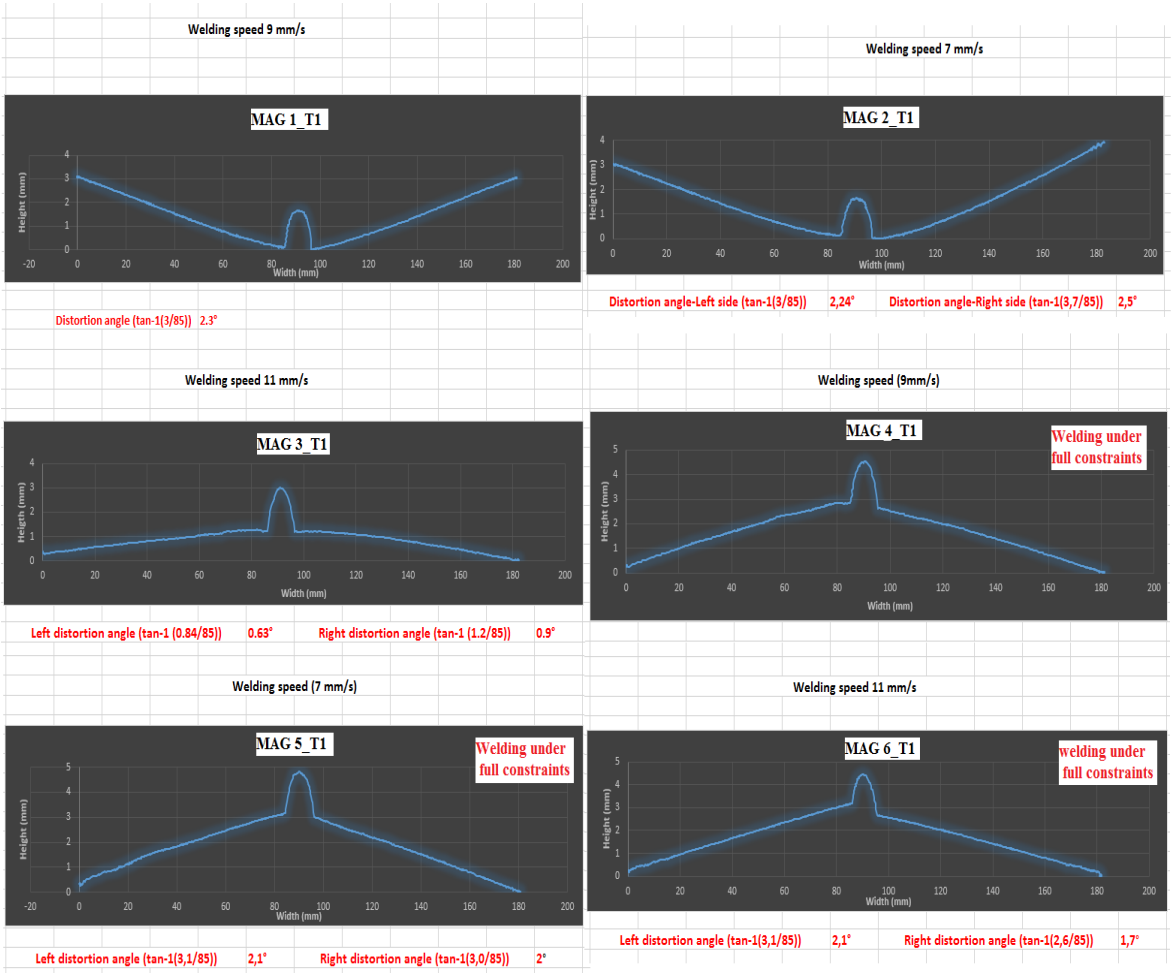

Figure 25. Angular distortion in MAG welded samples.

Figure 26 shows the distortion of the laser-welded samples. The welding parameters can be seen in the same figure. It is evident that angular distortion is relatively much less when compared to MAG welding.

Laser welding parameters applied to the sample (laser-1) have produced an optimum distortion results, a little angular distortion has been observed. Though the full penetration has not been achieved as discussed in 5.1- visual inspection and clarified in figure 23. In laser-2 sample when the laser speed lowered to 2.5 m/min, angular distortion has increased slightly, and penetration has not been achieved as in the previous sample (laser-1).

Laser parameters applied in the sample (laser-3) have produced a high-quality weld in term of angular distortion and penetration as well. Though the existence of the small amount of spatter (figure 23) which has been improved in laser-4 where the focal point has changed from 3mm to 0. It can be observed that laser-3 sample showed a better distortion compared to laser-2. However, the welding speed was less. This can be explicated due to the lower laser power in laser-3. Extrapolation of figure 26 can be outlined as; laser parameters applied in laser-3 after modifying the focal point to be on the surface of the plate (0 mm) produces a sound weld of 316L material, 3mm thickness for butt joint.

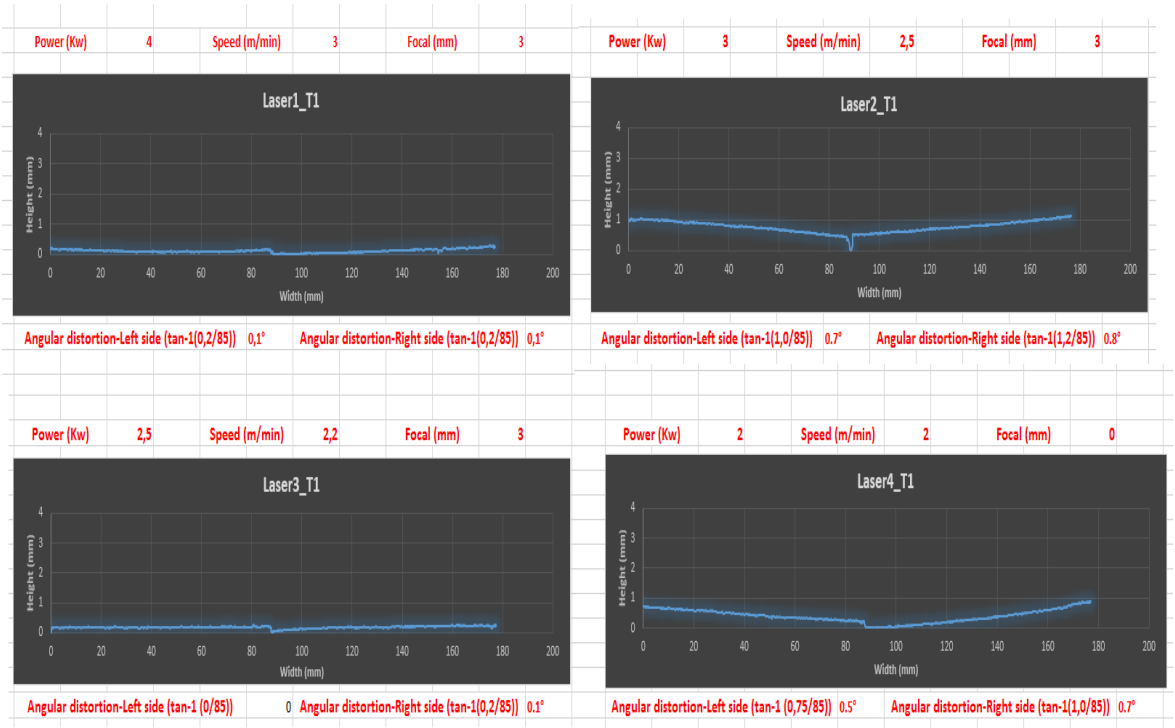

Figure 26. Angular distortion for laser welding samples.

Table 10 presents the distortion angle at the front of the plate (T1), at the middle (T2) and at the end (T3) for all weld samples measured in degree. The variation in distortion angle at

different locations (T1, T2 &T3) along the welded plate indicates the presence of longitudinal distortion or bowing. Table 10 highlights the maximum value of angular distortion which is 3.0° measured on the sample MAG2, while the least value was 0 in laser1 and laser 3 samples.

Table 10. Distortion angle

Sample	Angle (degree) T1		Angle (degree) T2		Angle (degree) T3		Maximun Angle of distortion
	Left	Right	Left	Right	Left	Right	
MAG-1	2.3	2.3	2.45	1.57	2.5	2.1	2.5
MAG-2	2.24	2.5	1.7	2.5	3.0	2.96	3.0
MAG-3	0.63	0.9	0.33	1.5	1.0	1.24	1.5
MAG-4	1.9	1.7	1.7	1.6	2.2	2.4	2.4
MAG-5	2.1	2.0	1.5	1.8	2.0	2.1	2.1
MAG-6	2.1	1.7	1.7	1.3	2.3	2.2	2.3
Laser-1	0.1	0.1	0	0.4	0.2	0.2	0.4
Laser-2	0.7	0.8	0.7	0.8	0.5	0.6	0.8
Laser-3	0	0.1	0	0.4	0.3	0.3	0.4
Laser-4	0.5	0.7	0.3	0.7	0.5	0.6	0.7

Figure 27 shows the relation between the welding speed, heat input and the produced angular distortion for the MAG weld samples. Figure 27 reveals that welding speed and angular distortion are reversely proportional to each other for the free ends joint. While for the constrained plates, distortion increases slightly when welding speed raised up to a certain limit then remains constant and independent from the speed. With regard to the heat input into the weld seam, angular distortion is always greater with a higher amount of heat input when no constraints are applied. However, for the constrained plates, angular distortion begins to increase with the higher heat input per unit length then decreases after a certain limit.

It can be seen from figure 27 that, applying the mechanical clamps to fix the welded plates prior to the welding process does not prevent the occurrence of distortion. However, the magnitude of angular distortion is different with the full constrained joints.

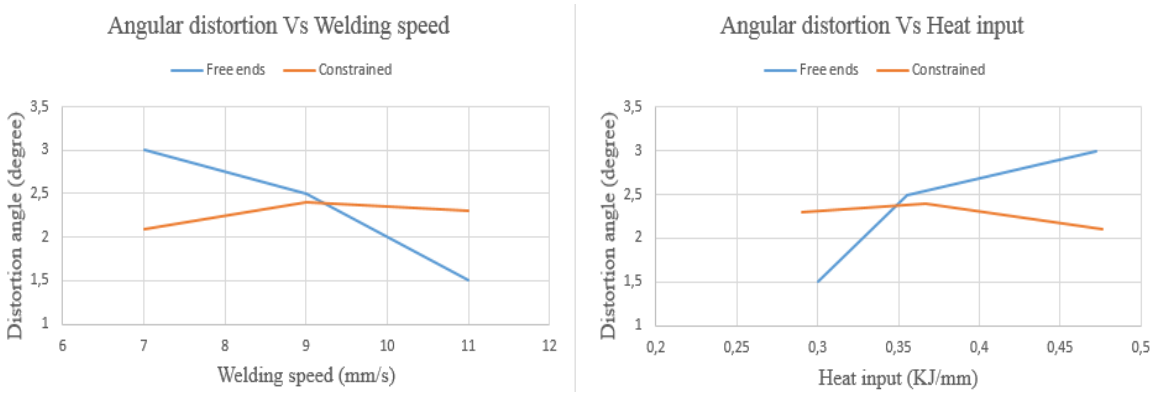

Figure 27. The relation between angular distortion, welding speed, and heat input.

5.3 Longitudinal distortion/bowing measurements

The methodology of measuring the longitudinal distortion was discussed in 4.3.2, the following graphs (figure 28 and 29) shows the drawn longitudinal distortion utilizing the obtained data from the laser -2D device. Graphs show the measured value of distortion likewise. The figures below represent the measured distortion at both sides of the plate. Left side (L1) in figure 28 and right side (L2) in figure 29.

Figure 28 reveals that. 316L tends to distort or bend longitudinally when welded with MAG while it keeps the original geometry when joined with laser welding. For free-ends joints, longitudinal distortion increases when welding speed decrease. For free-ends samples, the lowest value of angular distortion has happened at 11 mm/s where the direction of bending is reverse. MAG-3 sample where the welding speed was relatively high (11mm/s) showed a better resistance to longitudinal distortion when welded with the partially constrained situation compared to the same speed when the constraints were fully applied in MAG-6 sample.

Laser -1 and laser-3 samples have not been distorted as a result of the welding process. While laser-1 has a penetration failure, laser-3 considered as optimum parameters to joint 3 mm thick plate of 316L. Constraints have failed to restrict the longitudinal distortion rather it reverses the direction of bending. Welding speed has minimal effects on the magnitude of distortion when the joint is constrained.

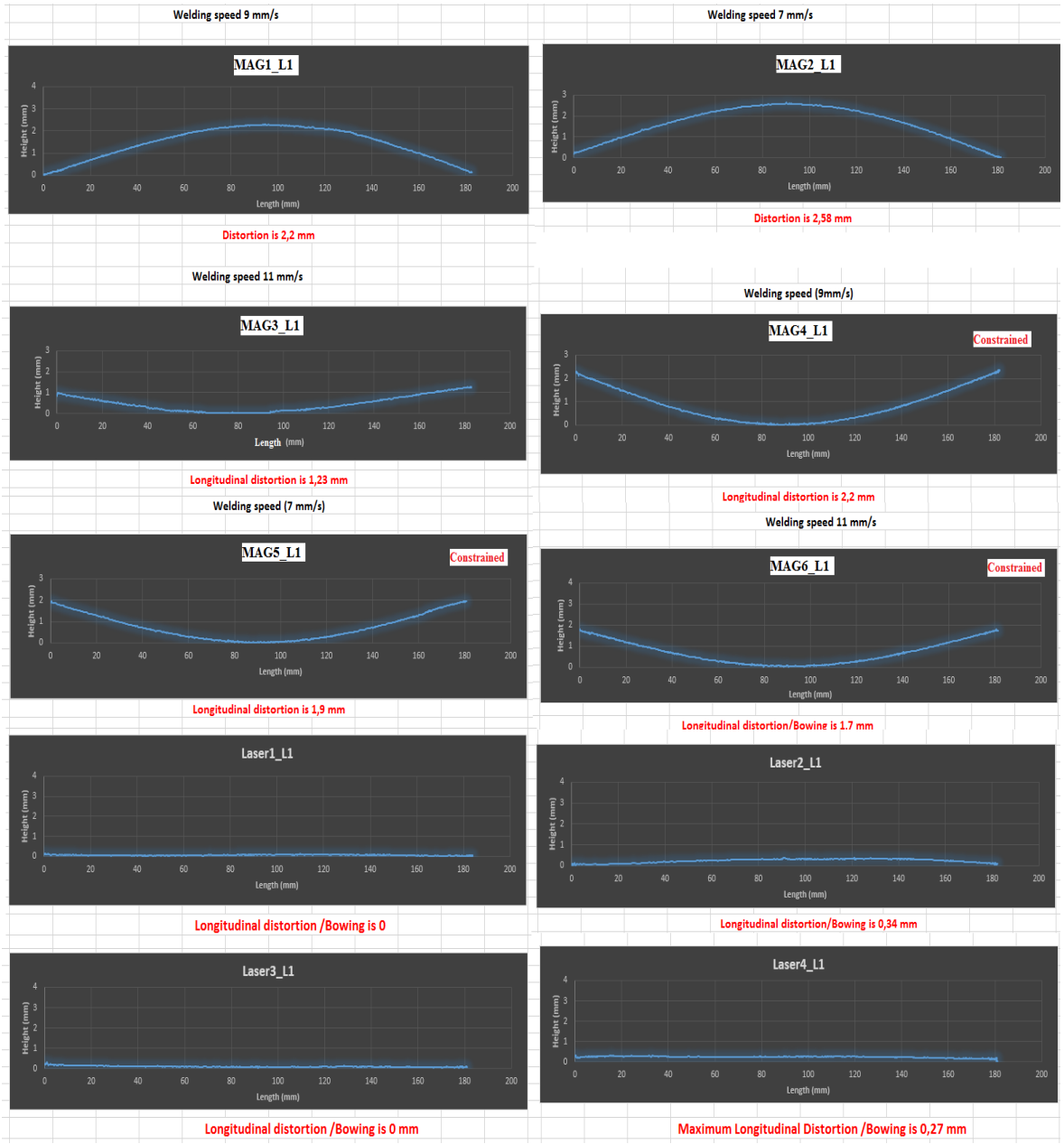

Figure 28. Longitudinal distortion for weld samples (MAG & Laser) on the left side of the plate (L-1).

In figure 29, longitudinal distortion has increased with the reduction of the welding speed from 0.95 mm at speed of 11 mm/s to 3.6 mm when the speed was 7 mm/s. Applying constraints is not an optimum solution to control the longitudinal distortion. Constrained plates showed a distortion in reverse direction (smiley face). Laser welded samples produced little distortion in comparison to MAG welding. Laser-3 parameters are ideal for zero distortion and sound weld.

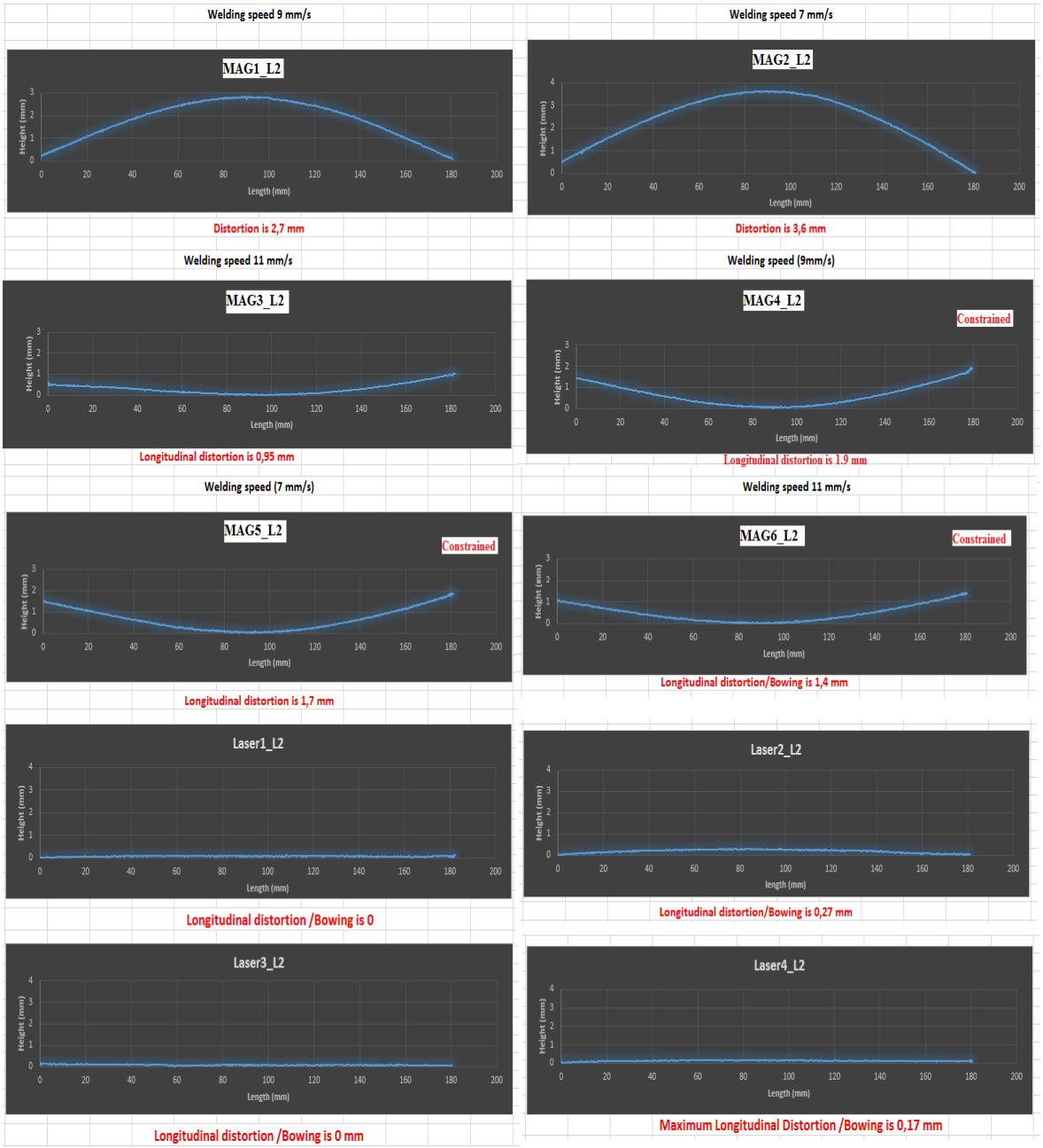

Figure 29. Longitudinal distortion for weld samples (MAG & Laser) on the right side of the plate (L-2).

Table 11 presents the values of the welding speed, heat input, and corresponding longitudinal distortion. Extrapolating from the table reveals that constraints do not restrict the longitudinal distortion however it mitigates the magnitude except for the high welding speed 11 mm/s where the free joint was distorted in a lower manner.

Table 11. Longitudinal distortion

Sample	Welding speed mm/s	Heat input KJ/mm	Longitudinal distortion-Left side-L1 (mm)	Longitudinal distortion-Right side–L2 (mm)	Max. Distortion (mm)
MAG-1	9	0.355	2.2	2.7	**2.7**
MAG-2	7	0.472	2.58	3.6	**3.6**
MAG-3	11	0.300	1.23	0.95	**1.23**
MAG-4	9*	0.367	2.2	1.9	**2.2**
MAG-5	7*	0.467	1.9	1.7	**1.9**
MAG-6	11*	0.290	1.7	1.4	**1.7**
Laser-1	50	0.072	0	0	**0**
Laser-2	41	0.065	0.34	0.27	**0.34**
Laser-3	36	0.061	0	0	**0**
Laser-4	33	0.054	0.27	0.17	**0.27**

*Full constraints were applied.

Figure 30 shows the relation between the welding speed, heat input and the produced longitudinal distortion for the MAG weld samples.

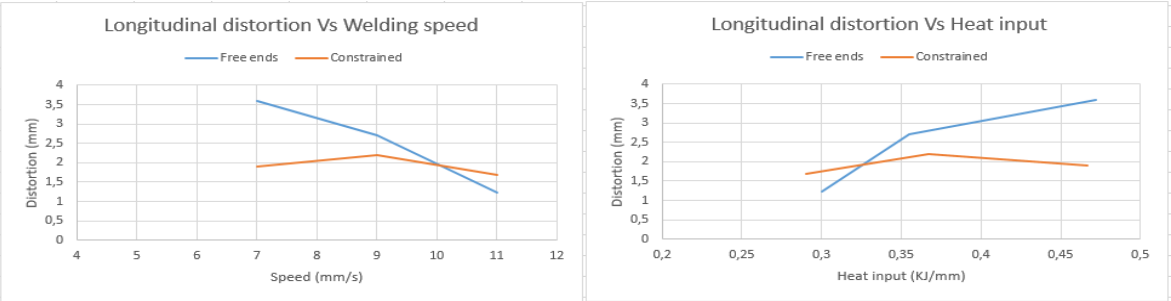

Figure 30. The relation between longitudinal distortion, welding speed, and heat input.

5.4 Microstructure analysis and hot cracking

In 4.3.4, the purpose of taking the microscopic images has been discussed. As a gateway to present the microstructure images obtained from the optical microscope, this chapter discusses Schaeffler-diagram which represents a tool to predict the ferrite level in austenitic stainless steel.

The presence of ferrite phase is advantageous to mitigate hot cracking in austenitic stainless steel, while 100%-austenite microstructure is more sensitive to fissuring at elevated

temperature. Ferrite phase prevents the segregation of low-melting elements such as phosphorus and sulphur, therefore, reduces the probability of hot-cracks. On the other hand, the high level of delta-ferrite phase reduces the corrosion resistivity of austenitic stainless steel (Kozuh, et al., 2009, p. 257).

Ferrite constitution as a percentage of welded austenitic stainless steel can either be measured utilizing special devices such as Feritoscope or predicted by employing Schaeffler-diagram for the MAG welding samples. Figure 31 represents filler metal and base metal position on Schaeffler-diagram based on calculated Cr_{eq} and Ni_{eq}. [Cr_{eq} and Ni_{eq} have been calculated based on the chemical composition in table 7 of appendix I.

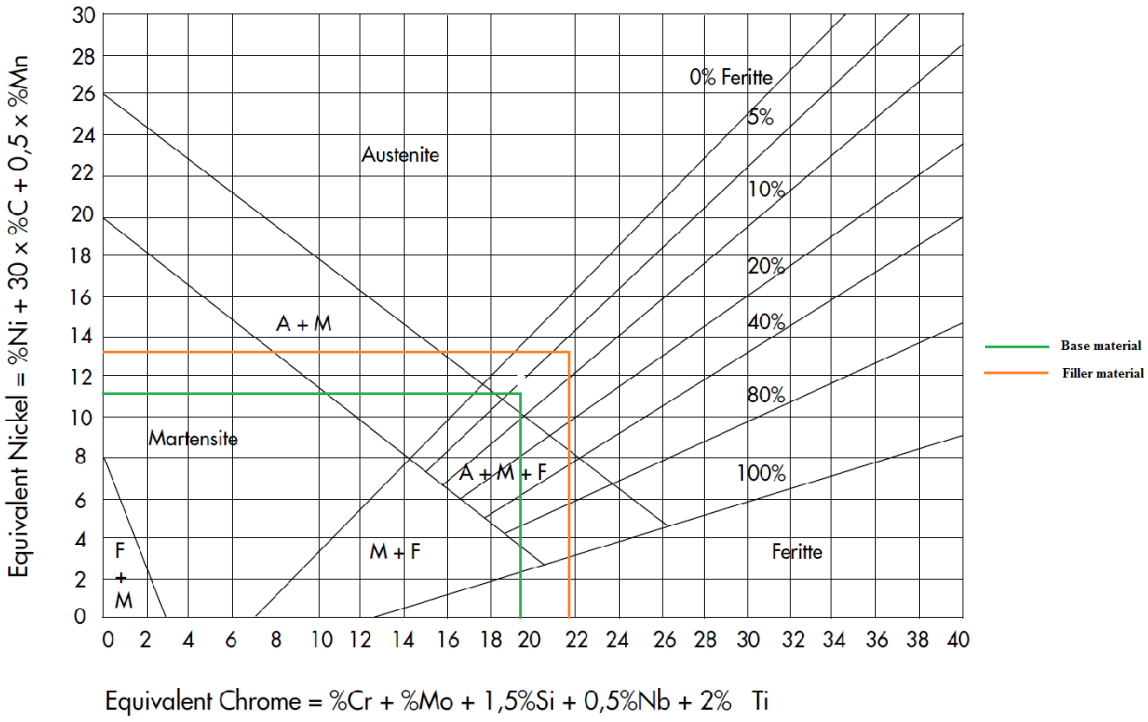

Figure 31. Schaeffler-diagram for 316L and filler material (Elga cromamig 316L Si).

Several facts can be read from figure 31. Firstly, the weld joint is heterogeneous due to the higher composition of the filler material. Solidification mode is austenite-ferrite (AF), mainly the austenite phase then a considerable amount of ferrite, it can be FA at some locations. Considering the dilution of 50%, Cr_{eq}/ Ni_{eq} is 1.7 which indicates the presence of δ-Ferrite phase (Shankar, et al., 2003, p. 561). Four solidification modes are prevailing in

austenitic stainless steel. Figure 32 list those modes attached by schematic drawing for the nucleation of each mode.

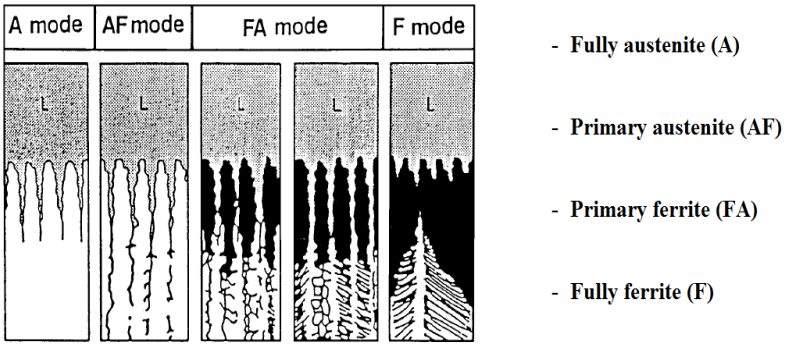

Figure 32. Solidification modes of austenitic stainless steel (Shankar, et al., 2003, p. 362).

FA and F solidification modes tend to transfer to austenite structure at room-temperature, while some of the austenitic stainless steel groups such as 304 and 316 permanently found in the austenite phase at room-temperature (Shankar, et al., 2003, pp. 362-362). Figure 33 represents the ternary diagram FE-Cr-Ni clarifies the formed phases out of liquid phase in stainless steel materials, the figure also shows a binary diagram derived from ternary one when the iron content is 70% corresponding to the utilized material for this research 316L.

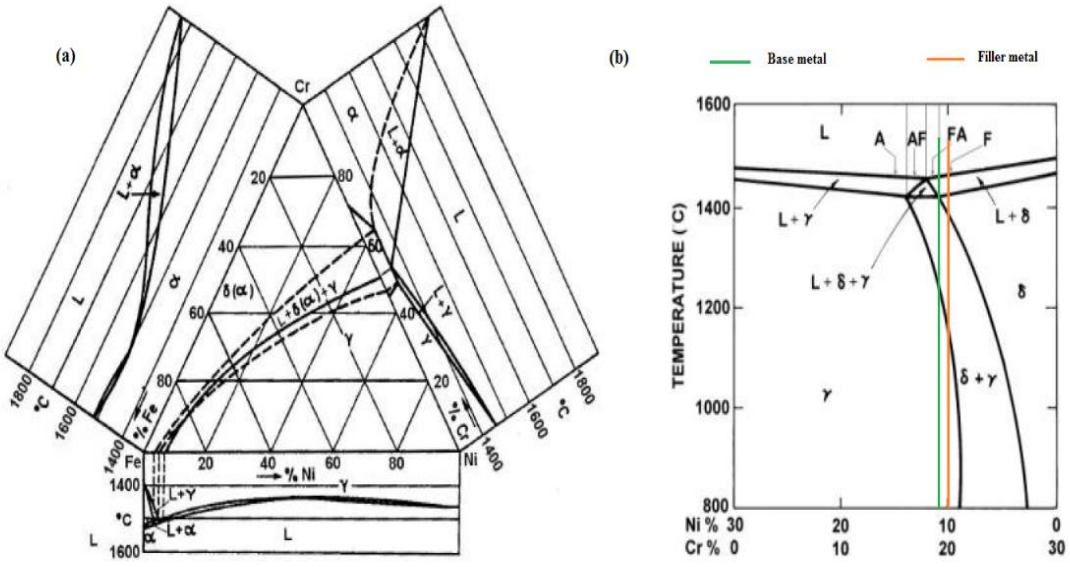

Figure 33. Fe-Cr-Ni ternary diagram (a). Derived binary diagram at 70% iron content (b). (mod. Shankar, et al., 2003, pp. 361-362)

It can be seen from figure 33 at (b) that, FA is the dominant solidification mode for the MAG welding samples, the fact indicates the presence of considerable δ-ferrite phase at elevated temperature. δ-ferrite can reach 70%-100% by the end of solidification (Shankar, et al., 2003, p. 363). Then austenite phase remains the dominant phase when the joint cools down to the room temperature.

In 1979, Hammer and Svenson have derived a formula to predict the solidification mode based on the chemical contents of the steel. Creq is equals to Cr% + 1.37 Mo% + 1.5 Si% + 2 Nb% + 3 Ti%, while Nieq equals to Ni% + 0.31 Mn%+ 22 C%+ 14.2 N%+ Cu%. Hammer and Svenson performed many experiments and they reached a conclusion that when Creq/Nieq is 1.55 the transformation from AF to FA occurs. (Shankar, et al., 2003, p. 363) The calculated ratio for the current material is 1.83 which emphasizes the result from figure 33-b.

Siewert et al., (1988) invented a new system known as the WRC-92 diagram in order to predict the ferrite contribution as a percent of the welded stainless steel material. The following figure (34) represents the WRC-92 diagram for the material utilized for the purpose of the current research (316L). it can be seen, the solidification mode is FA and ferrite content approximately was 8-10% which is similar to figure 31 and 33-b.

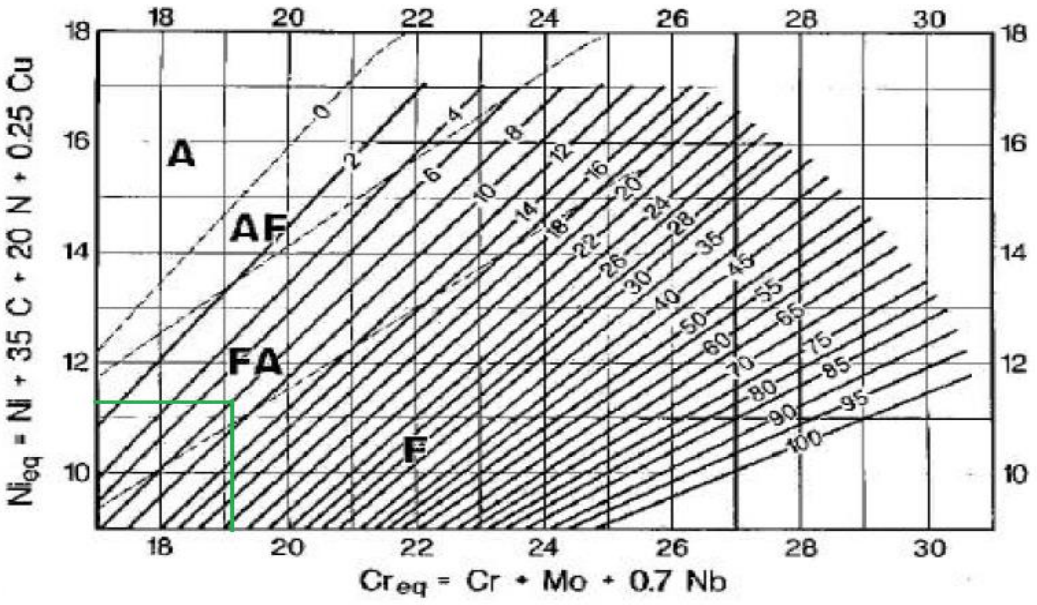

Figure 34. WRC-92 diagram for 316L austenitic stainless steel (mod. Shankar, et al., 2003, p. 364).

Many metallurgists and welding scientists have investigated the relation between solidification mode, δ-ferrite content, and formation of hot cracking in austenitic stainless steel. A common concept has been reached that FA mode is desirable in resisting the hot cracking more the residual ferrite subsequent to solidification. Another conclusion that ferrite content 5%-30%, not less not more is favourable for hot cracking prevention. (Shankar, et al., 2003, p. 378).

This fact in addition to the figures (31, 33 & 34), proves that 316L is a convenient material to resist the formation of hot cracks when welded, which improves the weldability of 316L. Figure 35 shows the susceptibility of solidification cracks formation of 316L based on Schaeffler Cr_{eq}/Ni_{eq} ratio against sulfur + phosphorus mass. Figure 35 is applicable for the MAG welding samples, it can be seen that the utilized material for the current research is not susceptible or slightly susceptible to solidification cracks.

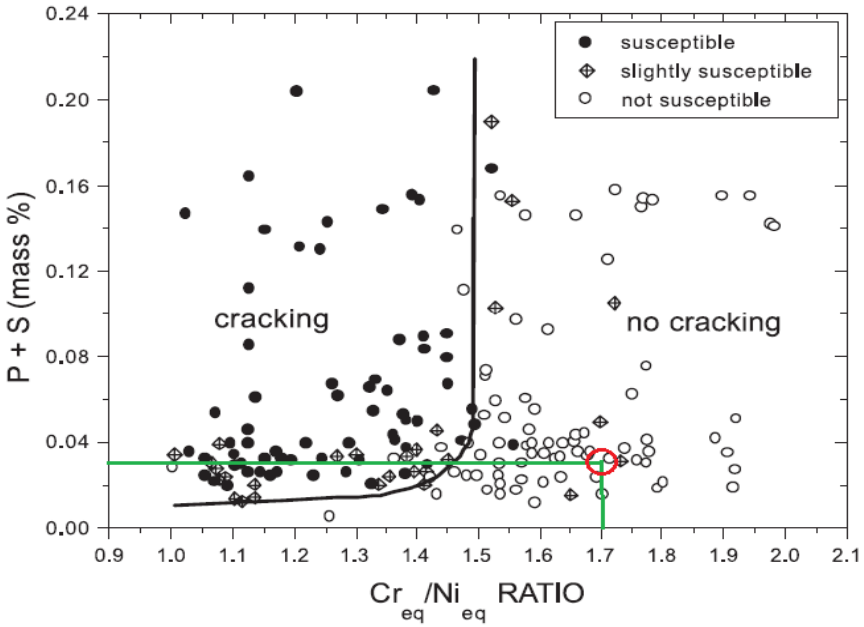

Figure 35. Hot-cracking susceptibility in austenitic stainless steel (mod. Shankar, et al., 2003, p. 368).

The following figures 36 and 37 presents the obtained microstructure images for the weld sample taken by the optical microscope at the fusion line and weld center respectively. As discussed earlier and proved with figures 31, 33 and 34, solidification mode was FA, therefore, most of δ-ferrite has transformed to austenite (γ) at room temperature. While a

tiny percentage of δ-ferrite has remained after solidification, it can be seen with dark streaks on the grain boundaries of HAZ in figure 36.

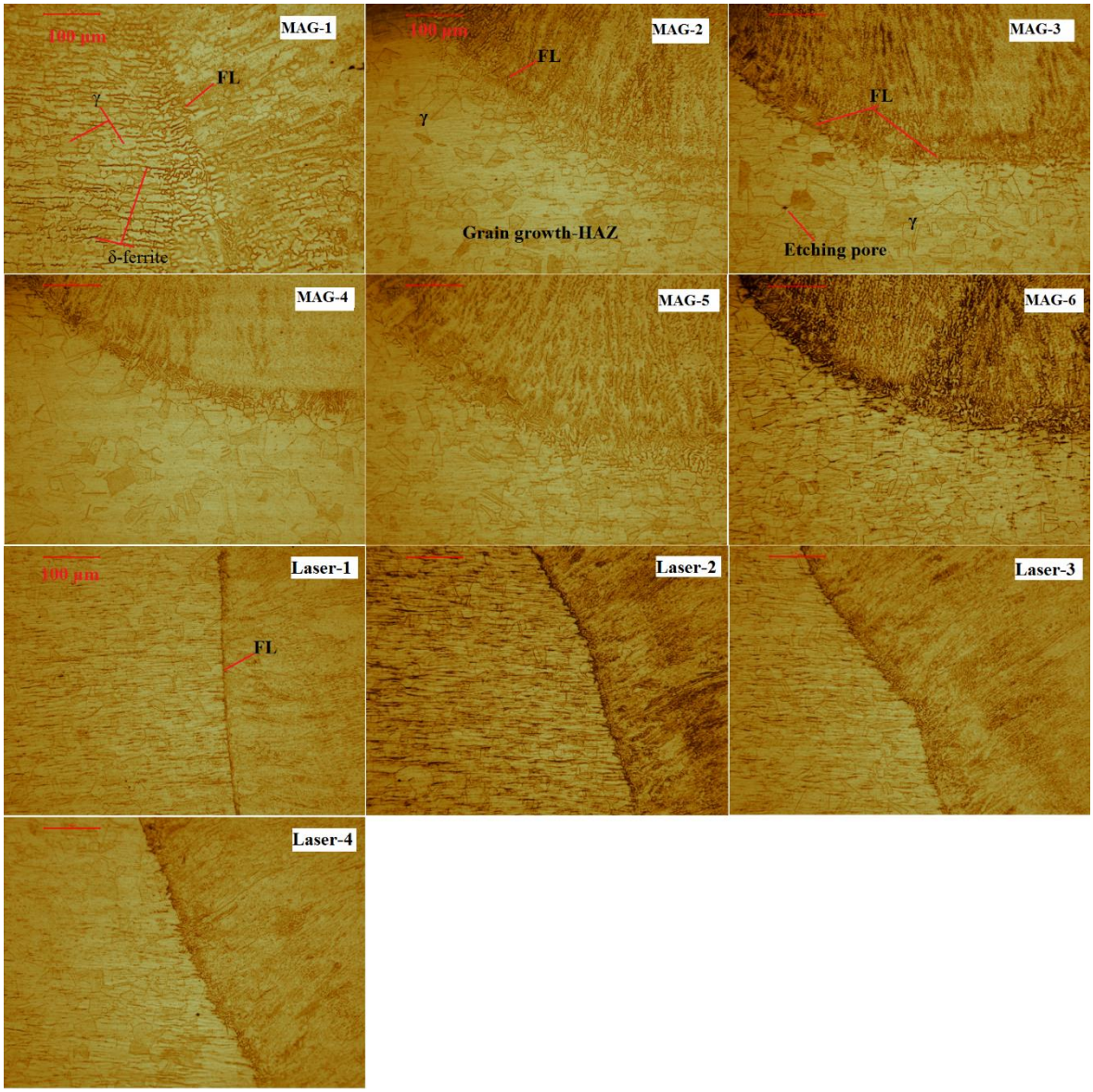

Figure 36. Optical microscope images for weld samples at the fusion line.

Detailed extrapolation for microstructure images requires knowing the applied welding parameters, which can be seen from table 6 for the MAG welding samples and table 7 for laser welding samples. Figure 37 shows the etching pores produced during the sample preparation process. A centerline crack is suspected in sample laser-2 due to the relatively high welding speed, while the welding speed in laser-1 sample was higher, other parameters such as laser power might be affected the occurrence of the centerline crack.

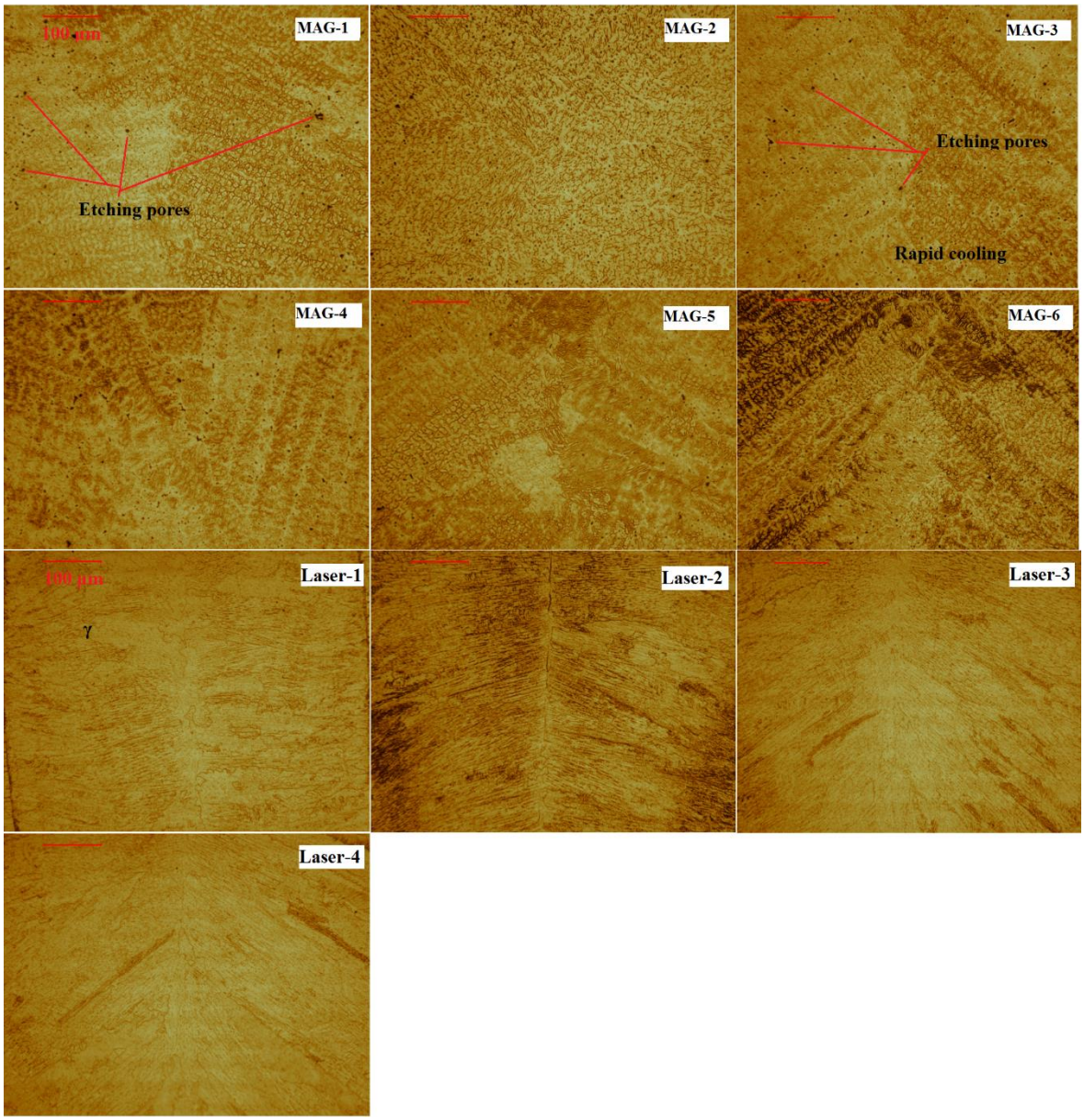

Figure 37. Optical microscope images for weld samples at the weld center.

5.5 SEM, EDS and carbides investigation results

In 4.3.5 the aim of applying SEM/EDS test has discussed in addition to the applied method and the utilized device. Two MAG samples; MAG-2 and MAG-3 with the lowest and highest welding speed; 7 mm/s and 11 mm/s respectively were tested in SEM device in addition to one laser sample (laser-3). Figure 38 presents the obtained SEM images for the samples at the fusion line and weld center. Dominant austenite phase is clearly observed in addition to the residual δ-ferrite on the grain boundaries of coarse grain area- HAZ at the vicinity of the fusion line.

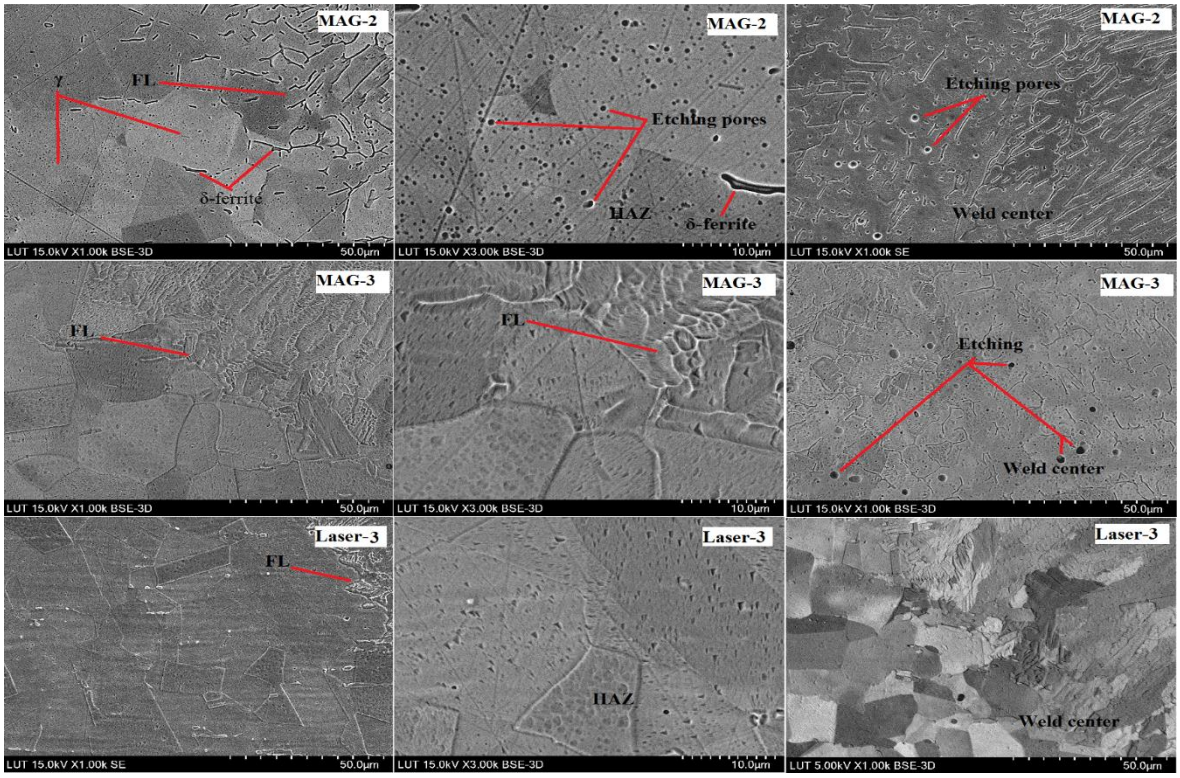

Figure 38. SEM-microstructure images for weld samples MAG-2, MAG-3 & Laser-3.

SEM investigation has revealed a clear indication for carbides formation at an area of HAZ close to the fusion line. Carbides precipitation at the base metal area is rarely occurs due to the permanent homogeneous structure in terms of chromium diffusion (Parvathavarthini, et al., 2006). Visibility of the indication in MAG-2 sample was superior to it in MAG-3 sample. EDS scan was performed for the suspected area in order to detect the nature of the observed indication. Figure 39 shows the indication in white color around the grain boundaries.

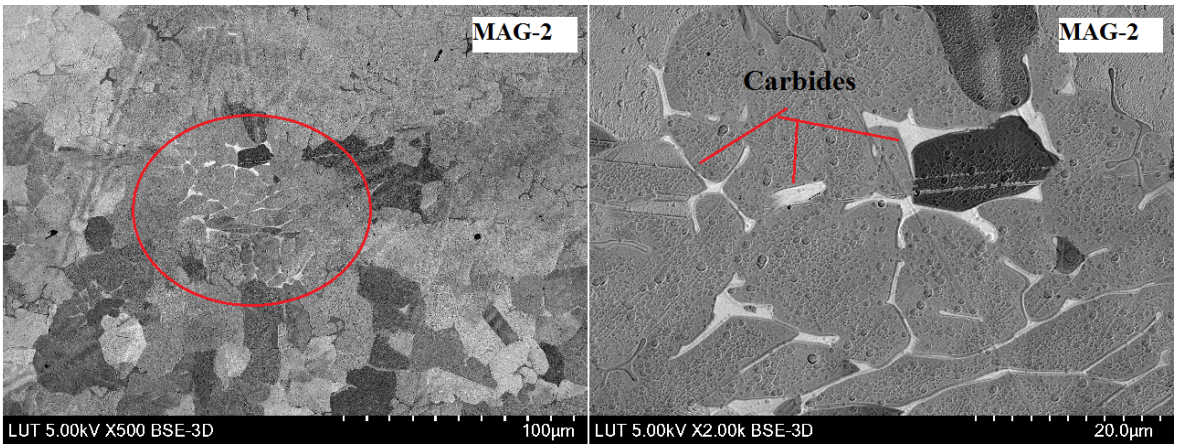

Figure 39. Carbides formation indication.

EDS mapping has been implemented for the samples MAG-2 and MAG-3 to cover the HAZ at vicinity to fusion line. Figures 40 and 41 show the EDS scan for the weld samples MAG-2 and MAG-3 respectively.

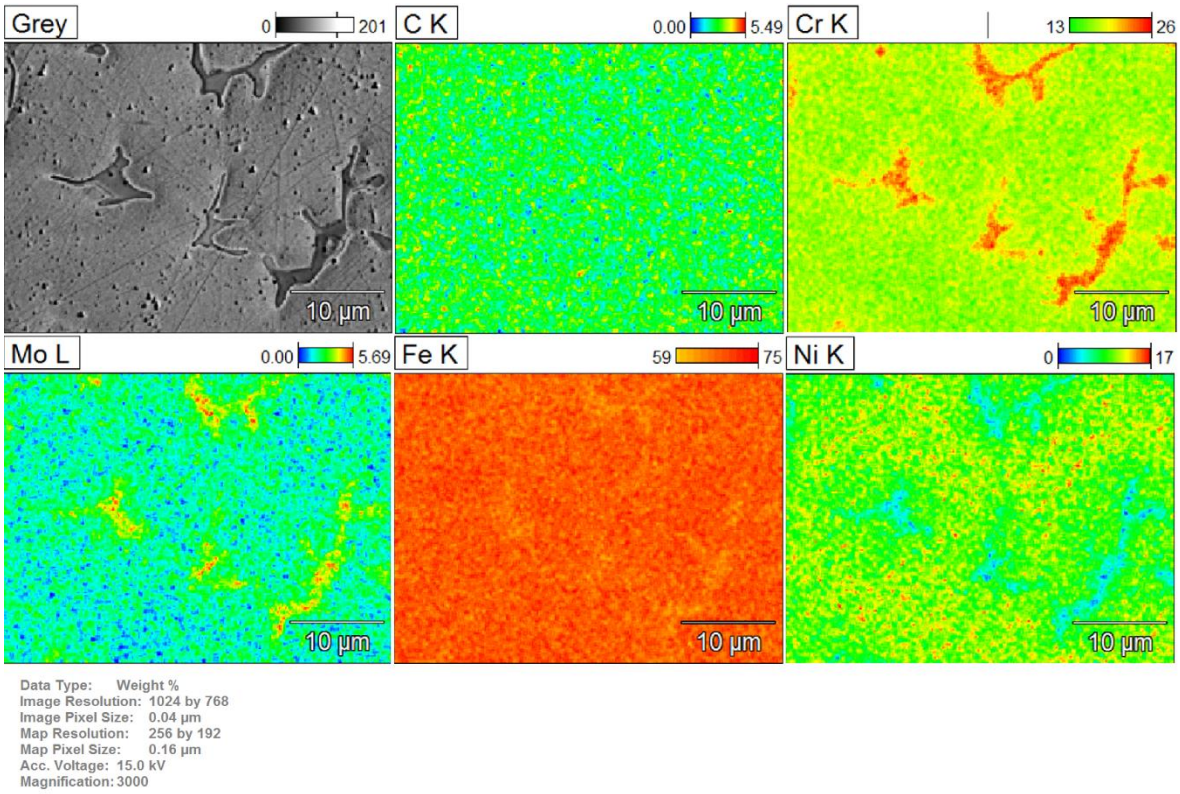

Figure 40. EDS mapping scan for sample MAG-2 at HAZ-Carbides formation.

It can be seen from the EDS images above for the tracked alloying elements; Carbon, molybdenum, nickel, and chromium the formation of the carbides on the grain boundary where chromium and molybdenum contents have increased and nickel has depleted. At the scanned area chromium percentage jumped to 26% while the original weight of chrome in the base metal was 17%, molybdenum as well increased from 2% to 5.6 %. At the same time, nickel has depleted from 10% to 2-4% which indicates the formation of a mixed carbide between C, Cr, and Mo. No change in carbon content can be observed due to the tiny percentage of carbon in 316L.

On figure 41 where MAG-3 sample was tested, carbide formation has been observed with minimal density or spread compared to MAG-3 sample which indicates the relation between welding speed or heat input and carbides formation.

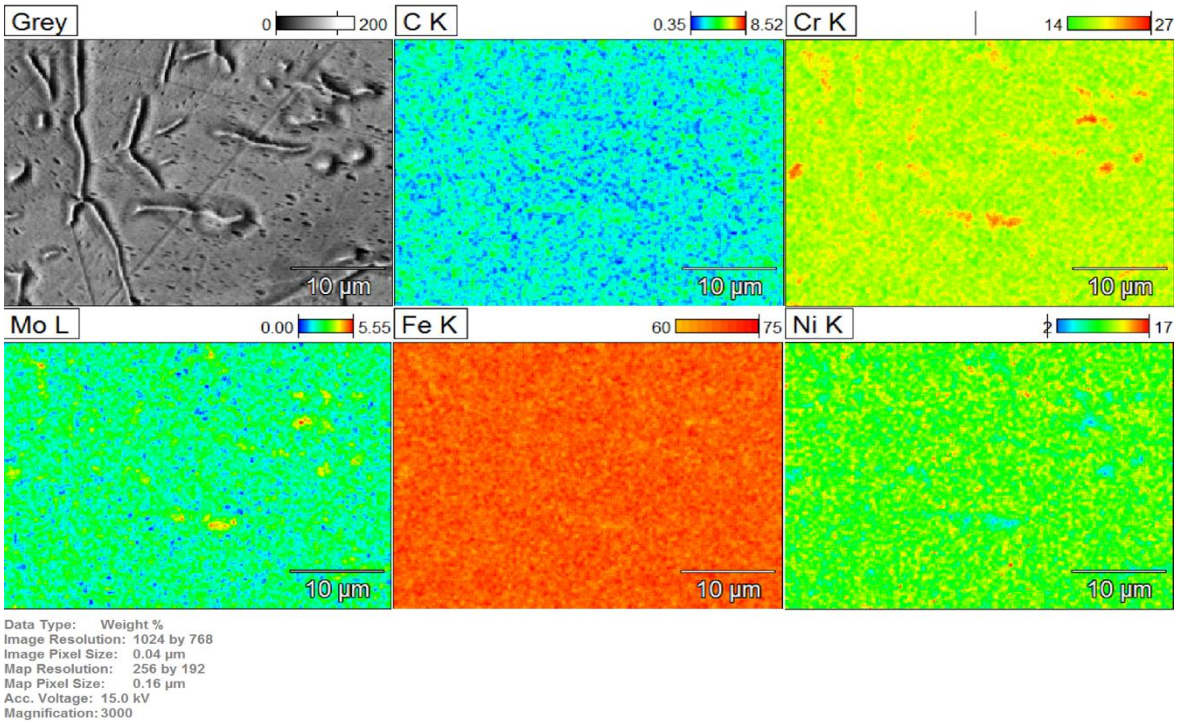

Figure 41. EDS mapping scan for sample MAG-3 at HAZ-Carbides formation.

5.6 Intergranular corrosion (IGC) and Critical cooling rate (CCR)

Excellent corrosion resistance is one of the main advantages of 316L. However, it is sensitive to IGC due to decomposition of δ-ferrite phase during the cooling time after solidification. Researches revealed that, temperature range of 550-650°C is the most critical range for δ-ferrite and austenite phases to decompose into other intermetallic phases and carbides. Cooling at a rate exceeds CCR helps to prevent IGC. (BenRhouma, et al., 2017, p. 871)

The degree of sensitization (DOS) to IGC is directly related to the microstructure and chemical composition of the stainless steel. Chromium depletion at HAZ area of welded austenitic stainless steel is a clear indication for carbides formation and susceptibility to IGC. Higher content of δ-ferrite increases the probability of IGC. (BenRhouma, et al., 2017, p. 872) The cooling rate (CR) of the weld samples MAG-1,2 and 3 is given by figure 42. CR has been measured at 500-800°C to cover the sensitive range of IGC. It can be observed from the cooling rate curves, that cooling rate increases with the higher welding speed. While carbide precipitation had seen for the lowest and highest welding speed, it is not possible to determine the CCR under the scope of the current research, further investigations are required.

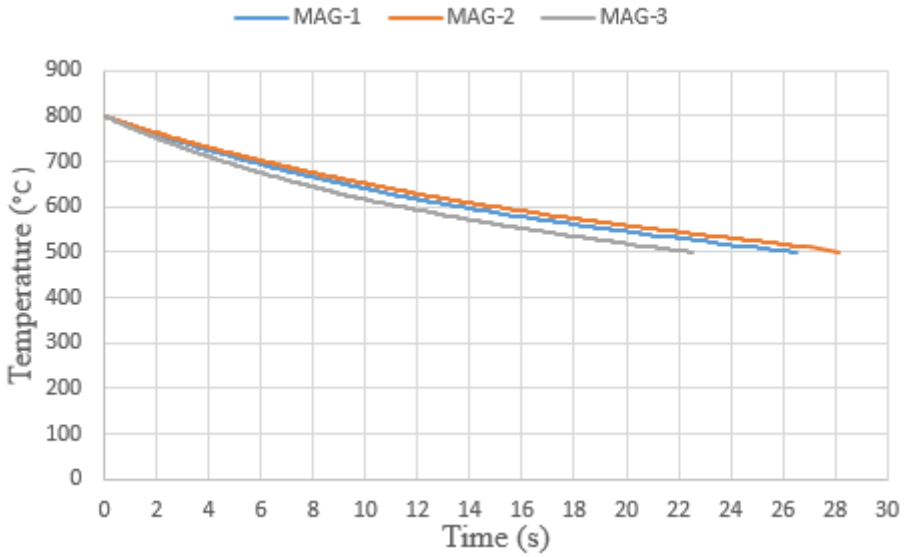

Figure 42. Cooling rate measured from the data obtained from laser temperature – sensor

According to the cooling rates curve, the dwell time between 800°C - 500°C which represents the sensitization temperature ranging (BenRhouma, et al., 2017, p. 871) is longer for MAG-2 sample compared to MAG-3. Therefore the carbides formation and susceptibility to IGC is higher for MAG-2 sample where heat input value was higher.

During the sensitization temperature ranging, δ-ferrite phase decomposes into carbides (M23C6) and other intermetallic phases. Therefore, the presence of the δ-ferrite phase is an evidence for the probability of carbides formation and IGC as a result of chromium depletion from some areas on the microstructure of austenitic stainless steel. The aging process following to the welding increases the dwell time at the sensitization range and therefore improves IGC. (BenRhouma, et al., 2017, pp. 571-572)

6 SIMULATION MODEL

3D-model for the welding joint has been drawn with SolidWorks. Then sent to ANSYS software to create a finite element model for the welding process. The objective of the simulation work is to verify the built model with the actual finding from the experimental work and to check the level of the accuracy of the model by comparing the deformation results with the actual data obtained from the experiment.

Sensitive mesh has been created and weld seam divided into 20 sections, dimensions of each is 10*3*3mm. Mechanical and thermal properties of 316L have been introduced. The simulation includes transient heat flow and plastic structural analysis. The model has been run two times with different heat conduction values to simulate welding heat input. 472 and 300 J/mm with full constraint were used to simulate MAG-5 and MAG-6 samples of the experimental work. Figure 43 shows the temperature diffusion on the plate by the end of the welding path.

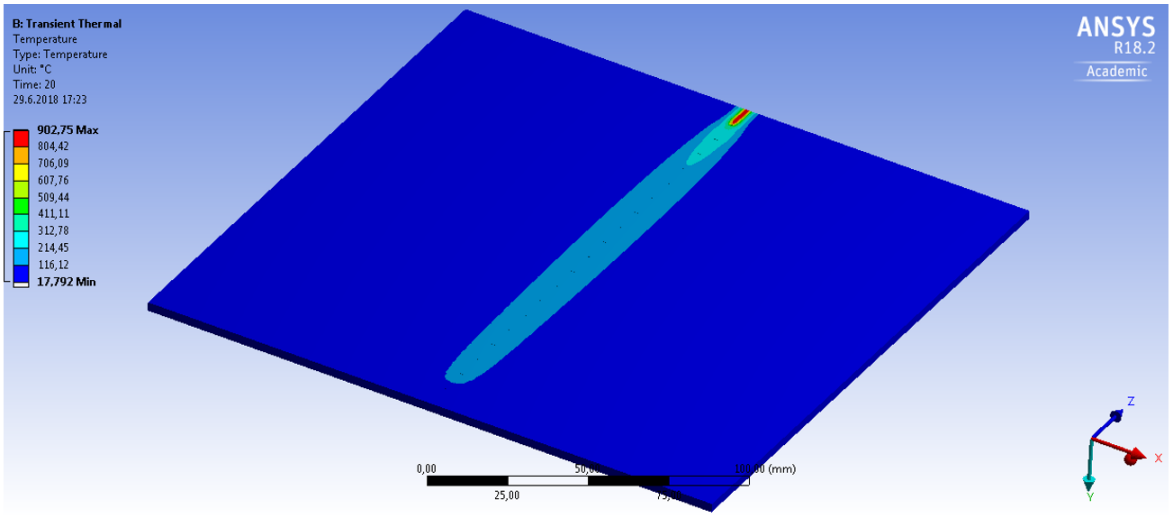

Figure 43. Simulation model-Thermal diffusion by the end of welding path.

Simulation report includes stress, temperature cycle, and distortion results. Angular and longitudinal distortion has been compared with the experimental results for both samples;

MAG-5 and MAG-6 and error percentage has registered. Figure 44 presents the obtained distortion from the simulation model.

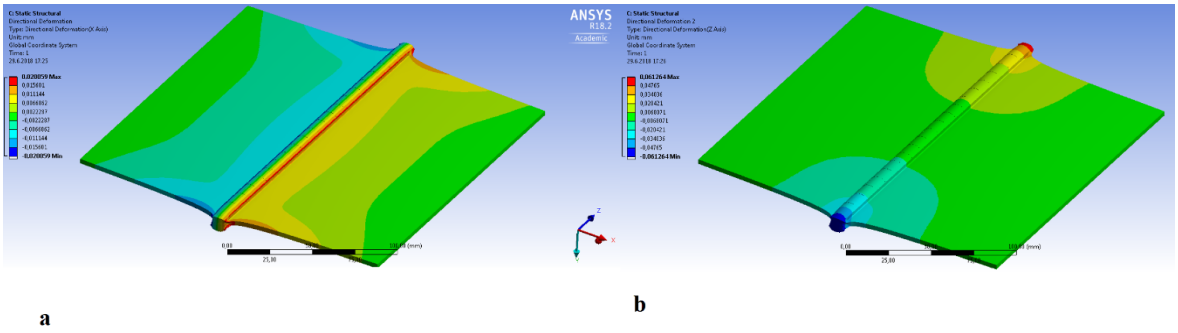

Figure 44. Deformation of the welded plate in the simulation model. Angular distortion (a) and the lonfitudinal distortion (b).

The following figure compares the simulation model result and experiments analysis for the angular distortion. Error found to be between 58% in MAG-5 sample to 60% in MAG-3. As can be seen from figure 45, weld seam geometry is not similar for simulation and real case due to the absence of reinforcement and root extension in the simulation model. Simulation model results show uniform distortion on both sides of the plate, which is not a real situation.

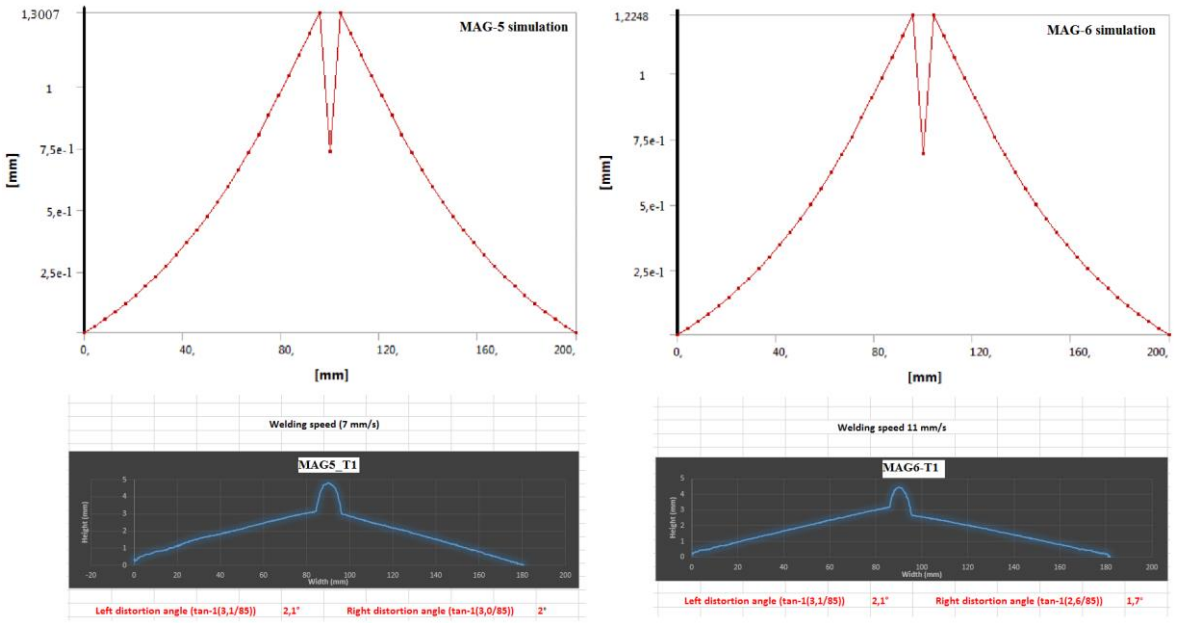

Figure 45. Difference between the simulation model and experiment in angular distortion.

Figure 46 shows the Difference between the simulation model and experiment in longitudinal distortion where the error in the model result was 52 % for MAG-5 and 64% for MAG-6. The significant deviation in the simulation results can be clarified by the lack of accuracy in introducing the welding parameters into the simulation software.

Many of the welding parameters such as welding current, voltage and travel speed cannot be introduced individually into the ANSYS model. Alternatively, the transferred heat from the weld source to the plate was defined as a single value to simulate the experemintal, calculated values of the heat input (KJ/mm). Therefore, the accurate simulation of a welding process requires a specialized welding software to be coupled with the FEM in order to simulate the process accurately.

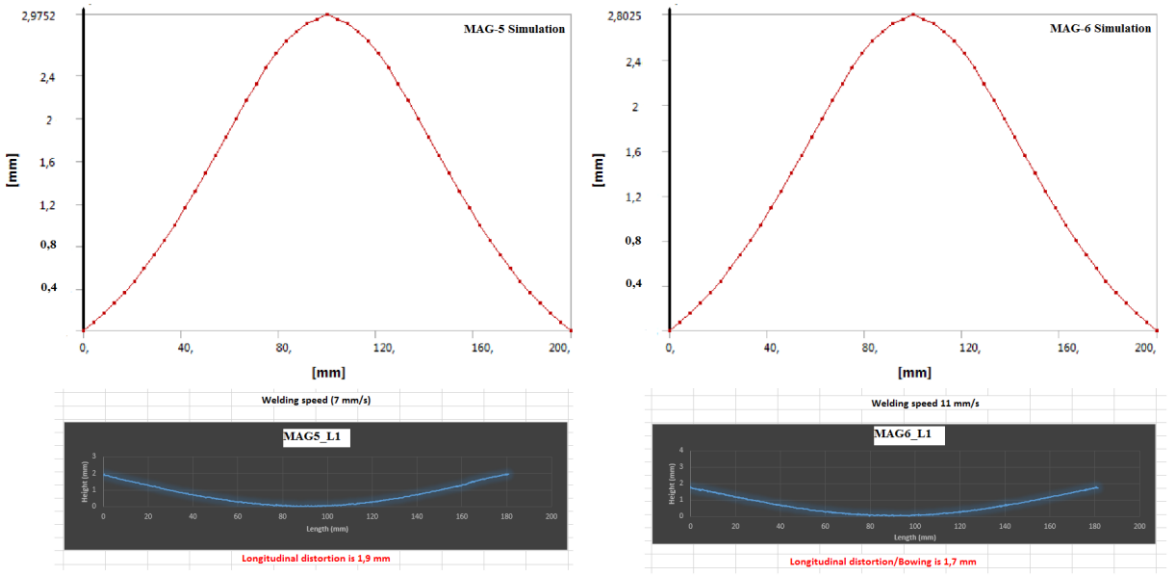

Figure 46. Difference between the simulation model and experiment in bowing measurement.

7 CONCLUSION

Austenitic stainless steels are one of the most susceptible metals to welding distortion due to their thermal properties. Distortion is a real concern for welded structures, repairing distortion represents 20-30% of the workload in the shipbuilding industry alone. The present research aimed to reveal the effect of the welding process and the introduced heat into the weld joint on the produced distortion. Therefore, ten samples of 3mm plate, 316L material, and butt-joint have been welded applying robotic-MAG and fiber laser welding, different values of heat input were set up by altering the welding speed.

Sensitive laser 2-D device was utilized to measure the distortion magnitude and orientation for each setup. Beside distortion measurement, optical micrograph was utilized to reveal the consequence of the welding heat on the microstructure and phase transformation for the welded samples of 316L austenitic stainless steel. Sensitization to intergranular corrosion and carbides formation were tested applying SEM and EDS tests. Furthermore, FEM has been built in order to validate the simulation model based on the real results from the experimental work. According to the experimental results, the following conclusion can be drawn.

- Fiber laser-welding has produced smaller fusion zone and minimal heat affected zone compared to MAG weld hence, quite less angular distortion and bowing were produced on the laser welded samples.
- Travel speed of 2.2 m/min and power of 2.5 kW in the laser welding process has achieved the optimum weld geometry, free of distortion. However higher welding speed produced weld joints with lack of penetration.
- For MAG welding samples, welding speed is inversely proportional to angular distortion and longitudinal distortion as well. Accordingly, heat input per unit length (kJ/mm) is proportional to angular distortion and bending. Multiplication of the heat input 1.5 times leads to an angular distortion four times worse. Best deformation result for MAG welds was found when the welding speed was 11 mm/s, lower speeds have produced excess root penetration.

- Constraints or mechanical clamp has a minimal influence to reduce distortion, it has changed the orientation of the distortion angle and bowing rather than total elimination of distortion.
- 316L stainless steel showed FA solidification mode for the MAG welding samples where the ferrite content is a 10% nearly, which is an appropriate amount to resist the formation of the hot cracks.
- High- magnification SEM images have shown an area with carbides precipitation on HAZ at the vicinity of the fusion line for sample MAG2 and MAG3 where the heat input were 0.472 and 0.3 KJ/mm respectively. Precipitations were investigated with EDS-mapping which revealed increasing of chromium and molybdenum against depletion of nickel on the precipitation area. Precipitation was heavier for MAG2 sample which indicates the proportional relation between the heat input and carbides formation or susceptibility to IGC.
- Numerical results of distortion obtained by the FE model have shown a significant deviation from the experimental results. The lack of accuracy in introducing the welding parameters into the simulation software justifies the deviation in the results. The basic welding parameters such as welding current, voltage, and travel speed were not introduced individually into the ANSYS model. Alternatively, the transferred heat from the welding source to the plate was defined as a single value.

8 FURTHER STUDIES

The accurate determination of the optimum heat input to mitigate distortion in 316L stainless steel requires widening the tested sample. In a specific sense, more values of welding speeds have to be tested in order to represent a wider range of the heat input. An effective plan for samples preparation prior to micrography can produce images with better quality. Therefore, microstructure investigation can be improved. FE simulation model results have to be validated utilizing the experimental data, hence the model can represent an effective tool to predict distortions in 316L plates, specialized welding software can be used either separately or attached with ANSYS in order to define the welding parameters accurately.

Fixation techniques rather than the mechanical clamping can be tested to study their influence in reducing the welding distortion. Ferritoscope device can be used for the accurate determination of the ferrite content in the microstructure to identify the relation between the heat input and the solidification cracks. For the future relevant studies, the effect of the heat input on the produced mechanical properties such as the toughness and the tensile strength can be investigated. Accordingly, the weld quality of 316L stainless steel would have been covered in different aspects.

REFERENCES

Adamczuk, p. C., Machado, I. G. & Mazzaferro, J. E., 2017. Methodology for predicting the angular distortion in multi-pass butt-joint welding. *Journal of Materials Processing Technology,* Volume 240, pp. 305-313.

Baddoo, N. R., 2008. Stainless steel in construction: A review of research, applications, challenges and opportunities. *Journal of Constructional Steel Research,* Volume 64, pp. 1199-1206.

Beddoes, J. & Parr, J. G., 1999. *Introduction to Stainless steel.* 3rd ed. washinton, D.C: Materials Park (OH) : ASM International 1999.

BenRhouma, A., Amadou, T., Sidhom, H. & Braham, C., 2017. Correlation between microstructure and intergranular corrosion behavior of low delta-ferrite content AISI 316L aged in the range 550-700 C. *Journal of Alloys and Compounds,* Volume 708, pp. 871-886.

Brown, J., 2018. *Simplit Tack Weld.* [Online] Available at:http://simplir.me/tack-weld/ [Accessed 06 March 2018].

Budkin, Y. V. & Redchits, A. V., 2013. A criterial approach to evaluating the weldability of materials and alloys for welded aircraft structures. *Welding International,* 27(9), pp. 687-689.

Camilleri, D., Gray, T. G. & Nash, D., 2010. Mitigation of welding distortion and residual stresses via cryogenic CO_2 cooling -a numerical investigation. [Online] Available at: https://pure.strath.ac.uk/portal/files/15658655/Nash_DH_strathprints_Mitigation_of_welding_distortion_and_residual_stresses_via_cryogenic_co2_cooling..._Mar_2010.pdf [Accessed 06 March 2018].

Cao, L. et al., 2017. Effects of Welding Speed on Microstructure and Mechanical Property of Fiber Laser Welded Dissimilar Butt Joints between AISI316L and EH36. *Metals,* 7(270), pp. 1-13.

Damen, S., 2015. *Angular distortion and buckling in welded plate.* [Online] Available at: http://www.m2i.nl/portfolio-items/angular-distortion-and-buckling-in-welded-plate-damen-schelde/ [Accessed 05 March 2018].

Deng, D. & Murakawa, H., 2008. Prediction of welding distortion and residual stress in a thin plate butt-welded joint. *Computational Material science,* Volume 43, pp. 353-365.

Devendranath, K. et al., 2015. Effect of Filler Metals on the Weldability and Mechanical Properties of Multi-pass PCGTA Weldments of AISI 316L. *Journal of Material Engineering and Performance,* 24(4), pp. 1602-1613.

Ghosh, P. K., Dorn, L., Kulkarni, S. & Hofmann, F., 2009. Arc characteristics and behaviour of metal transfer in pulsed current GMA welding of stainless steel. *journal of materials processing technology,* Volume 209, pp. 1262-1274.

Gietzelt, T., Wunsch, T., Eichhorn, L. & Dittmeyer, R., 2015. Impact of Different Parameters for Pulsed- Laser Welding of the Austenitic Stainless 304. *Chemical Engineering Technology,* 38(12), pp. 2189-2197.

Grigorenko, G. M. & Kostin, V. A., 2013. Criteria for evaluating the weldability of steels. *Taylor & Francis,* 27(10), pp. 815-820.

Harris, I. D. et al., 2004. Gas Metal Arc Welding. In: A. O`Brien, ed. *Welding Handbook, Welding Processes, Part 1.* Miami: American Welding Society, pp. 147-205.

Ion, J. C. & Ashby, M. F., 2011. *Weldability charts for constructional steels.* Nancy, 6th EEIGM International Conference on Advanced Materials Research .

ISSF, 2018. Worldstainless.org. [Online] Available at:http://www.worldstainless.org/files/issf/non-image-files/PDF/ISSF_Stainless_Steel_in_Figures_2018_English_Public.pdf [Accessed 26 09 2018].

Kah, P., Suoranta, R. & Martikainen, J., 2013. Advanced gas metal arc welding processes. *International journal of advanced manufacturing technology,* Volume 67, pp. 655-674.

Kikani, P., 2016. Study of Shielded Gases for MIG Welding. *Journal of Materials & Metallurgical Engineering,* 6(1), pp. 6-10.

Kozuh, S., Gojic, M. & Kosec, L., 2009. Mechanical properties and microstructure of austenitic stainless after welding and post-weld heat treatment. *Kovove Metallic Materials,* Volume 47, pp. 253-262.

Leggatt, R. H., 2008. Residual stresses in welded structures. *International Journal of Pressure Vessels and Piping,* Volume 85, pp. 144-151.

Lippold, J. C., 2015. *Welding Metallurgy and Weldability.* 1st ed. Ohio: John Wiley & Sons,Inc., Hoboken, New Jersey.

Nasir, N. S. M., Azhar, M. K., Mamat, s. & Ahmed, M. i., 2016. REVIEW ON WELDING RESIDUAL STRESS. *ARPN Journal of Engineering and Applied Sciences,* 11(9), pp. 6166-6175.

Outokumpu, 2013. *Handbook of Stainless Steel.* 1st ed. Avesta: Outokumpu Oyj.

Parvathavarthini, N. et al., 2006. Sensitization behaviour of modified 316N and 316L stainless steel weld metals after complex annealing and stress relieving cycles. *Journal of Nuclear Materials,* Volume 355, pp. 86-82.

Puchi-Cabrera, E. S. et al., 2009. Fatigue life of AISI 316L stainless steel welded joints, obtained by GMAW. *Welding International,* 23(10), pp. 778-788.

Radaj, D., 1992. *Heat Effects of Welding- Temperature field, Residual stress, Distortion.* 2nd ed. Berlin: Springer-Verlag.

Shankar, V., Gill, T. P., Mannan, S. L. & Sundaresan, S., 2003. Effect of nitrogen addition on microstructure and fusion zone cracking in type 316L stainless steel weld metal. *Materials Science and Engineering,* Volume A343, pp. 170-181.

Shankar, V., Gill, T. P., Mannan, S. L. & Sundaresan, S., 2003. Solidification cracking in austenitic stainless steel welds. *Sadhana- Academy Proceedings in Engineering Sciences,* 28(3 &4), pp. 359-382.

Slane, 2010. *Sidexsideworld.com.* [Online] Available at:http://www.sidexsideworld.com/threads/mig-welding-process-overview.23305/ [Accessed 19 March 2018].

Sokolov, M. & Salminen, A., 2014. Improving Laser Beam Welding Efficiency. *Scientific research,* Volume 6, pp. 559-571.

Sowards, J. W. et al., 2012. Solidification behavior and weldability of dissimilar welds between a Cr-free, Ni-Cu welding consumables and type 304L austenitic stainless steel. *Metallurgical and Materials Transactions A,* Volume 43A, pp. 1209-1222.

Tamaki, K., Kawakami, H. & Suzuki, J., 2003. Effects of carbon content and peritectic reaction on hot cracking of high-carbon steel weld metal. *Welding International,* 17(1), pp. 26-35.

Teng, T. L. & Lin, C. C., 1998. Effect of welding conditions on residual stresses due to butt welds. *International Journal of Pressure Vessels and Piping,* Volume 75, pp. 857-864.

Trevisan, R. E., Braga, E. & Fals, H. C., 2003. Effects of nitrogen and pulsed mean welding current in AISI 316 austenitic steel solidification cracks. *Welding International,* 17(4), pp. 298-302.

TWI, 2016. *Distortion Control - Prevention by fabrication techniques.* [Online] Available at: https://www.twi-global.com/technical-knowledge/job-knowledge/distortion-control-prevention-by-fabrication-techniques-036/ [Accessed 06 March 2018].

TWI, 2017. *Distortion - prevention by design.* [Online] Available at: https://www.twi-global.com/technical-knowledge/job-knowledge/distortion-prevention-by-design-034/ [Accessed06March2018].

TWI, 2018.*Distortion types and causes.* [Online] Available at:https://www.twi-global.com/technical-knowledge/job-knowledge/distortion-types-and-causes-033/ [Accessed5March2018].

Verhaeghe, G., 1999. *Predictive formula for weld distortion- a critical review.* 1st ed. Cambridge: Woodhead Publishing Ltd.

Verneau, M. & Mecozzi, G., 2000. *Effect of residual stresses on localised corrosion and stress resistance of stainless steel,* Belgium: European commission, Science Research Development.

Weman, K., 2012. *The weldability of steel.* 2nd ed. Philadelphia: Woodhead Publishing India Private Limited.

Weman, K., 2012. *Welding Processes Handbook.* 2nd ed. Cambridge: Woodhead Publishing Limited.

Younes, C. M., Steele, A. M., Nicholson, J. A. & Barnett, C. J., 2013. Influnce of hydrogen content on the tensile properties and fracture of austenitic stainless steel welds. *International Journal of Hydrogen Energy,* Volume 38, pp. 4864-4876.

Zhang, L. et al., 2013. Residual stress,micro-hardness and tensile properties of ANSI 304 stainless steel thick sheet by fiber laser welding. *Materials Science & Engineering,* Volume A 561, pp. 136-144.

APPENDICES

APPENDIX I

Inspection certificate of 316L carried out by Outokumpu stainless Oy.

Delivery address, Empfänger, Lieu de livraison TIBNOR OY JÄRVENPÄÄ SERVICE CENTER ASPONKATU 2 04400 JÄRVENPÄÄ SUOMI-FINLAND	TIBNOR OY NIINISTÖNKATU 7 05800 HYVINKÄÄ SUOMI-FINLAND
Requirements, Anforderungen, Exigences EN 10088-4:2009 AD 2000 W2, W10 & EN 10028-7:2016 ASTM A240/A240M ASME SA-240/SA-240M II A ED. 2015	Our Order No. Unser Auftrag Nr. Notre commande n°: 300461869 Your order, Ihre Bestellung, Votre commande: TILAUS 2.1.2018
Product, Erzeugnisform, Produit COIL , STAINLESS STEEL	Mark of Manufacturer, Zeichen des Lieferwerkes, Signe de producteur: outokumpu Process, Erschmelzungsart, Mode de fusion: AOD
Grade, Werkstoff, Nuance 1.4404 TYPE 316L 1.4401	Tolerances Toleranzen, Tolérances EN ISO 9445-2
Marking, Kennzeichnung, Marquage 1.4404 2B	Marks, Versandzeichen, Marques

Inspector's stamp, Zeichen d. Sachverst., Poinçon de l'expert

Line, Reihe, Ligne	Item, Position, Poste	Charge-test No., Schmelze-Probe Nr., Coulée n°	Size, Abmessungen, Dimensions	Quantity, Stückzahl, Nombre	Weight, Gewicht, Poids	Finish, Ausführung, Fini EN/ASTM
1	2	77416 1	3,0 X 1000 MM		8060 KG	2B

CE 14 0045-CPR-0567

Charge no., Schmelze Nr., Coulée n°	Chemical composition, Chemische Zusammensetzung, Composition chimiques											
	C %	Si %	Mn %	P %	S %	Cr %	Ni %	MO %	N %			
77416	0,018	0,45	0,98	0,038	0,001	17,1	10,0	2,04	0,036			

Line, Reihe, Ligne	Mechanical properties, Mechanische Eigenschaften, Caracteristiques mecaniques								Tensile test, Zugversuch, Essai de traction
	Sample ID, Proben ID, Echantillon	Rp0.2 MPa	Rp1.0 MPa	Rm MPa	A5 %	A50 %	%	Hardness, Härte, Dureté HBW	ISO 6892-1:2009 A224 SAMPLES PERPENDICULAR TO THE ROLLING DIRECTION
1	01	317	346	603	56	52		182	APPROVED ACC.TO AD2000-W0 WITH VERIFICATION OF THE UNIFORMITY OVER THE STRIP LENGTH. CERTIFIED ACC.TO PED 2014/68/EU BY TÜV NORD REG. NO. 0045. DOPS ACC. TO CPR AVAILABLE ON THE WEB PAGE BY STEEL NUMBER
	02	311	342	608	56	52		179	

Identity test, Verwechslungsprüfung, Controle d'identification: OK
Sizes, Abmessungen, Dimensions: OK
Surface, Oberfläche, Surface: OK
Test of intergran. corros, Prüfung auf interkrist. Korros, Test de corros. intercrist.
EN ISO 3651-2 A: OK

ASTM A240/A240M
ASME SA-240/SA-240M II A ED. 2015
TYPE 316
EN 10088-2:2014/1.4404, 1.4401
NACE MR0103/ISO 17945 AND
NACE MR0175/ISO 15156-1 / NACE MR0175/ISO 15156-3
HEAT TREATMENT 1070 C
SOLUTION ANNEALED
A001.A02548 4500985721

We certify that the above mentioned products comply with the terms of the order contract.
Wir bestätigen, dass die Lieferung den Vereinbarungen der Bestellannahme entspricht.
Nous certifions que les produits énumérés ci-dessus sont conformes aux prescriptions de la commande.

This test certificate is made by controlled ADP-system and is valid without signature.
Dieses Zeugnis wurde von einem überprüften Datenverarbeitungssystem erstellt und ist ohne Unterschrift gültig.
Ce certificat a été établi par un système informatique contrôlé et est valide sans signature.

Outokumpu Stainless Oy

Authorized inspector, Werkssachverständiger, Inspecteur autorisé: MIRVA KUJANSUU

FI-95490 Tornio, Finland
Tel. +358 16 4521,email certificate.tornio@outokumpu.com,
www.outokumpu.com
Domicile: Tornio, Finland. Business Identity Code 0623316-9

Angular distortion at the center of welded plates, T-2 line

Welding speed 9 mm/s

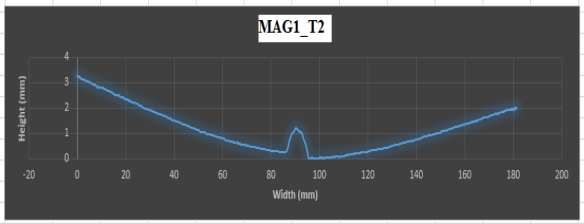

Angular distortion-Left side (tan-1(3,28/85)) 2,45° Angular distortion-Right side (tan-1(2,1/85)) 1,57°

Welding speed 11 mm/s

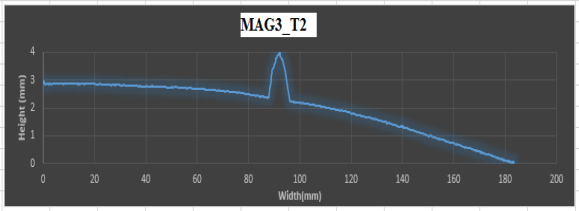

Left distortion angle (tan-1 (0.5/87)) 0,33° Right distortion angle (tan-1 (2.23/85)) 1,5°

Welding speed (7 mm/s)

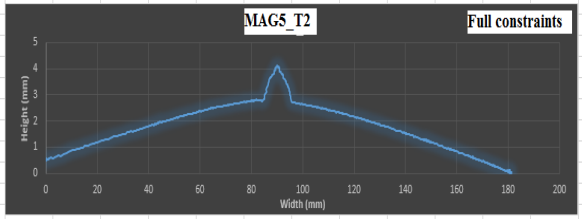

Left distortion angle (tan-1(2,3/85)) 1,5° Right distortion angle (tan-1(2,7/85)) 1,8°

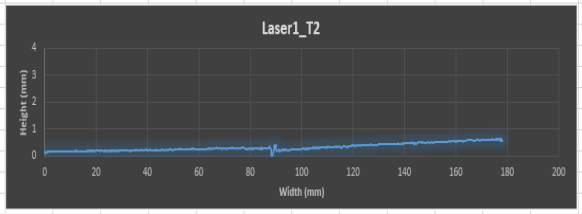

Angular distortion-Left side (tan-1(0/85)) 0 Angular distortion-Right side (tan-1(0,6/85)) 0,4°

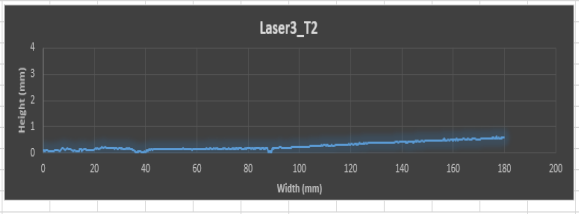

Angular distortion-Left side (tan-1 (0/85)) 0 Angular distortion-Right side (tan-1(0,6/85)) 0,4°

Welding speed 7 mm/s

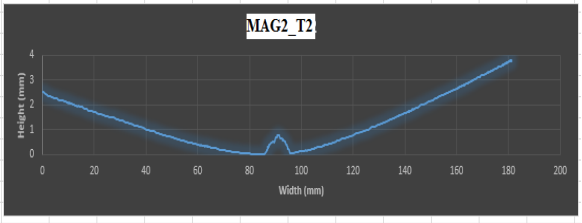

Distortion anele-Left side (tan-1(2.55/85)) 1.7° Distortion anele-Rieht side (tan-1(3.7/85)) 2.5°

Welding speed (9mm/s)

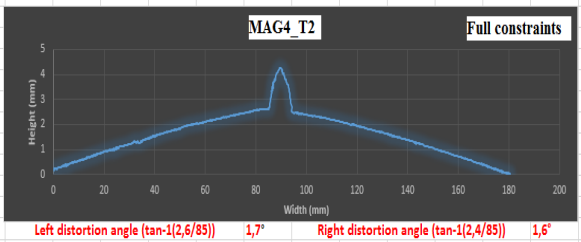

Left distortion angle (tan-1(2,6/85)) 1,7° Right distortion angle (tan-1(2,4/85)) 1,6°

Welding speed 11 mm/s

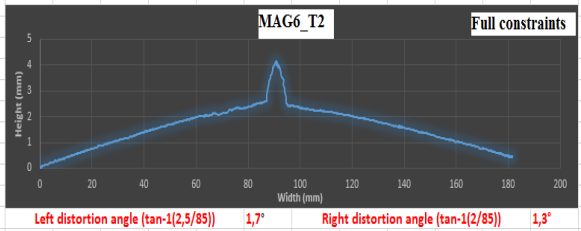

Left distortion angle (tan-1(2,5/85)) 1,7° Right distortion angle (tan-1(2/85)) 1,3°

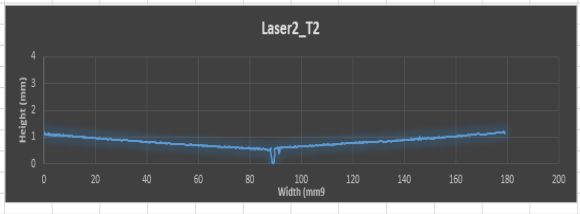

Angular distortion-Left side (tan-1(1,0/85)) 0.7° Angular distortion-Right side (tan-1(1,2/85)) 0.8°

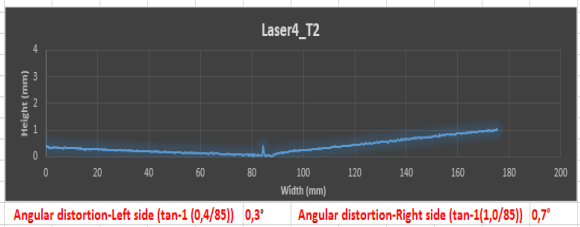

Angular distortion-Left side (tan-1 (0,4/85)) 0,3° Angular distortion-Right side (tan-1(1,0/85)) 0,7°

Angular distortion at the end of welded plates, T-3 line

Welding speed 9 mm/s

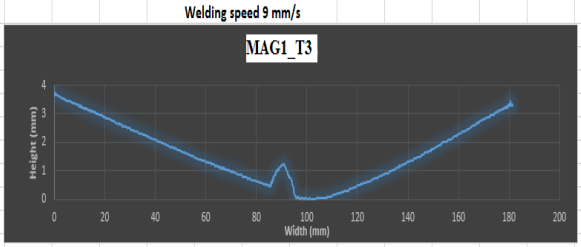

Angular distortion-Left side (tan-1(3,7/85)) 2,5° Angular distortion-Right side (tan-1(3,2/85)) 2,1°

Welding speed 7 mm/s

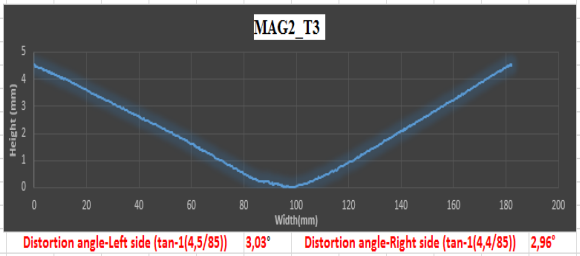

Distortion angle-Left side (tan-1(4,5/85)) 3,03° Distortion angle-Right side (tan-1(4,4/85)) 2,96°

Welding speed 11 mm/s

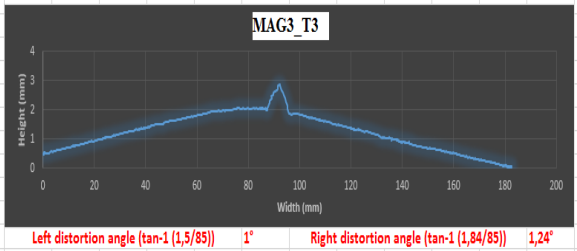

Left distortion angle (tan-1 (1,5/85)) 1° Right distortion angle (tan-1 (1,84/85)) 1,24°

Welding speed (9mm/s)

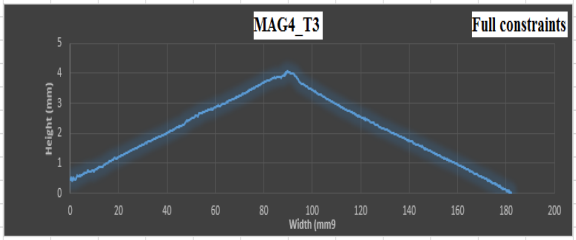

Left distortion angle (tan-1(3,3/85)) 2,2° Right distortion angle (tan-1(3,6/85)) 2,4°

Welding speed (7 mm/s)

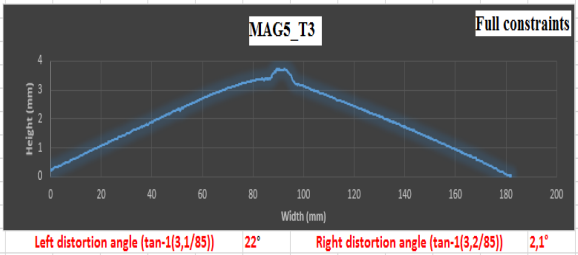

Left distortion angle (tan-1(3,1/85)) 22° Right distortion angle (tan-1(3,2/85)) 2,1°

Welding speed 11 mm/s

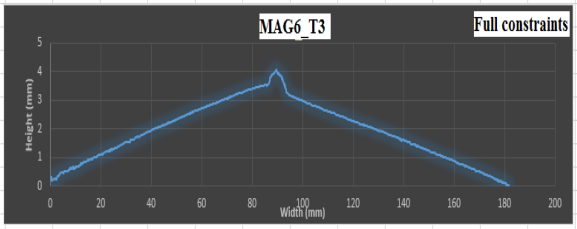

Left distortion angle (tan-1(3,4/85)) 2,3° Right distortion angle (tan-1(3,3/85)) 2,2°

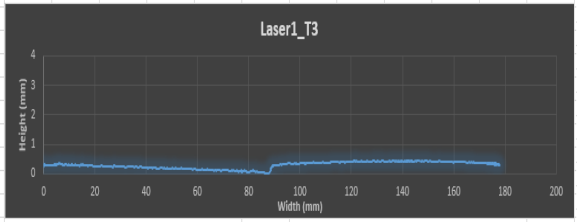

Angular distortion-Left side (tan-1(0,27/85)) 0,2° Angular distortion-Right side (tan-1(0,3/85)) 0,2°

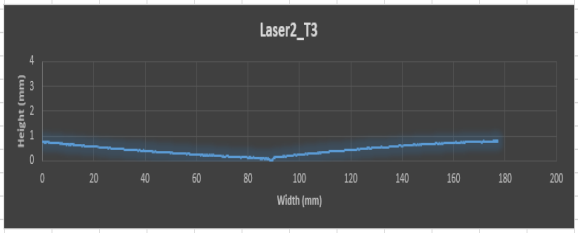

Angular distortion-Left side (tan-1(0,75/85)) 0,5° Angular distortion-Right side (tan-1(0,9/85)) 0,6°

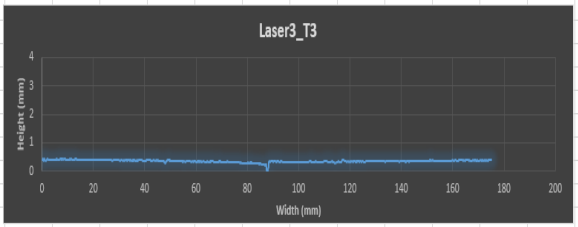

Angular distortion-Left side (tan-1 (0,4/85)) 0,3° Angular distortion-Right side (tan-1(0,4/85)) 0,3°

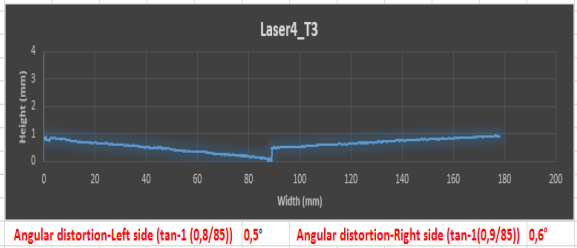

Angular distortion-Left side (tan-1 (0,8/85)) 0,5° Angular distortion-Right side (tan-1(0,9/85)) 0,6°

APPENDIX IV

WPS for the MAG welded samples.

Parent material	**316l (1.4404)**				
Material thickness	**3mm**	Joint type 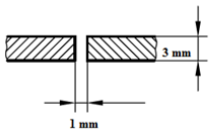 Air gap is 1.2 mm		Welding sequences Single pass.	
Outside diameter	-				
Welding process	**Robotic MAG**				
Welding position	**Flat**				
Groove preparation	**square**				
Groove cleaning	-				
Workpiece fixturing	-				
Tack welding	**Both ends- TIG welding**				
Back gouging	-				
Backing	**Copper backing**				
	Designation of consumables and trade name		Torch angle		**5° pushing**
	Filler material classification	**EN ISO 14343: G19 12 3 LSi**	Inclination angle		
		AWS A5.9 : ER316L Si	Distance contact tube to workpiece		
			Preheating and interpass temperature		
	Filler material trade name	**Elga Cromamig 316L Si**	Preheat temperature		-
			Interpass temperature		-
	Flux		Preheating method		-
	Shielding gas	**M21 Ar + 2% Co_2**	Temperature measurement		-
	Flow rate	**16 L/min**	Post-weld heat treatment		
	Plasma gas	-	Method		-
	Flow rate	-	Heating rate		-
	Backing gas	-	Temperature		-
	Flow rate	-	Time		-
	Type of current	**DC+**	Cooling rate		-
	Polarity		Post-weld treatment	-	
Remarks:			Date and name:		

Sample	Process	Size of filler metal Ø (mm)	Current (A)	Voltage (V)	Travel speed (mm/s)	Wire feed rate (m/min)	Heat input (kJ/mm)	Run-out length (mm)	Weaving frequency (Hz)	Amplitude (mm)	Remarks
1	MAG	1.0	160	25	9.0	9.5	0.355	18	-	-	
2	MAG	1.0	157	26.3	7.0	9.5	0.472	18			
3	MAG	1.0	157	26.3	11.0	9.5	0,3	18			
4	MAG	1.0	157	26.3	9.0	9.5	0.367	18			Constrained applied
5	MAG	1.0	155	26.4	7.0	9.5	0.467	18			Constrained applied
6	MAG	1.0	157	25.4	11.0	9.5	0.29	18			Constrained applied